ABSTRACT

Title of Dissertation:	INVESTIGATION OF THE PRODUCTION AND DECAY PATHWAYS OF SUPEROXIDE BY CHROMOPHORIC DISSOLVED ORGANIC MATTER
	Danielle Le Roux, Doctor of Philosophy, 2022
Dissertation directed by:	Professor and Director of the Chemistry Graduate Program, Neil Blough, Department of Chemistry and Biochemistry

Chromophoric dissolved organic matter (CDOM) in natural waters absorbs sunlight which leads to the production of a suite of reactive intermediates and reactive oxygen species (ROS) such as superoxide ($O_2^{\bullet-}$) and hydrogen peroxide (H_2O_2). A significant amount of research over the years has investigated the sources and sinks of these two ROS. The currently accepted sequence of reactions for their production involves photochemically produced one-electron reductants (OER) within CDOM reacting with dissolved oxygen to form $O_2^{\bullet-}$, which undergoes self-dismutation to produce H_2O_2.

A previously used method to detect radical species with CDOM has been modified herein to be conducted simply using a fluorometer. Production rates of OER and H_2O_2 were measured for a variety of samples and correlations between the rates and optical/structural properties of the samples indicate that lower molecular weight species produce more OER and H_2O_2. Based on the stoichiometry of the mechanism above, the ratio of the production rate of OER to that of

H_2O_2 should be two. However, ratios from five to sixteen were obtained, which suggests that $O_2^{\bullet-}$ undergoes oxidative reactions that compete with dismutation.

The possibility of a light-dependent pathway for $O_2^{\bullet-}$ decay has been proposed but had yet to be explicitly demonstrated. Herein this sink is directly shown through $O_2^{\bullet-}$ spiking experiments. Rapid consumption of the $O_2^{\bullet-}$ spike occurs if injected into a sample during irradiation, as compared to a spike introduced into the sample in the dark, suggesting the presence of a light-dependent sink. Extensive data analysis and kinetic modeling of the $O_2^{\bullet-}$ decay data has allowed for approximations as to the extent of the sink and its decay rate constant.

$O_2^{\bullet-}$ and H_2O_2 are environmentally important species, and a significant amount of work has been done on modeling their concentrations in natural waters. Based on the work here, $O_2^{\bullet-}$ is produced at higher concentrations than previously believed, which has implications on the modeling of $O_2^{\bullet-}$ and H_2O_2 in natural waters. Additionally, the light-dependent oxidative sink of $O_2^{\bullet-}$ could be with moieties within CDOM, providing further insight to the photochemical transformation of DOM during transit from terrestrial sources to marine waters.

INVESTIGATION OF THE PRODUCTION AND DECAY PATHWAYS OF SUPEROXIDE AND HYDROGEN PEROXIDE IN NATURAL WATERS

by

Danielle Le Roux

Dissertation submitted to the Faculty of the Graduate School of the
University of Maryland, College Park, in partial fulfillment
of the requirements for the degree of
Doctor of Philosophy
2022

Advisory Committee:
Professor Neil Blough, Chair
Professor Akua Asa-Awuku
Professor Amy Mullin
Assistant Professor Mercedes Taylor
Assistant Professor Leah Dodson

Acknowledgements

First and foremost, I would like to thank my advisor, Dr. Neil Blough, for his mentorship and guidance throughout my graduate career. He has certainly trained me to be a thorough, detail-oriented, analytical chemist. The research, although frustrating at times, fascinated me and I truly enjoyed working in the group. I appreciated his patience, especially during the many times of problem-solving, whether it was with computer/instrument problems or trying to figure out funky data. I also want to thank him for being respectful and empathetic, it helped greatly during the several times I had to travel home to be with family.

I also want to thank Dr. Leanne Powers and Dr. Xu Zhang who we had as visiting scientists. Leanne helped me incredibly and spent a lot of time with me, teaching me how to use the flow-injection analysis instruments. She has also been a great resource for talking through results. Xu and I also spent a lot of time talking together, particularly about how in the world to study light-dependent superoxide decay, I'm sure he will enjoy my work on this!

I want to thank Dr. Carmen Cartisano and Dr. Marla Bianca, members of the group when I joined, for welcoming me, helping me get started in the lab, and teaching me the ropes of being a teaching assistant for Instrumental Methods of Analysis. I'll never forget my first interaction with them. They told me they liked to listen to music in the lab and asked me what I liked. I told them country music and that's what they both loved, and I knew right away we would be good friends. I'd also like to thank Shannon McDonnell and Rachel Ashmore, our current members, for their support and assistance over the past few years. We truly bonded during the major lab clean-out and move as we tried to make the best of it. I've also just had a blast with everyone outside of the lab. We've done a lot of fun things together!

I'd like to thank my committee members, Dr. Akua Asa-Awuku, Dr. Amy Mullin, Dr. Mercedes Taylor, and Dr. Leah Dodson for their time, serving on my committee, reading my dissertation, and providing feedback on my work.

I was a teaching assistant for Instrumental Methods of Analysis for nine semesters in total and I'd like to thank Natalia White for making it as enjoyable as possible. She was a pleasure to work for and I appreciated how much she cared for her teaching assistants.

My undergraduate advisors had a major role in shaping my future. I'd like to thank them, Dr. Nina Goodey and Dr. Yvonne Gindt, for all of their guidance during my time at Montclair State University. Dr. Goodey was the first professor I ever did research under and she shaped me into a scientist. Dr. Gindt provided me with a lot of advice regarding graduate school. They both saw my potential and convinced me to pursue my PhD. Dr. Gindt told me that sometimes it was going to stink, and sometimes I was going to hate it, but that I would make it through!

I'd like to thank all my friends and family back home for all their support throughout the years. Everyone made sure to check in from time to time to see how things were going, whether it was over the phone, on Zoom, or if they came to Maryland for a visit. Everyone was very supportive of me going through this journey and was there for me whenever I needed them.

Last but not least, I'd like to sincerely thank my fiancé, Ryan Dykstra. It was far from easy to pick up our lives in our hometown, along with our several pets, and move down to Maryland. I would not have been able to do this without him, and in the end, we went through graduate school together. We've been each other's greatest support and biggest motivators. I'm excited for our future ahead and am looking forward to heading back to New Jersey, though we had a ton of fun exploring Maryland and Washington D.C. during our time here!

Table of Contents

List of Tables

List of Figures

List of Abbreviations

Dissolved organic matter (DOM)

Chromophoric dissolved organic matter (CDOM)

Reactive oxygen species (ROS)

Singlet excited state of CDOM (^{1}CDOM*)

One-electron reductant (OER; CDOM$^{D^{\bullet+}/A^{\bullet-}}$)

Donor (D)

Acceptor (A)

Superoxide ($O_2^{\bullet-}$)

Hydroperoxyl radical ($HO_2^{\bullet}$)

Hydrogen peroxide (H_2O_2)

Singlet oxygen ($^1O_2$)

Hydroxyl radical ($OH^{\bullet}$)

Dissolved organic carbon (DOC)

Dissolved inorganic carbon (DIC)

Natural water (NW)

Extract (EX)

International Humic Substance Society (IHSS)

Humic acid (HA)

Suwannee river fulvic acid (SRFA)

Suwannee river natural organic matter (SRNOM)

Elliott soil humic acid (ESHA)

Delaware River (DR)

Station 19 (St. 19)

Echo Lake (ECL)

Greenwood Lake (GWL)

Monksville Reservoir (MKR)

Saint Mary's River (SMR)

Nuclear magnetic resonance (NMR)

Infrared spectroscopy (IR)

Fourier transform-ion cyclotron mass spectrometry (FT-ICR MS)

Electrospray ionization (ESI)

Electron paramagnetic resonance (EPR)

High-performance liquid chromatography (HPLC)

Apparent quantum yield (AQY)

Fluorescence quantum yield (FQY)

Excitation-emission matrices (EEMs)

Spectral slope (S_λ)

Spectral slope ratio (S_R)

Ratio between the absorbance at 254 nm and the absorbance at 365 nm (E2/E3)

Specific UV absorbance ($SUVA_\lambda$)

Mass-normalized absorbance (a*)

Production rate of hydroxylamine (R_H)

Production rate of hydrogen peroxide (R_{H2O2})

Production rate of superoxide ($R_{O2^{\bullet-}}$)

Milli-Q water (MQ)

Quinine sulfate (QS)

Superoxide dismutase (SOD)

Diethylenetriaminepentaacetic acid (DTPA)

Desferrioxamine (DFOA)

Methyl cipridina luciferin analog (MCLA)

Acridinium ester (AE)

3-amino-2,2,5,5-tetramethyl-1-pyrrolidinyloxy (3AP)

Limit of detection (LOD)

Limit of quantification (LOQ)

Post-irradiation decay (PID)

Post-steady-state spike decay (PSD)

Steady-state spike decay (SSD)

Decay spike decay (DSD)

Chapter 1: Chromophoric Dissolved Organic Matter and the Photoproduction of Superoxide and Hydrogen Peroxide

1.1 Historical Background and Goals of Research

The presence of hydrogen peroxide (H_2O_2) in natural waters was first discovered by Baalen and Marler in 1966 in Port Aransas, Texas.[1] Although the authors made no definite statement about where the H_2O_2 originated from, they suggested photochemical generation by pigment molecules in water, photochemical generation in the atmosphere and subsequent deposition, or metabolic generation by aquatic microbes. In 1977, Zafiriou suggested that chromophoric dissolved organic matter (CDOM) would be the primary species involved in aquatic photochemical reactions but noted that the literature still did not contain any photochemical systems for which we knew the structures of the reactants and products, the production rates, and the basics of the mechanisms.[2] In the early 1980's, researchers began to demonstrate that irradiation of CDOM in natural waters would generate superoxide ($O_2^{\bullet-}$) and/or H_2O_2, with H_2O_2 likely resulting from the dismutation of $O_2^{\bullet-}$.[3,4] With the confirmation that irradiation of CDOM within natural waters photochemically generates $O_2^{\bullet-}$ and H_2O_2, research surged in the mechanisms with which this was occurring. Meanwhile, in 1983 and 1987, work was published involving the use of superoxide dismutase (SOD), an enzyme that catalyzes $O_2^{\bullet-}$ dismutation to produce H_2O_2 with a high rate constant (2×10^9 $M^{-1}s^{-1}$)[5], that found that up to half of the $O_2^{\bullet-}$ generated in samples did not undergo dismutation to form H_2O_2.[6,7] Further research began investigating oxidative consumption pathways for $O_2^{\bullet-}$ that would not produce H_2O_2.

My research is in both the production of $O_2^{\bullet-}/H_2O_2$ by CDOM and in the decay pathways of $O_2^{\bullet-}$. The rest of Chapter 1 will provide a thorough background on CDOM, $O_2^{\bullet-}$, and H_2O_2

including: the origins of CDOM, the optical and structural properties of CDOM, what is currently known about $O_2^{\bullet-}$ and H_2O_2 production by CDOM and about $O_2^{\bullet-}$ decay pathways, and finally, the environmental importance of $O_2^{\bullet-}$ and H_2O_2. Chapter 2 and 3 are about my research on the production of $O_2^{\bullet-}$ and H_2O_2 by CDOM. More specifically, chapter 2 discusses the development of a fluorescence-based radical probe method to detect the pre-cursors to $O_2^{\bullet-}$ that are photoproduced within CDOM. Chapter 3 discusses the comparison of the radical probe measurements to $O_2^{\bullet-}$ and H_2O_2 measurements and how these measurements correlate to optical and structural features of CDOM. Chapter 4 and 5 are about my research on the decay pathways of $O_2^{\bullet-}$. In chapter 4, $O_2^{\bullet-}$ spiking experiments are presented along with in-depth kinetic analyses which demonstrated the presence of a significant light-dependent, oxidative decay pathway for $O_2^{\bullet-}$. Chapter 5 provides estimations for the magnitude of the light-dependent sink and provides information on possibilities for what the light-dependent sink is. To conclude, chapter 6 provides an overall summary of the dissertation and includes ideas for future research.

1.2 Dissolved Organic Matter and Chromophoric Dissolved Organic Matter

1.2.1 Origins

Dissolved organic matter (DOM) is present in all natural waters and is operationally defined as filterable carbon-containing material and has been the subject of numerous reviews.[8–12] The source of DOM has been a significant area of debate; DOM can originate from degradation of plant/animal material, exudation from phytoplankton and algae, or from anthropogenic effluents.[13,14] DOM can therefore include a multitude of biomolecules including lignin, tannins, carbohydrates, proteins, lipids, amino acids, and anthropogenic organic compounds. Additionally, DOM can be transformed through photochemical reactions or by

microbes.[13,14] A subset of DOM that absorbs light is called chromophoric dissolved organic matter (CDOM). Humic substances have been found to be a major component of CDOM and are the primary cause of the golden yellow color of CDOM.[15] Humic substances are products of degradation processes and consist of humic and fulvic acids.[11,16,17] Due to the variety in possible sources and routes of modification, there are no defined structures for DOM/CDOM, though a significant amount of research has been conducted in an effort to structurally characterize it.

1.2.2 Structural Properties

Modern techniques like nuclear magnetic resonance (NMR) spectroscopy, Fourier transform-ion cyclotron mass spectrometry (FT-ICR MS), and infrared spectroscopy (IR), have become popular tools to study molecular features of DOM.[18–23] For instance, FT-ICR MS has sufficiently high resolution and mass accuracy to assign unambiguous and exact molecular formulas for thousands of ions in a given sample.[24–27] Electrospray ionization (ESI) is by far the most commonly used method to minimize fragmentation, but the type of ionization used (positive or negative mode) will greatly influence resulting spectra depending on the weak and strong ionizers in the sample. Negative ion mode will be selective for acidic functionalities whereas positive ion mode will be selective for basic functionalities.[28] Using FT-ICR MS coupled with negative mode ESI, it has been found that DOM contains molecules with primarily carbon (C), hydrogen (H), and oxygen (O). Heteroatoms like nitrogen (N) and sulfur (S) have been observed but their amounts differ greatly by sample and ionization method used.[28] The use of selective chemical reduction with sodium borohydride and sodium borodeuteride has been used in conjunction with FT-ICR MS to identify aldehyde and ketone functionalities.[29,30] Based on NMR spectroscopy, DOM contains a large variety of functional groups including carboxylic acids, alcohols, quinones, ketones, and aldehydes.[19,22,31,32]

Discerning between molecular structures of CDOM from those of DOM is more difficult. Some studies have characterized CDOM using optical property analyses (absorbance and fluorescence) in conjunction with NMR spectroscopy and/or FT-ICR MS.[33,34] Positive correlations have been found between CDOM optical properties and lower molecular weight and more aliphatic structures.[33] However, large signal overlap in complex CDOM samples can further complicate these analyses. To alleviate this problem, some studies have used fractionation techniques to relate optical properties to general groups or classes of structures within CDOM. For example, using hydrophobic interaction liquid chromatography and NMR spectroscopy, it was found that highly fluorescent hydrophobic fractions were associated with terpenoids.[35] DOM fractionated by pH and analyzed by FT-ICR MS found a strong relationship between fluorescence and aromatic carboxylic acids.[36] Despite these findings, recent studies have also shown that the majority of DOM is generally indistinguishable across diverse aquatic ecosystems, due to the very large number of isomers for each molecular formula.[37,38] Therefore, despite the use of these powerful tools, it is still somewhat impossible to differentiate the molecular composition of CDOM from that of bulk DOM. Since CDOM can absorb and fluoresce, a significant research area exists dedicated solely to understanding these properties.

1.2.3 Optical Properties

CDOM absorbance is most often measured using standard benchtop spectrophotometers and 1-10 cm spectrophotometer cells or long pathlength (50-200 cm) liquid capillary cells, depending on the limitations of the particular instrument and the characteristics of the sample in question.[39] CDOM absorbance decreases exponentially with increasing wavelength, with a tail that can extend far into the visible region, and the spectra typically lack any appreciable peaks or shoulders (**Figure 1.1a**).[39–44]

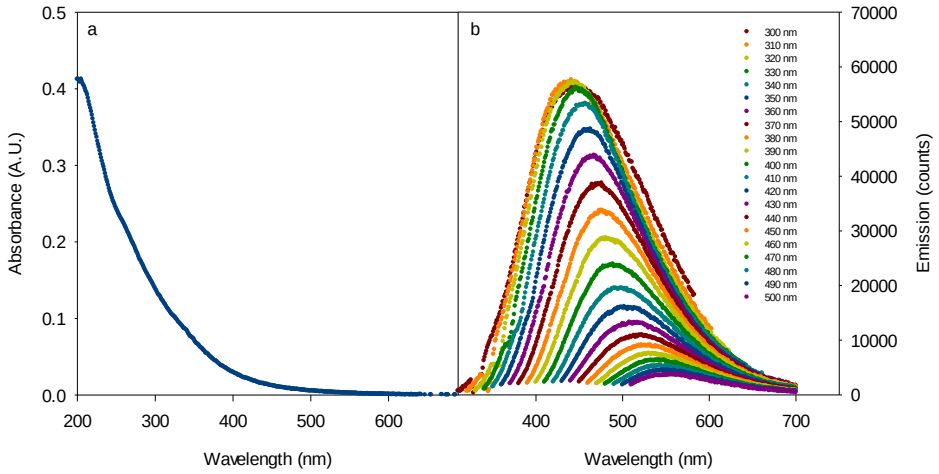

Figure 1.1. Absorbance plot (a) and EEM (b) for 10 mg/L SRFA in a 1 cm cuvette. Colors for EEM are for increasing excitation wavelength.

Fluorescence measurements of CDOM are primarily either steady-state [2D emission intensity vs. wavelength spectra, 3D excitation-emission spectra (EEMs)][45–49] or time-resolved.[50,51] The fluorescence of CDOM is typically featureless and broad, though fluorescent amino acids such as tyrosine and tryptophan, can produce additional emission signatures.[45,46] Recently, time-resolved fluorescence was used to probe the emission properties of CDOM, and revealed that short-lived species (<100 ps) dominate fluorescence emission decays in the visible spectrum.[51] Thus, steady-state fluorescence measurements severely under-represent the complexity of the photophysical properties of CDOM. CDOM fluorescence also has a peculiar feature in that the emission intensity decreases and shifts to longer wavelengths as the excitation wavelength is increased (**Figure 1.1b**).[52] This is unlike typical fluorophores where an increase in excitation wavelength normally only decreases the intensity of the emission, and not the wavelength at which the emission occurs.

Two models have been proposed to explain the observed optical properties of CDOM: 1) superposition model and 2) charge transfer model. The superposition model describes the optical properties as being the result of the superposition of optical characteristics of a large ensemble of

individual, non-interacting chromophores. The charge transfer model suggests that interactions between electron donating and electron accepting groups within CDOM give rise to optical charge transfer bands, which broaden the spectrum and produce the long wavelength absorbance and fluorescence.[52,53] The optical and photochemical evidence that supports the charge transfer model over the superposition model has been reviewed by Sharpless and Blough.[9] Another more recent review on both models was published by McKay.[12] More recent work has continued to support the charge transfer theory. For example, by studying structural features of DOM using NMR, along with different solvents to study backbone vs. exchangeable protons, the intensity of long wavelength absorbance was found to correlate with lower aliphatic content and higher carboxylic rich alicyclic moieties.[54] The authors suggested that increased aliphatic content separates electron donating and accepting groups, interfering with charge transfer interactions and therefore decreasing long wavelength absorbance. Another study used time-resolved fluorescence spectroscopy to study decay on the picosecond timescale and discovered the presence of an ultrafast component, consistent with excitation energy transfer within DOM.[55]

1.2.4 Production of Reactive Oxygen Species

The total absorption spectrum of unfiltered natural waters is composed of absorbance by water itself, phytoplankton, nonphytoplankton or detritus, and CDOM. CDOM dominates the total absorption spectrum in most natural waters in the blue and ultraviolet wavelengths, with CDOM accounting for 50% of the total absorption at 400 nm and increasing to ≥70% of the total absorption in the ultraviolet region.[56] Absorption of high-energy radiation by CDOM in the blue and ultraviolet regions drives photochemical reactions in surface waters. Upon absorption of light, CDOM enters excited singlet states and excited triplet states, which can subsequently react with dissolved oxygen in water to produce reactive oxygen species (ROS) such as hydroxyl

radical ($OH^{\bullet}$), singlet oxygen ($^1O_2$), superoxide ($O_2^{\bullet-}$), and hydrogen peroxide (H_2O_2).[57–64] H_2O_2 and $O_2^{\bullet-}$ are long-lived relative (days and minutes; respectively) to the other ROS (~μs) and have numerous methods for their detection which have been reviewed previously.[63,65] H_2O_2 has been studied for much longer than $O_2^{\bullet-}$, due to its much higher stability and ease of measurement compared to $O_2^{\bullet-}$.

1.3 History of the Study of Superoxide and Hydrogen Peroxide in Natural Waters

1.3.1 Early Work on the Study of the Production of Superoxide

In 1969, it was proposed that beta decay of ^{40}K would result in the formation of hydrated electrons within natural waters which could then react with dissolved molecular oxygen to form $O_2^{\bullet-}$.[66] The production of hydrated electrons was also shown to result from photoionization of natural water samples.[67,68] Similar work was conducted by Power et al. and they confirmed hydrated electron production from humic material.[69,70] However, it has been determined that their production rates[71], quantum yields[72] and steady-state concentrations[73] are much lower than those of $O_2^{\bullet-}$ and H_2O_2 and they are therefore not a major source. Another ROS, $^1O_2$, was also proposed to be involved in H_2O_2 production through reaction with DOM.[74] The use of azide ion in irradiated groundwater as a $^1O_2$ quencher resulted in the increase in H_2O_2, the opposite of what would be expected.[75] Dalrymple et al. measured H_2O_2 production in deuterated water which enhances the lifetime of $^1O_2$ by ten-fold, but they only saw a twenty percent increase in H_2O_2 production.[76] They also used the $^1O_2$ quencher beta-carotene and saw no effect on H_2O_2 production. Another possibility for $O_2^{\bullet-}$ production in natural waters was the direct electron transfer from an excited singlet state or triplet state in CDOM to molecular oxygen.[75,77] However, the excited singlet states have very short lifetimes[50] and triplet state quenchers such as

bromide and chloride ions have been shown to not have a major effect on the formation rates of H_2O_2.[78] Lastly, the possibility of direct excitation of optical charge transfer transitions and their subsequent reaction with molecular oxygen was explored. Charge transfer transitions are believed to occur between electron-rich donors (phenol or methoxylated phenol) and electron-poor acceptors (quinones or aromatic ketones/aldehydes) in close proximity within the molecule.[9] Sodium borohydride selectively reduces ketones and aldehydes to alcohols (irreversibly) and quinones to hydroquinones (reversibly).[79] Zhang et al. used sodium borohydride to reduce CDOM samples, removing ketone/aldehyde electron acceptors and depleting the long wavelength absorbance, which signifies the loss of the optical charge transfer transitions. However, this treatment did not significantly affect the rate of H_2O_2 production, supporting the theory that direct excitation into optical charge transfer transitions does not produce H_2O_2.[78] Additionally, these results showed that ketone and aldehyde functionalities are also not involved in H_2O_2 production.

It is now well accepted that the primary source of $O_2^{\bullet-}$ (and subsequently H_2O_2) in sunlit waters occurs through an abiotic photochemical pathway.[64,75] The current proposed series of reactions for the generation of H_2O_2 by this pathway involves an initial absorption of light (hv) resulting in the formation of excited singlet states (^{1}CDOM*) as shown in step one (**Figure 1.2**). In step two, intramolecular electron transfer occurs between electron rich donors (D) and electron poor acceptors (A) based on current evidence.[80] In terms of functional groups, the donors could be phenols while the acceptors could be quinones, since these do not get reduced by sodium borodeuteride.[9,80] The electron transfer results in the formation of one-electron reductants ($CDOM^{D\bullet+/A\bullet-}$) which further reduce dissolved molecular oxygen in step three to form $O_2^{\bullet-}$. In step four, $O_2^{\bullet-}$ undergoes dismutation to form H_2O_2.

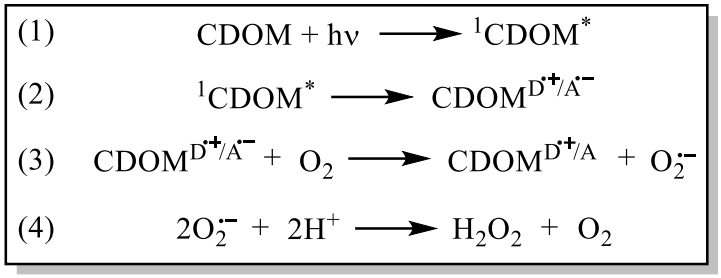

Figure 1.2. Proposed reaction scheme for the production of $O_2^{\bullet-}$ and H_2O_2 from CDOM.

1.3.2 Early Work on the Study of the Decay of Superoxide in Natural Waters

$O_2^{\bullet-}$ self-dismutation to form H_2O_2 is pH dependent [pK_a of hydroperoxyl ($HO_2^{\bullet}$) is 4.6 ± 0.15][81] and can theoretically occur between two $O_2^{\bullet-}$ molecules, between two $HO_2^{\bullet}$ molecules, or between a $O_2^{\bullet-}$ and a $HO_2^{\bullet}$.[81–83] The rate constants differ drastically among the possibilities from $k < 0.3\ M^{-1}s^{-1}$ to $k = 8.3 \times 10^5\ M^{-1}s^{-1}$ to $k = 9.7 \times 10^7\ M^{-1}s^{-1}$.[81,84] The simplified, pH dependent, rate constant equation is written as $k = 5 \pm 1 \times 10^{12} \times [H^+]$ which demonstrates that the rate of $O_2^{\bullet-}$ dismutation increases an order of magnitude for every unit decrease in pH.[81,85] The most probable reaction to form H_2O_2 is therefore between $O_2^{\bullet-}$ and a $HO_2^{\bullet}$.

Based on the reaction scheme discussed above (**Figure 1.2**), the ratio of the production rate of $O_2^{\bullet-}$ to that of H_2O_2 should be equal to two, as it takes two $O_2^{\bullet-}$ molecules to produce one H_2O_2. However, past research is inconsistent with these values and suggests the presence of oxidative sinks for $O_2^{\bullet-}$ that do not lead to H_2O_2 production.[86] As stated earlier, the enzyme superoxide dismutase (SOD) has been utilized to catalyze the dismutation of $O_2^{\bullet-}$ in an effort to outcompete other decay pathways. Using this approach, Petasne and Zika discovered that up to 41% of the $O_2^{\bullet-}$ generated in coastal seawater samples does not dismutate to form H_2O_2.[7] Powers et al.[87] also combined the use of SOD with $O_2^{\bullet-}$ measurements and also obtained a discrepancy of about 40% for natural freshwater from the Altamaha River and seawater samples from the

Skidaway River Estuary and the South Atlantic Bight. Garg et al. monitored H_2O_2 production in Suwannee River fulvic acid samples in the presence of SOD and showed that the loss of $O_2^{\bullet-}$ to other pathways was at least 70%.[77] However, SOD was found to have no effect on H_2O_2 production in other studies, which could either indicate the inability of SOD to outcompete other pathways or that issues exist with the use of SOD in certain experimental set-ups that impact its stability and function.[88,89]

1.4 Environmental Importance of Superoxide and Hydrogen Peroxide

1.4.1 Overview

There have been a number of reviews outlining the importance of photochemical processes on chemical and biological systems in natural waters.[2,57,58,63,64,90] These articles cover a vast array of past research in understanding the role of ROS in the environment including their involvement in trace metal cycling, the transformation of organic compounds (natural or anthropogenic), and their impact on aquatic organisms, as summarized in **Figure 1.3**. Following is a discussion of the prevalence of $O_2^{\bullet-}$ and H_2O_2 in natural waters with highlights of their environmental importance.

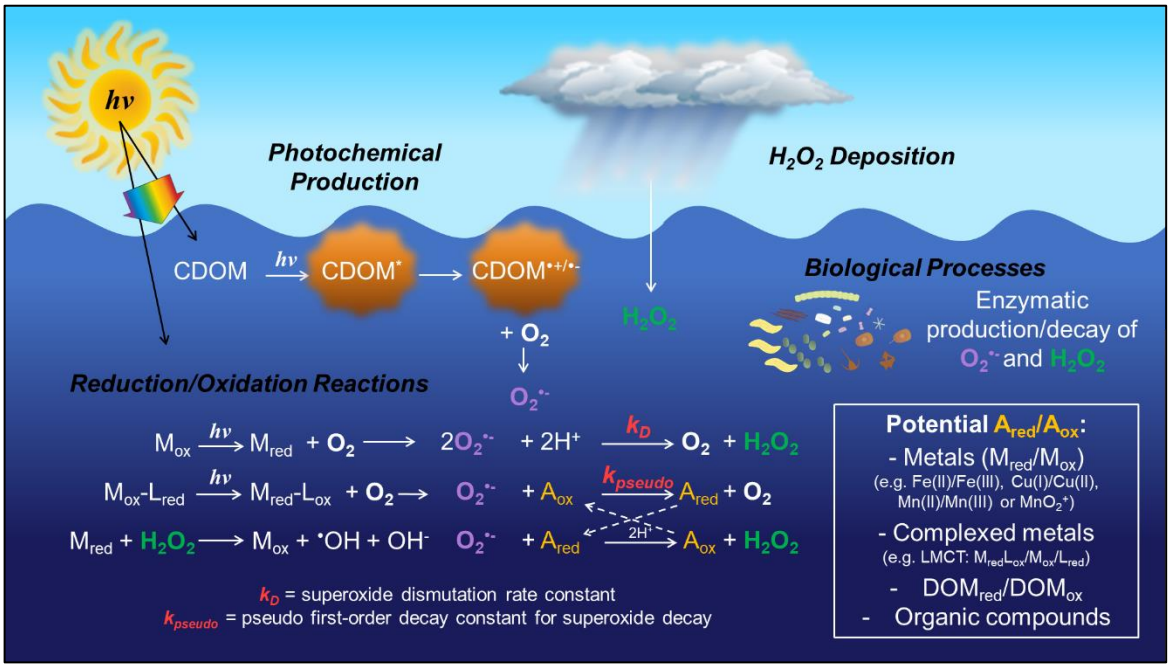

Figure 1.3. Sources and sinks of $O_2^{\bullet-}$ and H_2O_2 in natural waters.

1.4.2 Hydrogen Peroxide and Superoxide Distributions in Natural Waters

H_2O_2 has a diurnal cycle with daytime concentrations in the nM to low µM range, with terrestrial and coastal regions typically having higher concentrations than more marine waters such as the open ocean.[91–101] $O_2^{\bullet-}$ also has a diurnal cycle with concentrations typically in the nM range.[102] Variations of H_2O_2 concentrations have been observed based on geographical location, with mid to lower latitude regions having higher concentrations, likely due to increased UV radiation and increased wet deposition because of larger amounts of precipitation.[99,103] However, lower latitudes have also shown lower H_2O_2 concentrations, possibly due to increased H_2O_2 decay because of higher temperatures and higher consumption by increased biomass.[92]

H_2O_2 concentrations are highest in the surface layer (photic zone) due to primarily being produced by photochemical processes.[91,96,97,101,104–107] The concentration then typically decreases with depth as light penetration decreases, however, the processes that produce and consume H_2O_2 (microbial processes, deposition, reactions with metals, etc.) along with vertical mixing of

water layers has led to the observation of different trends of the concentration of H_2O_2 with depth. [91,94,95,99,103,108–110] Few works have measured $O_2^{\bullet-}$ concentrations with depth and the ones that have shown conflicting information. One shows that $O_2^{\bullet-}$ concentrations decrease with depth, which would be the expected trend based on H_2O_2, however, the authors also suggest that biological production would be highest at the surface due to the presence of larger amounts of biomass.[111] Alternatively, other sources suggest that $O_2^{\bullet-}$ maximums below the surface may also be due to biological production.[95,102,112]

1.4.3 Involvement in Trace Metal Cycling

Trace metals in natural waters can complex with DOM which greatly improves their solubility and makes them readily available for redox chemistry. Copper, iron, and manganese have been of particular interest as they are all commonly found in natural waters. For copper and iron, their oxidized forms [Cu(II) and Fe(III)] are the most stable in aquatic environments and organic matter complexes with these species make up over 90% of the values measured for total Cu(II) and Fe(III) concentrations in natural waters.[113,114] Manganese on the other hand, has been found to primarily exist as free dissolved Mn(II) or as Mn(III) or Mn(IV) oxides rather than in organic complexes.[115] The specific reactions that copper, iron, and manganese could be involved in, and the extent of such reactions, are highly dependent on many environmental factors including pH, concentration, and the presence of inorganic ions.[116–119] Due to this complexity, a significant amount of research has been conducted on metal-ROS chemistry.

One of the prominent metal related reactions in natural waters is the Fenton reaction. In the Fenton reaction, Fe(II) is oxidized by H_2O_2 to produce hydroxyl radical ($^{\bullet}OH$) and hydroxide ion (^{-}OH). This reaction has been suggested to be a significant sink of H_2O_2 and a prominent source of $^{\bullet}OH$ in natural waters.[120–123] $^{\bullet}OH$ is considered to be the most reactive radical in natural

waters; it is non-selective and strongly oxidizing and has been shown to react with DOM and organic compounds.[124] Copper has also been shown to be involved in Fenton-like chemistry.[120] Early work with Fenton-like reactions involving copper demonstrated that not only could Cu(I) be oxidized by H_2O_2, but the resulting Cu(II) could also be reduced by H_2O_2, producing a catalytic cycle for the loss of H_2O_2.[120,125] Organic copper complexes have been found to have catalytic rate constants (k_{cat}) of ~5 x 10^7 and ~7 x 10^8 $M^{-1}s^{-1}$ for strong and weak organic copper ligands respectively.[113] The rate constants for these reactions are also comparable to the rate constant for the dismutation of $O_2^{\bullet-}$, which would allow these reactions to compete with dismutation. Heller and Croot demonstrated this by adding Cu(II) to seawater samples and monitored $O_2^{\bullet-}$ decay. The addition of the metals increased the rate of $O_2^{\bullet-}$ decay, more so for copper than for iron.[126] Alternatively to a catalytic Fenton reaction cycle, more recent work studying these reactions with copper have shown that the oxidation of Cu(I) by H_2O_2 actually can lead to the production of Cu(III) with no production of $^{\bullet}OH$, though Cu(III) is also a strong oxidant in the environment.[127]

Hansard et al., studied Mn(II) oxidation by $O_2^{\bullet-}$ by monitoring the enhanced $O_2^{\bullet-}$ decay as a result of added nanomolar concentrations of Mn(II).[128] Through their kinetic studies, they obtained rate constants in the range of 10^6-10^7 $M^{-1}s^{-1}$ in seawater and simulated freshwater and were able to observe catalytic decay of $O_2^{\bullet-}$ at higher initial $O_2^{\bullet-}$ concentrations and excess Mn(II). It was proposed that this catalytic cycle could maintain moderate steady state concentrations of soluble Mn(III) in natural water systems in the presence of a continuous source of $O_2^{\bullet-}$. However, the Mn(III) production and concentrations were not measured directly and Wuttig et al. a few years later provided evidence that Mn(III) would not be produced to any appreciable extent.[129] They proposed that the more likely species produced between $O_2^{\bullet-}$ and

Mn(II) is the MnO_2^+ which could react with another $O_2^{\bullet-}$ to produce H_2O_2 and regenerate Mn(II). Regardless, Mn(II) has been found to be a significant sink of $O_2^{\bullet-}$ in waters where relatively high concentrations of it exist.[130] Interestingly, around this same time, a Science paper emerged that demonstrated the prevalence of Mn(III)-ligand species in sediment porewater.[131] A few years later, Mn(III)-ligand species were also found to be prevalent in estuarine and marine water, making up a significant portion of the dissolved Mn content.[132–134] Mn(III) is considered a strong oxidant of organic materials and may have a large impact on the carbon cycle.[133] Mn(III) is also the pre-cursor to Mn oxide minerals which are major adsorbents and oxidants in the environment.[135,136]

1.4.4 Biological Implications

H_2O_2 and $O_2^{\bullet-}$ ($HO_2^{\bullet}$), being reactive species, have potential to cause harm to organisms by reacting with biomolecules such as proteins, lipids, and nucleic acids.[137–139] For example, $HO_2^{\bullet}$ has been shown to damage cytosolic enzymes[139], photoproduced ROS by DOM have also been implicated in damaging the DNA of *Daphnia magna*[140], and H_2O_2 decreased the activity of extracellular enzymes of marine prokaryotes by 62%.[141] The primary mechanism for H_2O_2 removal in the ocean is believed to be through microbial enzymes via dismutation by catalase, or reduction with peroxidase, both of which are typically produced extracellularly for protection.[64,98,142,143] The cyanobacterium *Prochlorococcus*, responsible for nearly half of oceanic primary production of nutrients, lacks catalase and therefore cannot remove H_2O_2 on its own.[144] Therefore, *Prochlorococcus* rely heavily on the microbial community's overall ability to remove it. It has been noted that while surface concentrations in coastal waters on the order of 100 nM are too low to directly cause bacterial mortality, H_2O_2 still contributes to oxidative stress in microbes as evidenced by increased catalase activity.[145]

Interestingly, some aquatic organisms have been found to produce $O_2^{\bullet-}$ despite the possible dangers. $O_2^{\bullet-}$ has been implicated as being both beneficial and harmful to the health and survival of coral reefs and recently Diaz and coworkers have made direct measurements of $O_2^{\bullet-}$ concentrations in coral reefs to further study the dynamics of $O_2^{\bullet-}$ production in a reef environment.[146] $O_2^{\bullet-}$ measurements directly near the corals' surface varied in magnitude based on species but reached nearly 140 nM and decreased rapidly moving away from the coral. Their results indicated that there is species-specific regulation of $O_2^{\bullet-}$ concentrations within the vicinity of the coral, with extracellular production and enzymatic decay both playing roles. Diaz and coworkers have also observed significant $O_2^{\bullet-}$ and H_2O_2 production from harmful algal bloom causing phytoplankton.[147] More work is needed to understand the role $O_2^{\bullet-}$/H_2O_2 play in both coral reefs and algal blooms.

Microbial production of $O_2^{\bullet-}$ has been shown to be beneficial in a few other instances. The cyanobacterium *Lyngbya majuscula* produced $O_2^{\bullet-}$ to reduce organically complexed Fe(III) to Fe(II) which resulted in increased uptake of Fe(II) by the organism.[148] $O_2^{\bullet-}$ was also shown to be important in the oxidation of manganese oxides by *Roseobacter* species and the resulting oxidized manganese oxides are important in a variety of biogeochemical cycles.[149]

1.4.5 Transformation of Natural and Anthropogenic Compounds

Anthropogenic contaminants such as chlorophene (disinfectant) and 17β-estradiol (hormone medication) have been found in natural waters. Work by Wang et al. showed that concurrent involvement of $O_2^{\bullet-}$ and manganese resulted in the formation of primarily dimerized products. An estrogenic activity study showed that the dimers were less toxic than the original compounds. However, it was noted that the total organic carbon and pH of the water can have an

impact on the efficiency of the transformation of these contaminants.[150]

Transformation of compounds could instead lead to decreased availability of compounds considered to be nutrients. In a kinetic and mechanistic study of phenol-containing compounds acetaminophen (pain reliever), 2,4,6-trimethylphenol (model phenol), and tyrosine (amino acid), it was found that $O_2^{\bullet-}$ could react with the phenoxy radical form of these compounds to produce peroxide-like structures.[151] The reactivity of the phenolic compounds in this manner and their resulting stability depended on the structure of the parent phenol. The fate of the tyrosine-peroxide was further investigated, and it was discovered that it underwent hydrolysis and a reduction reaction to form a bicyclic compound. This transformed product did not decay nearly as rapidly as the parent compound tyrosine in dark decay studies of these compounds in unfiltered natural water samples. The stability of the bicyclic transformation product in natural waters indicated that it was less bioavailable to aquatic microbes compared to tyrosine.[152]

Silver nanoparticles are commonly used in consumer products such as athletic wear, medical bandages, and personal care products due to their antibacterial properties. Subsequently, their release into the environment has been an increasing concern. It has been found that DOM complexes with silver nanoparticles in the environment and that H_2O_2 enhances the oxidation of them by 17-27% which would release silver into the environment. This trend was more notable at lower concentrations of silver nanoparticles. At higher silver nanoparticles concentrations, direct photochemical reactions appear to play a larger role in their oxidation.[153]

1.4.6 Involvement of Superoxide in the Photodegradation of Dissolved Organic Matter

DOM presence in the open ocean has perplexed scientists due to the lack of terrestrial based sources which led to significant research into the possibility of the transportation of terrestrially sourced DOM to the open ocean through river outlets. However, open ocean DOM

differs significantly in its optical/structural properties from terrestrial DOM.[21,49] There is some evidence that marine DOM can originate from microbial processing of marine organic material[154] or by direct release from microbes.[155,156] However, marine DOM is believed to primarily originate from terrestrial sources and that photochemical modification changes its optical/structural features.

Irradiation of CDOM results in a loss of absorbance, breakdown of aromatic carbon, decreases in dissolved organic carbon (DOC) concentrations, and decreases in DOM molecular weight[157–159] while producing carbon monoxide (CO) and dissolved inorganic carbon (DIC).[160–164] The decrease in CDOM absorbance is typically faster in the UVA (320 – 400 nm) and visible (≥ 400 nm) wavelength regions.[157,165,166] Because not all DOM is colored, and the loss of color does not necessarily mean the loss of carbon, samples typically lose absorbance faster than they lose DOC.[158,166,167] Only recently with advancement in FT-ICR MS and NMR analysis of DOM have researchers been able to study more specific structural changes that occur as a result of irradiation. The loss of terrestrial character has been explored in terms of biomarkers such as lignin phenol content and ^{13}C isotopic signatures.[158,168–170] Lower carbon-13 percentage compositions[171] and high amounts of lignin phenols[172] are indicative of terrestrial DOM as compared to marine DOM. As a result of irradiating Congo River water, enrichment in dissolved organic carbon-13 and a large loss in lignin phenol content was observed.[167] Additional findings during irradiations of riverine DOM have found that unsaturated aromatic formulas decreased and more saturated and aliphatic formulas increased.[168,173] The aforementioned works only studied photochemical reactions through irradiation of the samples, so discerning between direct photochemical reactions and indirect reactions from photoproduced ROS is not possible.

Investigations then sought to understand the role ROS play in DOM oxidation and to elucidate possible mechanisms. Several groups demonstrated the involvement of oxygen by studying the photochemical uptake of molecular oxygen by natural water samples.[161,174] Increasing the concentration of molecular oxygen increased the rate of photodegradation.[161] Apparent quantum yield spectra for the consumption of molecular oxygen and for the production of H_2O_2 both decreased with increasing wavelength used for irradiation and it was estimated that half of the molecular oxygen consumption led to H_2O_2 production, leaving the other half to consumption by other processes, such as formation of organic peroxides.[174]

Work then began by singling out particular ROS that could be responsible. $OH^{\bullet}$ reaction with DOM has been demonstrated[175], though the magnitude of their impact appears to be small.[162] The use of furfuryl alcohol as a $^1O_2$ scavenger demonstrated that $^1O_2$ played a role in DOM transformation.[176] Reaction between DOM and photoproduced $^1O_2$ and $O_2^{\bullet-}$ has been shown to result in decreased aromatic carbon and increased aliphatic carbon, oxygen-containing aromatic groups, and carbonyl-containing groups in the DOM pool. Another study found that $^1O_2$ reacted with and removed formulas with O/C ratios > 0.3 while $O_2^{\bullet-}$ reacted with and removed formulas with O/C < 0.3. Reaction with $^1O_2$ resulted in the formation of more oxygenated structures while reaction with $O_2^{\bullet-}$ resulted in formation of more aliphatic structures.[177]

1.4.7 Climate Change Concerns

Potential effects of climate change on biogeochemical cycles has been reviewed previously, although little is known about the impacts on ROS and their reactions.[178] Only recently has the topic been addressed in regards to triplet DOM, $^1O_2$, $^{\bullet}OH$, and carbonate radicals.[179] Changes in seawater temperature and pH, especially in the Arctic where projected decreases in pH could produce a 185% increase in hydrogen ion concentration[180], will certainly

impact ROS production and decay. An increase in seawater temperature leads to an increase in H_2O_2 production, typically by a factor of 2 for every 10° C increase in temperature.[104] By plotting the natural log of the H_2O_2 production rate versus the reciprocal of temperature, H_2O_2 photoproduction follows the Arrhenius rate law, with the activation energy being ~31.9 ± 12 kJ mol^{-1}. This demonstrates the temperature dependence, which is likely due to the fact that oxygen reduction to $O_2^{\bullet-}/HO_2^{\bullet}$ and dismutation are thermal processes.[96,104]

Previous work has demonstrated the pH dependence of DOM photodegradation rates using terrestrial reference materials, indicating that photodegradation rates increase with increasing pH.[181,182] However, this may not be the case for all natural waters, because Yangtze River water had the lowest photobleaching rate at pH 6 and 7, and higher photobleaching rates at pH 4 and 10[182], perhaps due to the presence of iron.[183]

It has been shown that the rates of Fe(II) oxidation by H_2O_2 are a function of pH, temperature, and salinity.[184] It has also been shown that in the presence of DOM, the rate of Fe(II) oxidation by H_2O_2 markedly decreases.[185] This experiment was performed at a pH of 8.4 and so the authors concluded that the formation of a Fe(II)-DOM complex prevents oxidation by H_2O_2. On the other hand, Voelker and Sulzberger[186], in a similar set of experiments, found that Fe(II) oxidation by H_2O_2 was accelerated in the presence of fulvic acids at a pH of 5. Although these studies used model systems and may not be fully representative of natural water systems, it is possible that decreasing pH could shift redox rates involving H_2O_2 and other ROS.

An interesting point brought up by Mostofa and co-workers is that the acidification of natural waters due to various climate change issues could be offset by $O_2^{\bullet-}$ chemistry. The process of $O_2^{\bullet-}$ dismutation consumes protons to form H_2O_2 and this process has been shown to be able to be catalyzed as discussed earlier. However, it is noted that the extent of this offset

requires extensive analysis of all possible reactions with careful note on charge balances, though it does warrant further consideration as a possibility.[187]

1.5 Overview of Research

Due to the lack of an understanding of the extent of $O_2^{\bullet-}$ production and the observed discrepancies between relative production rates of $O_2^{\bullet-}$ and H_2O_2 in previously published studies, my research was focused on method development for studying $O_2^{\bullet-}$ precursors and analyzing the production and decay rates of $O_2^{\bullet-}$. More specifically, chapter 2 provides an overview on the development of a radical probe method to trap the reactive species, the one-electron reductants, within CDOM that are the believed pre-cursors to $O_2^{\bullet-}$ production. The re-development of the method to be conducted simply via a fluorometer is discussed. Chapter 3 goes over how the radical probe measurements were used in relation to $O_2^{\bullet-}$ and H_2O_2 measurements and how these measurements correlate to optical and structural features of CDOM. Chapter 4 delves deeper into the study of $O_2^{\bullet-}$ and its production and decay rates. $O_2^{\bullet-}$ spiking experiments are presented which provide insight into a light-dependent, oxidative decay pathway for $O_2^{\bullet-}$. Kinetic analyses of the data allow for estimations of the rate constants of the decay pathways. Chapter 5 provides more insight into the magnitude of the light-dependent sink and reviews and tests possibilities for what the sink of $O_2^{\bullet-}$ could be. Chapter 6 concludes the dissertation with an overall summary and provides future research directions.

Chapter 2: Development and Validation of a Radical Probe Method to Quantify the Production of One-electron Reductants

The majority of this chapter has been published in reference 260:

Le Roux, D. M.; Powers, L. C.; Blough, N. V. Photoproduction Rates of One-Electron Reductants by Chromophoric Dissolved Organic Matter via Fluorescence Spectroscopy: Comparison with Superoxide and Hydrogen Peroxide Rates. *Environ. Sci. Technol.* **2021**, *55* (17), 12095–12105. https://doi.org/10.1021/acs.est.1c04043.

I performed all experiments and data analysis and prepared the first draft of the manuscript. Dr. Powers and Dr. Blough assisted in data analysis and editing the manuscript.

2.1 Abstract

Due to the ability of nitroxide probes to react with free radicals, they have been used to probe for reducing species within CDOM, which has enabled the study of reactive groups within CDOM that lead to the production of ROS. The focus of its application to CDOM photochemistry is reaction with reducing radicals, which produces the hydroxylamine, a stable O-unsubstituted product. Presented here is a small review of past methods such as electron paramagnetic resonance spectroscopy (EPR) and high-performance liquid chromatography (HPLC) coupled with fluorescence detection. The development and validation of a fluorometer-based method is presented along with the results of various controlled experiments that demonstrate the validity of the method and confirm findings from previous versions of the method. Additionally, the applicability of the method to natural waters is presented, with some careful modifications to the method parameters.

2.2 Introduction

Radicals have been suspected to be involved in chemical reactions in natural waters for quite some time.[2] The early difficulties of measuring radicals in natural waters came down to low steady-state concentrations and short lifetimes that made measurements via absorbance or

electron paramagnetic resonance (EPR) exceedingly difficult.[63,188] To combat such issues, using probe molecules to react with or trap the radicals was proposed.[189] Although an indirect method of measurement, the probes would produce stable products that could be easily measured.[63,188,189]

Probe molecules must satisfy certain parameters in order to be useful for a particular application.[63,188] First, in order to avoid false-positive/interfering signals, the probe must only react with the radical molecule in question, and not other radical species that may also be present. Second, the probe must react with the radical of interest with a large enough rate constant to effectively compete with other processes that the radical molecule may decay through. Third, the method to measure the probe-radical adduct must be sensitive to measure low concentrations and the method should be relatively easy to conduct. Fourth, the probe should not have any identifiable signal itself in the detection method being used and the probe should not be involved in other side reactions that would interfere with the detection of the radical in question. In regards to photochemical processes in particular, the probe should not be photochemically active itself, with particular concern being photochemical degradation of the probe.[63,188]

Water-soluble nitroxides are stable radical probes that can react with carbon-centered, reducing, and inorganic radicals and these reactions are irreversible under most conditions.[189,190] Reaction with carbon-centered radicals forms O-substituted products (alkoxyamines), whereas reaction with reducing radicals produces the O-unsubstituted products (hydroxylamine). Reaction of the nitroxide probes with photoproduced radicals by DOM, under anaerobic conditions, was first studied in humic acid (HA) using EPR spectroscopy, since nitroxide probes convert from paramagnetic (have unpaired electrons) to diamagnetic (have paired electrons), allowing for the monitoring of the loss of spin of the unpaired electron as the probe was reduced by DOM.[189] Under anaerobic conditions, significant consumption of the probe was observed

during irradiations of HA, indicating photoproduction of radicals within HA. If aerobic conditions were used, the initial rate of loss of the probe was lowered dramatically, indicating that molecular oxygen also reacts with the radical species within HA.[189]

Further work improved upon the sensitivity of the method by derivatizing the nitroxide probe with a fluorophore and employing fluorescence detection (**Figure 2.1**).[191] The paramagnetic nitroxide coupled with fluorescamine will have low fluorescence because of efficient intramolecular quenching by the nitroxide.[192] However, when the nitroxide is converted to a diamagnetic product, the fluorescence is no longer quenched, providing a large signal increase above background. High performance liquid chromatography (HPLC) was used with fluorescence detection to separate and detect the resulting fluorescent radical adduct forming during irradiation of solutions of various ketones and α-keto acids under anaerobic conditions.[191,193] Additionally, the first application of this method to natural waters and Suwannee River Fulvic Acid (SRFA) was conducted. It was found that the hydroxylamine (product of reduction of probe by DOM) is the major product during anaerobic irradiations. The contribution to fluorescence from other products (O-substituted products; alkoxyamines) was insignificant, making the separation of the products unnecessary.[193]

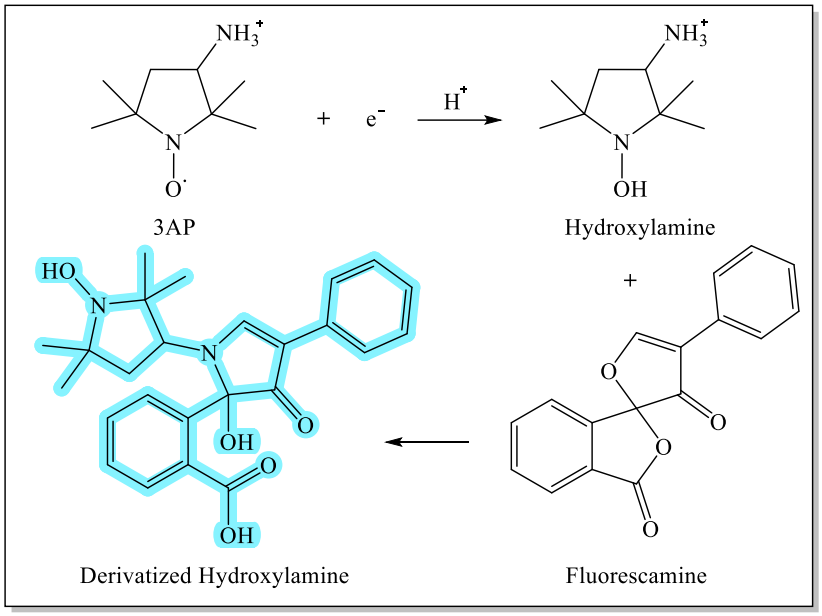

Figure 2.1. Reduction of the radical probe 3-amino-2,2,5,5-tetramethyl-1-pyrrolidinyloxy (3AP) and subsequent derivatization with fluorescamine to produce the fluorescent product, the hydroxylamine. 3AP is the specific probe used in the work in this dissertation, though other variants have been used previously.

Since the hydroxylamine is the major product under anaerobic conditions, its steady-state fluorescence signal should dominate compared to the very small contributions from other products, making separation unnecessary. Therefore, the nitroxide probe and derivatization method was modified to be conducted simply using fluorescence spectroscopy to quantify the production of one-electron reductants (OER) photoproduced within CDOM. The production rate of hydroxylamine (R_H), the one-electron reduced and derivatized product of the nitroxide probe, will be used as a proxy for production of OER. Validation experiments are consistent with previously published results[193,194] and include: 1) nitroxide probe, fluorescamine, and CDOM concentration dependence; 2) linearity of production over time; 3) stability in air; 4) oxidation of the hydroxylamine by copper; and 5) detection limits. Presented in this chapter are the results for the method development and validation process of the method and the modifications that were needed for application to natural waters. Chapter 3 will delve deeper into how the measurements relate to $O_2^{\bullet-}$ and H_2O_2 production and to optical/structural features of CDOM.

2.3 Materials and Methods

2.3.1 Materials

Boric acid, sodium hydroxide (NaOH), methanol, fluorescamine, and 3-amino-2,2,5,5-tetramethyl-1-pyrrolidinyloxy (3AP) were purchased from Millipore Sigma. Sodium dithionite ($Na_2S_2O_4$) was purchased from Acros Organics. Hydrochloric acid (HCl) and 0.2 µM nylon syringe filters were purchased from VWR International. C-18 solid phase extraction columns were purchased from United Chemical Technologies. Acetonitrile was purchased from Fischer. Ultrapure nitrogen was purchased from Airgas. Suwannee River fulvic acid (SRFA; 2S101F) was purchased from the International Humic Substance Society (IHSS). Natural water (NW) from the Delaware River was collected in August of 2006 (St. 19; 40.1 N, -74.8 W). Purified water (18 MΩcm) was obtained from a Milli-Q system.

2.3.2 Solid Phase Extraction

DOM was extracted from natural waters using C-18 solid phase extraction columns.[195] Natural waters were filtered with pre-rinsed 0.2 µm nylon filters and then acidified to pH 2 with HCl. C-18 columns were pre-treated with methanol followed by acidified MQ pH 2. The filtered and treated natural water was then pumped through the column to extract the DOM. After, the column was rinsed with acidified MQ pH 2. Methanol was used to elute the DOM from the column and this eluent was dried down. Finally, MQ was used to re-dissolve the extract which was then brought to pH 7 using NaOH.

2.3.3 Sample Preparation

Stock solutions of extracts and reference materials were prepared by diluting/dissolving the extract or reference material in MQ water. These stocks were adjusted to pH 7 using NaOH

and HCl and filtered using pre-rinsed 0.2 μM nylon filters. Dilutions of these stocks at desired concentrations for experiments were then prepared by diluting the stock solutions with 50 mM borate buffer at a pH of 8 unless otherwise noted. Natural waters were filtered with pre-rinsed 0.2 μm nylon filters and used as is.

2.3.4 Measurement of One-electron Reductants

The production of OER (as R_H) was measured using 3-amino-2,2,5,5-tetramethyl-1-pyrrolydinyloxy (3AP) followed by derivatization with fluorescamine.[86] Fluorescence measurements were conducted with a Horiba Fluoromax-4. The excitation wavelength was set to 450 nm, band passes were 4 nm, the integration time was 0.1 s, and the emission was scanned from 460-600nm. Although 390 nm is approximately the wavelength of maximum absorption, an excitation wavelength of 450 nm was used to prevent inner filter effects and to reduce the background due to CDOM itself. The emission intensity at 490 nm was used for data analysis.

A standard curve for hydroxylamine was produced by reducing derivatized 3AP with sodium dithionite ($Na_2S_2O_4$). First, 600 μM 3AP was combined with 1 mM fluorescamine (in acetonitrile) in 50 mM borate buffer pH 8 in 1 cm quartz cuvettes (with screw tops fitted with septa) that were then deoxygenated for 30 minutes using ultrapure nitrogen gas. A dithionite stock solution was then prepared by adding a small amount of the solid to a 1 cm quartz cuvette of MQ water at pH 11 that had been deoxygenated. The concentration of the dithionite stock solution was monitored spectrophotometrically ($\varepsilon = 8000\ M^{-1}cm^{-1}$ at 315 nm)[196] using a Shimadzu UVPC 2401 benchtop spectrophotometer. Increasing amounts of the dithionite stock were added to the derivatized 3AP using a gas-tight syringe and the emission was recorded after each addition.[193] Standard curves were performed in at least triplicate.

Unless otherwise noted, samples were mixed with 600 μM 3AP in 1 cm screw-top quartz

cuvettes fitted with caps and septa to measure R_H. Ultrapure nitrogen was first bubbled through the sample for 30 minutes and was then irradiated for 15 minutes using a 300-watt xenon arc lamp with a 20 cm water jacket (to remove infrared irradiation to prevent sample warming). A 325 nm cut-off was the primary filter used to approximate the solar spectrum in natural waters. Other cut-off filters (355, 380, 399, 418, and 440 nm) were used to evaluate wavelength-dependence. The headspace of the cuvette was continuously purged with nitrogen throughout the irradiation. The sample was then derivatized directly in the cuvette, using a gas-tight syringe, by the addition of 200 μL of 15 mM fluorescamine in acetonitrile (1 mM in sample) unless otherwise noted. The sample was mixed for about one minute and then was placed in the fluorometer for measurement. A non-irradiated sample was derivatized and measured to determine the blank. If necessary, samples were then filtered with a pre-rinsed 0.2 μm nylon filter into a clean cuvette to remove any excess precipitated fluorescamine and the fluorescence was measured. Filtering the samples removes issues with scattering in the measurements due to particulates and does not remove any of hydroxylamine product (**Figure A2.1**). The initial rate of hydroxylamine production was calculated by the following equation:

$$R_H = \frac{T_{15} - T_0}{15\ min * 60\ s/min} \quad \text{(Eqn. 2.1)}$$

where T_{15} is the product yield after the 15 minute irradiation and T_0 is the blank measurement.[86]

The hydroxylamine method required some modifications to be used in natural waters due to their variability. Additional buffering of natural waters was needed following irradiation but before derivatization to maintain a higher stable pH and a higher concentration of fluorescamine was needed to ensure complete derivatization. For the natural waters tested in this study, an addition of ~100 μL of a 50 mM borate buffer at pH 11 and 2 mM fluorescamine was sufficient. The details of determining these parameters will be explained in the results and discussion.

2.3.5 Rate of Excitation and Apparent Quantum Yields

Rates of production were normalized to the rate of excitation of the sample to give apparent quantum yields (Φ).

$$\Phi = \frac{Rate\ of\ production\ of\ species\ (R_S)}{Rate\ of\ Excitation\ (R_{EX})} \quad \text{(Eqn. 2.2)}$$

This ensures that variability in sample concentrations/absorbance are taken into account. Rate of excitation was calculated under optically thin conditions by the equation:

$$R_{EX} = \int_{300}^{800} a(\lambda)\ I(\lambda)\ d\lambda \quad \text{(Eqn. 2.3)}$$

where a(λ) is the Naperian absorption coefficient of the sample in cm^{-1} and I(λ) is the absolute irradiance of the xenon arc lamp in photons $cm^{-2}\ s^{-1}\ nm^{-1}$.[86] Absorbance measurements of samples were conducted on a Shimadzu UVPC 2401 benchtop spectrophotometer in a 1 cm cell. The instrument was always baselined to air and blank measurements (MQ or buffer) were taken and were subtracted from absorbance spectra. The absolute irradiance of the lamp from 300-800 nm was measured using an Ocean Optics spectroradiometer (**Figure A2.2**).

2.4 Results and Discussion

2.4.1 Validation and Control Experiments

Reduction of 3AP with dithionite to form hydroxylamine, followed by derivatization with fluorescamine, produced an enhanced fluorescence emission that was linear (emission at 490 nm was used) with the extent of reduction of 3AP, thus allowing for method calibration (**Figure 2.2a and 2.2c**). Irradiation of SRFA in the presence of 3AP also produced enhanced signals, indicating reduction of 3AP, which were linear with both the irradiation time (**Figure 2.2b and 2.2d**) and the concentration of SRFA (**Figure A2.3**). The difference in spectral shape between **Figure 2.2a** and **2.2b** is due to the background fluorescence of CDOM. The hydroxylamine

signal was stable in air for at least two hours (**Figure A2.4**).

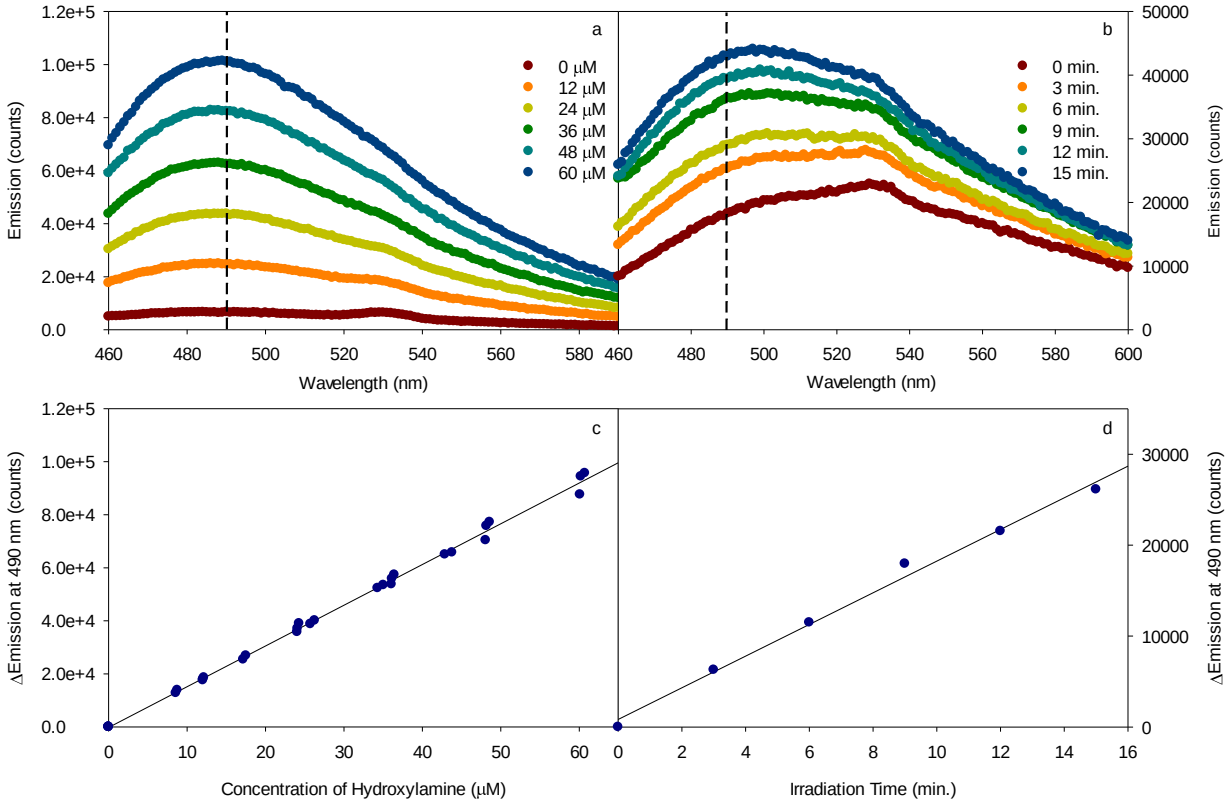

Figure 2.2. Raw emission signals for (a) hydroxylamine produced via dithionite reduction of 600 μM 3AP and (b) hydroxylamine produced by reduction of 600 μM 3AP during an irradiation of 10 mg/L SRFA. Standard curve for hydroxylamine; linear fit has an equation y = 1530(±10)x with an R^2 of 0.99 (c). Linearity of hydroxylamine production with irradiation time; linear fit has an equation y = 1820(±50)x with an R^2 of 0.99 (d).

To ensure that the fluorescence signal obtained was due mostly to derivatized hydroxylamine and not other products, Cu^{2+} was added in the form of CuCl to the sample. Cu^{2+} catalyzes the oxidation of hydroxylamine, which would turn it back into its radical form, resulting in the loss of fluorescence.[197,198] Introduction of a low concentration (7.3 μM) of Cu^{2+} to an irradiated sample (10 mg/L SRFA with 325 nm cut-off for 15 min.) continued to lower the fluorescence signal over the course of 40 minutes, signifying the oxidation of the hydroxylamine (**Figure 2.3**). The signal did not come completely down to the level of the non-irradiated sample that was also treated with Cu^{2+}, indicating the presence of some other radical adducts radical adducts (methyl,

acetyl, pentanoyl)[193], however their contribution to the overall fluorescence is less than 15%.

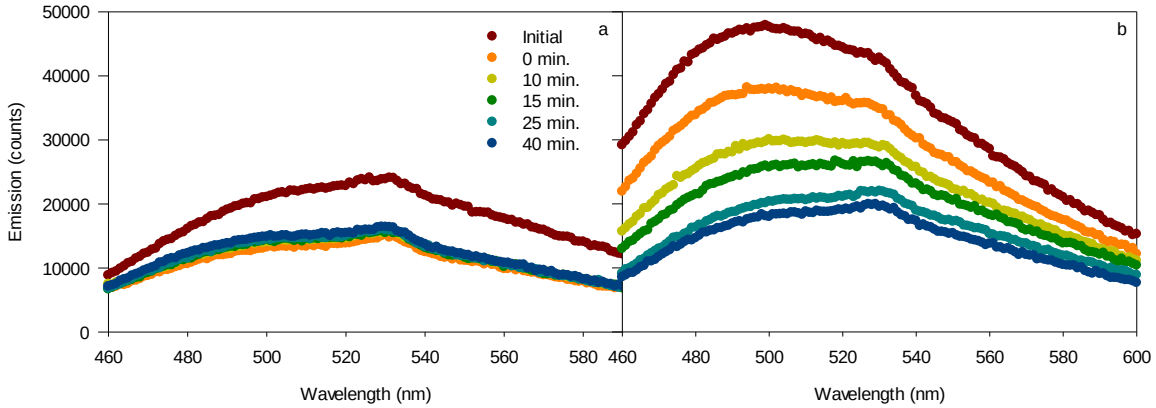

Figure 2.3. Loss of emission intensity due to the oxidation of hydroxylamine using copper chloride. (a) Non-irradiated and (b) irradiated 10 mg/L SRFA. Initial measurements were taken before adding copper. Signal at t=0 min. was the intensity obtained immediately upon adding the copper chloride.

To ensure that sufficient 3AP was being utilized to trap all photoproduced one-electron reductants, the dependence of R_H on the concentration of 3AP was evaluated in a solution of 10 mg/L SRFA (irradiated with 325 nm cut-off filter for 15 min.) (**Figure 2.4**).

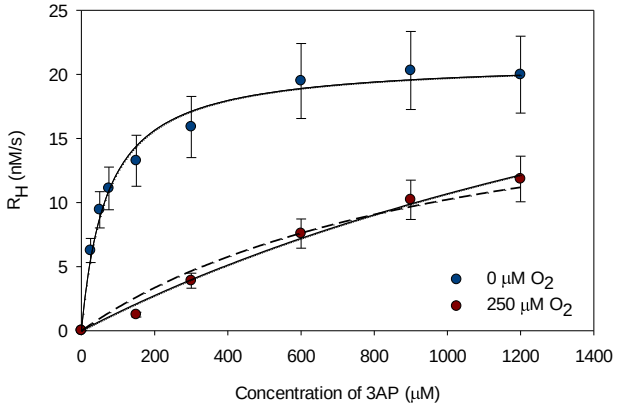

Figure 2.4. Dependence of R_H on 3AP concentration for 10 mg/L SRFA under 0 and 250 µM molecular oxygen. Solid lines are the fits of the data to equation 2.4. The dashed line is the fit of the 250 µM molecular oxygen data to equation 2.4, but with A restricted to 21.1 nM/s. Error bars are standard deviation based on a relative standard deviation of 15% which was the maximum deviation observed for triplicate R_H measurements.

The production and consumption of OER in the presence of molecular oxygen and 3AP can be described by the reaction scheme shown in **Figure 2.5**.[86]

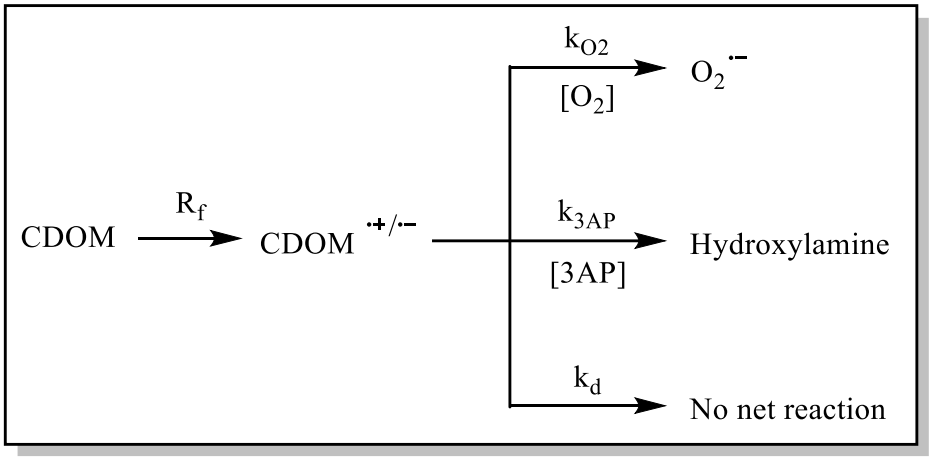

Figure 2.5. Formation of OER and branching for possible subsequent reaction pathways.

R_f is the formation rate of OER, k_{O2} is the rate constant for reaction with oxygen, $[O_2]$ is the concentration of molecular oxygen, k_{3AP} is the rate constant for reaction with 3AP, [3AP] is the concentration of 3AP, and k_d is the rate constant for recombination (back reaction). The initial production rate of hydroxylamine ($R_H = \left(\frac{d[H]}{dt}\right)_0$) is therefore described by the following equation (derivation provided in **Text A2.1**):

$$R_H = \left(\frac{d[H]}{dt}\right)_0 = \frac{R_f[3AP]}{\left(\frac{(k_d + k_{O2}[O_2])}{k_{3AP}} + [3AP]\right)} = \frac{A[3AP]}{B+[3AP]} \qquad \text{(Eqn. 2.4)}$$

The parameter $A = R_f$ and parameter $B = \frac{k_d + k_{O2}[O_2]}{k_{3AP}}$. When $[O_2] = 0$ µM under nitrogen, $B = \frac{k_d}{k_{3AP}}$ which gives the half-saturation concentration for reaction of 3AP with one-electron reductants. When $[O_2] = 250$ µM under air-saturated conditions, the equation for B is rearranged to give $\frac{k_{O2}}{k_{3AP}} = \frac{(B_{250} - B_0)}{250}$.

The data under nitrogen plateaus by 600 µM and the resulting fit gave a half-saturation concentration (B) of 70 ± 8 µM and a rate of formation of one-electron reductants (A) of 21.1 ± 0.6 nM/s, somewhat higher than the previously published results of 40 ± 8 µM and 16.2 ± 0.7 nM/s respectively.[86] This difference could be attributed to the broader range of concentrations

tested in this iteration, allowing for a better fit than previous results (only tested up to 600 µM). In the presence of 250 µM O_2 (calculated based on temperature and solubility), competition between 3AP and molecular oxygen for OER is evidenced by the far lower values obtained for R_H. For this data, the fit gave B = 2600 ± 1200 µM and A = 39 ± 13 nM/s; the very large uncertainty could be attributed to not reaching rate saturation over the concentration range of 3AP investigated, in accordance with previous results.[86] Restricting the fit with A = 21.1 nM/s (from fit to 0 µM molecular oxygen) gives B = 1100 ± 85 µM, which is more in line with that observed visually for the half-saturation concentration and fits within the expected error of the data. These data provide strong evidence that 3AP and molecular oxygen are competing for the same pool of OER. Further, molecular oxygen and 3AP are highly effective quenchers of both excited singlet and triplet states with rate constants on the order of 10^9 $M^{-1}s^{-1}$ or more[194], primarily via mechanisms not involving electron transfer. These results provide further evidence that the excited states giving rise to the OER must be relatively short-lived and are thus not originating from long-lived triplet states.[192,194,199]

The concentration dependence of fluorescamine was also examined to ensure that derivatization of hydroxylamine was complete. This was achieved by irradiating 10 mg/L SRFA with 600 µM 3AP (with 325 nm cut-off filter for 15 minutes) but varying the concentration of fluorescamine used to derivatize the sample (**Figure 2.6**). The emission was linear up to ~0.8 mM fluorescamine and then plateaued after 1 mM, indicating that 1 mM was sufficient to derivatize 600 µM 3AP.

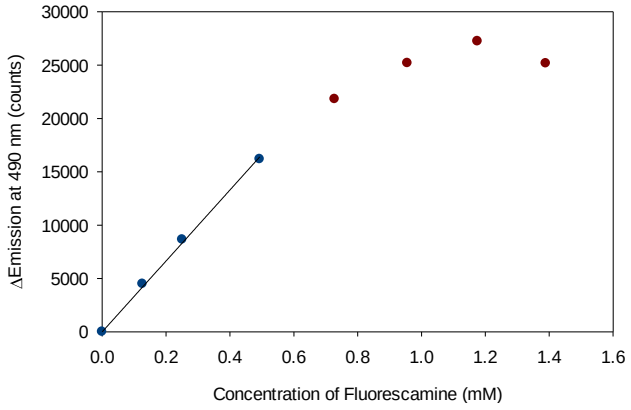

Figure 2.6. Blank subtracted emission intensities obtained for hydroxylamine derivatization in irradiated 10 mg/L SRFA using various concentrations of fluorescamine. Emission intensity is linear with concentrations up to 0.5 mM with a fit of y = 33300(±600)x with an R2 of 0.99. Derivatization reaches maximum efficiency at around 1 mM.

The hydroxylamine technique is quite sensitive and can detect nanomolar concentrations of hydroxylamine. The limit of detection (LOD = 3(s/m)) and the limit of quantification (LOQ = 10(s/m)) were determined where s is the standard deviation of the blank signal and m is the slope of the standard curve. LOD and LOQ values were determined using at least two standard curves and are reported as the average ± standard deviation. The hydroxylamine method has a LOD of 310 ± 70 nM and a LOQ of 1000 ± 200 nM. Although the hydroxylamine method does not have the best sensitivity, the simplicity and ease of use of the hydroxylamine method outweigh the loss of sensitivity. Additionally, this issue could be solved for low absorbing samples by implementing longer irradiation times when necessary.

2.4.2 Unraveling Issues with Natural Waters

While utilizing the hydroxylamine method on natural waters (with the same conditions used for reference materials and extracts; 600 µM 3AP and 1 mM fluorescamine), it was initially discovered that natural water samples (NW) had lower apparent quantum yields of hydroxylamine (Φ_H) compared to the extracts (EX) of the same samples (**Figure 2.7**). This was

not expected as the EX should simply be the DOM of the sample, just without the extraneous dissolved components of the NW matrix, and it has been found that extracted material is representative of the original NW.[195] One theory that was tested was the possibility that the samples were releasing free amines, which could be released during irradiation of CDOM.[200] Fluorescamine can also derivatize these free amines, resulting in an undesired excess fluorescence signal, and the NW and EX could be releasing them to different degrees. To test for this, Delaware River (DR) St. 19 EX and NW were irradiated without 3AP and then derivatized and measured. Neither sample showed an increased fluorescence signal, indicating that no free amines were present (**Figure A2.5**).

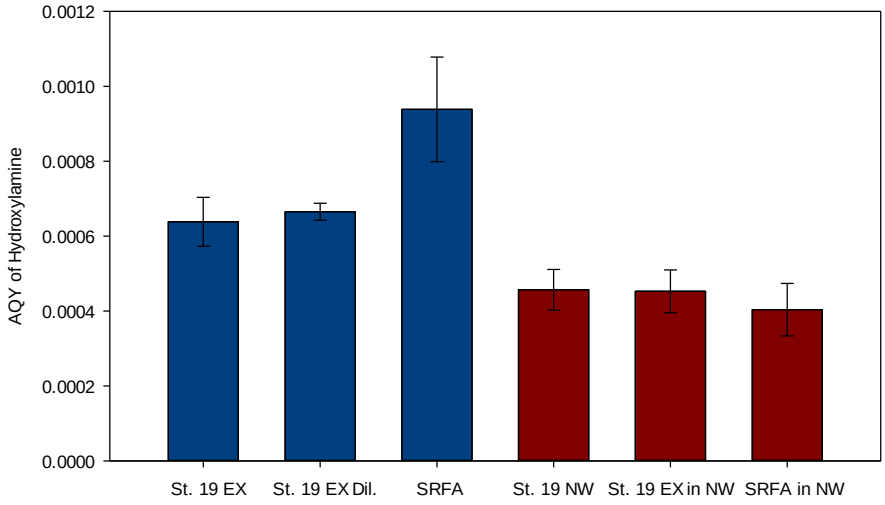

Figure 2.7. Φ_H obtained for 5 mg/L St. 19 EX, diluted (Dil) St. 19 EX, and 5 mg/L SRFA (blue) as well as Φ_H obtained for St. 19 NW, St. 19 EX in St. 19 NW and 5 mg/L SRFA in St. 19 NW (red). Absorbance of diluted St. 19 EX matched the absorbance of St. 19 NW. Error bars represent the standard deviation of triplicate measurements.

Further work focused on evaluating possible interferences due to the NW matrix. It was observed that during R_H measurements on NW that the pH of the sample would drop drastically following derivatization, which did not occur with reference materials or EX in buffer. Derivatization of nitroxide with fluorescamine results in the net release of protons, causing the pH of the solution to decrease. The derivatization process has been shown to be pH dependent,

with highest yields obtained between pH 7.5-9.5.[193] Therefore, the sudden change of pH was likely impeding the full completion of the derivatization process. To combat this and maintain the pH of the NW during the derivatization process, St. 19 NW was spiked with aliquots of a 50 mM borate buffer pH 11. Various volumes (25, 50, 75, and 100 µL) were tested to see which volume would result in the desired end pH of 8 post-derivatization. Emission signals of the buffered samples were enhanced indicating an improvement in derivatization, but this occurred for both non-irradiated (baseline measurement) and irradiated samples (**Figure 2.8**). Therefore, buffering the NW did not affect the overall value of R_H.

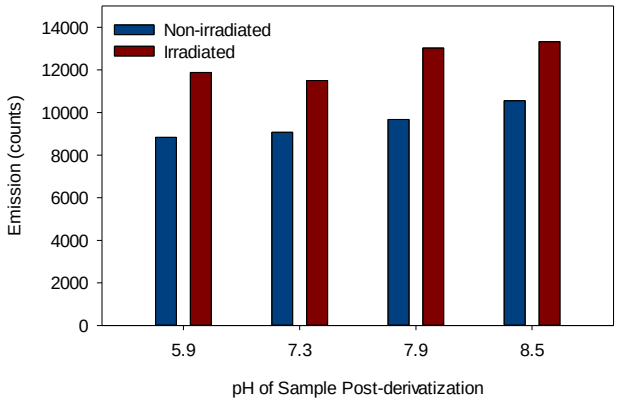

Figure 2.8. Emission of non-irradiated and irradiated St. 19 NW samples that were buffered and derivatized. Extent of buffering increases from left to right (25, 50, 75, and 100 µL of 50 mM borate buffer pH 11). Irradiation was conducted with 325 nm cut-off filter for 15 minutes.

Derivatization of 3AP by fluorescamine introduces a slight yellow color to the sample being tested. Upon visual examination of NW samples that were being measured for R_H, their color was noticeably lighter than reference material or EX samples. Absorbance scans of the NW in comparison to SRFA in buffer confirmed a lack of derivatization in the various NW samples tested (**Figure 2.9a**). The derivatization in just buffer alone shows what the absorbance should be for complete derivatization, and it is apparent that derivatization in SRFA in buffer follows that expected amount, since the absorbances match. All NW samples show a varying degree of

decreased absorbance, indicating less than complete derivatization. Since buffering seemed to be a step in the right direction, St.19 NW was buffered and the amount of fluorescamine was also doubled to see if more complete derivatization could be obtained. Although buffering alone did not improve the rates overall, when combined with increased concentrations of fluorescamine, the extent of derivatization rose to completion (**Figure 2.9b**), and therefore R_H values were enhanced (**Figure 2.10**).

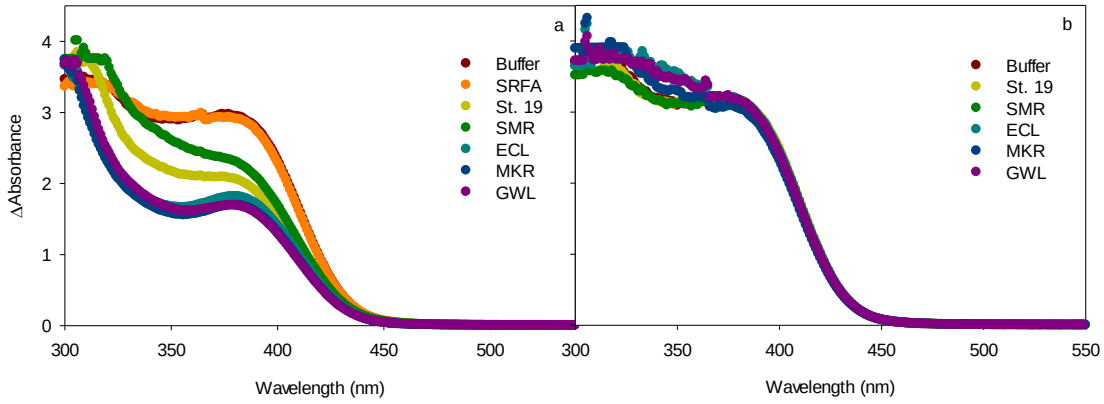

Figure 2.9. Absorbance of derivatized 3AP in various non-irradiated samples. Absorbance plotted is the absorbance of the derivatized sample minus the absorbance of the sample itself and therefore shows only the absorbance due to the derivatized 3AP. (a) Conditions for these samples are 600 μM 3AP, 1 mM fluorescamine, and no buffering for the natural waters. (b) Conditions for these samples are 600 μM 3AP, 2 mM fluorescamine, and buffering for the natural waters (~75 μL of 50 mM borate buffer pH 11).

Further tests were conducted where the concentration of 3AP was increased and the addition of an even higher concentration of fluorescamine was investigated. Increasing the concentration of the 3AP alone did not affect R_H and increasing the fluorescamine concentration beyond 2 mM also did not lead to any further enhancement (**Figure 2.10**). The enhanced conditions of buffering and the use of 2 mM fluorescamine were also tested on St. 19 EX to check for increases in rates, but no such increase was observed, further confirming that the enhanced conditions are only necessary for NW samples (**Figure 2.10**). The need for higher concentrations of fluorescamine could be due to undesired side reactions between fluorescamine

and secondary amines or ammonia which leads to non-fluorescent products.[201–203] Secondary amines can be present in NW samples since several anthropogenic contaminants are secondary amines.[204] It is unlikely that ammonia was an issue in the samples tested because the concentrations were minimal to none (**Figure A2.6**). Alternatively, something in the NW could be causing the hydrolysis of fluorescamine.[205]

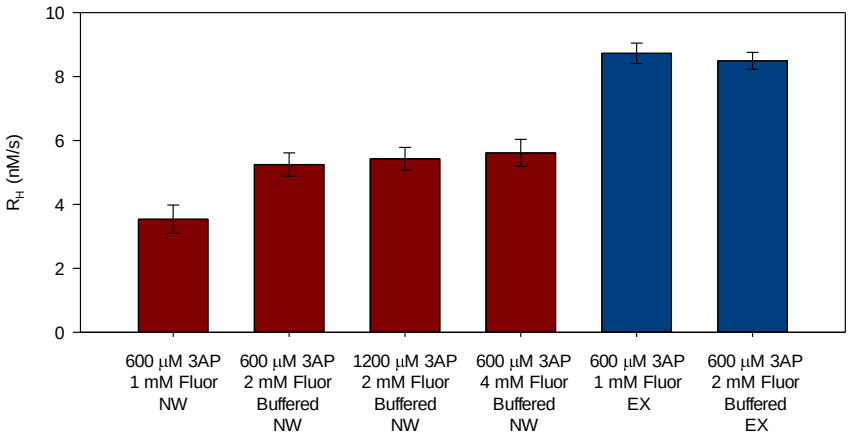

Figure 2.10. R_H in DR St. 19 NW (red) and DR St. 19 EX (blue) using various experimental conditions. Error bars represent standard deviation of triplicate measurements.

2.5 Conclusion

Measurements of photoproduced OER were successfully performed using the newly improved fluorescence method on a wide variety of reference materials, natural waters, and extracts. The hydroxylamine method provides reasonable estimates for $O_2^{\bullet-}$ production, is faster and easier to conduct than the traditional chemiluminescence-based method for $O_2^{\bullet-}$, and should be amenable to continuous measurement via flow-injection analysis (in a fashion like the chemiluminescence-based method). The sensitivity should be sufficient for application to most fresh and coastal waters, and with longer irradiation times, to open ocean waters.

Chapter 3: Correlations between the Production of One-electron Reductants with that of Hydrogen Peroxide and Superoxide

The majority of this chapter has been published in reference 260:

Le Roux, D. M.; Powers, L. C.; Blough, N. V. Photoproduction Rates of One-Electron Reductants by Chromophoric Dissolved Organic Matter via Fluorescence Spectroscopy: Comparison with Superoxide and Hydrogen Peroxide Rates. *Environ. Sci. Technol.* **2021**, *55* (17), 12095–12105. https://doi.org/10.1021/acs.est.1c04043.

I performed all experiments and data analysis and prepared the first draft of the manuscript. Dr. Powers and Dr. Blough assisted in data analysis and editing the manuscript.

3.1 Abstract

One-electron reductants (OER) photoproduced by chromophoric dissolved organic matter (CDOM) have been shown to be likely precursors for formation of superoxide ($O_2^{\bullet-}$) and therefore hydrogen peroxide (H_2O_2). The improved nitroxide radical probe method that was developed, as described in Chapter 2, was used to determine the photoproduction rates of OER from a diverse set of CDOM samples. Values for the production rates of OER (hydroxylamine), $O_2^{\bullet-}$, and H_2O_2 (R_H, $R_{O2\bullet-}$, and R_{H2O2}) have a similar wavelength dependence, indicating a common origin. Correlations between the yields of OER and H_2O_2 to various optical properties of CDOM suggest that lower molecular weight components of CDOM are more efficient at producing OER and H_2O_2. If all of the OER react with molecular oxygen to produce $O_2^{\bullet-}$, the simplest mechanism predicts that R_H/R_{H2O2} and $R_{O2\bullet-}/R_{H2O2}$ should be equal to two. However, measurements reveal R_H/R_{H2O2} values as high as sixteen (5.7-16), consistent with prior results, and $R_{O2\bullet-}/R_{H2O2}$ values as high as eight (5.4-8.2). These results indicate that a substantial fraction of $O_2^{\bullet-}$ (65-88%) is not undergoing dismutation.

3.2 Introduction

Since CDOM spectra ($a(\lambda)$) appear to have an exponential shape with wavelength, they are often described with the following equation:

$$a(\lambda) = a(\lambda_{ref})e^{-S(\lambda - \lambda ref)} \quad \text{(Eqn. 3.1)}$$

where λ_{ref} is the reference wavelength and S (nm^{-1}) is the spectral slope coefficient. Variation in S between studies are typically due to the wavelength region over which S is determined.[9] S is often reported over shorter wavelength regions, such as 275 – 295 nm or 350 – 400 nm, although the larger range from 300-700 nm is also used. Helms et al. demonstrated that $S_{275–295}$ and the slope ratio (S_R; S determined over 275 – 295 nm divided by that from 350 – 400 nm) were correlated to molecular weight of DOM for a variety of samples.[206] Lower values of S are often associated with high molecular weight (HMW) DOM and high values of S are associated with low molecular weight (LMW) DOM.[206] For $S_{300–700}$, it is typically highest for ocean/offshore samples (> 0.020 nm^{-1}), lower for coastal/inshore samples (0.014 – 0.018 nm^{-1}), and lowest for freshwater samples (< 0.014 nm^{-1}).[9] Decreasing values of S result from increasing long-wavelength absorbance.

The E2/E3 ratio is the ratio between the absorbance at 254 nm and the absorbance at 365 nm and it has been shown to be inversely correlated with the molecular weight of DOM[207] and also inversely correlated with the quantum yield of H_2O_2 production for DOM isolates and humic substances.[76,165] Specific UV absorbance at a particular wavelength (λ) ($SUVA_\lambda$; absorbance at a given wavelength, usually 254 or 280 nm, normalized to pathlength and DOC concentration) has been used as an indicator of DOM aromaticity, wherein high $SUVA_{254}$ values indicate more aromaticity.[208] A positive linear relationship has been observed between $SUVA_{280}$ and the production of H_2O_2[165] as well as for $O_2^{\bullet-}$.[209] Mass-normalized absorbance values (a* =

a_{350}/[DOC]) showed no relationship with H_2O_2 photoproduction in a sample set containing riverine and coastal seawaters.[210] Increased values of normalized absorbances have been shown to be associated with increased molecular weight and aromaticity.[9] Results obtained from Northwestern Patagonia showed that higher molecular weight, more humic material of streams and shallow lakes were more productive than lower molecular weight material from deep lakes, based on a_{254} values.[211]

Fluorescence measurements have not been widely used in evaluating ROS photoproduction rates. The fluorescence quantum yield (FQY), which is a ratio of the light emitted from a sample compared to how much light was absorbed, has been widely measured and is calculated via the following equation:

$$FQY(\lambda_{ex}) = \left(\frac{F_{s(int)}(\lambda_{ex})}{F_{QS(int)}(\lambda_{ex_{350nm}})} * \frac{A_{QS}(\lambda_{ex_{350nm}})}{A_s(\lambda_{ex})}\right) * 0.51 \qquad \text{(Eqn. 3.2)}$$

where $F_{s(int)}$ and $F_{QS(int)}$ are the integrated emission intensities of the sample and quinine sulfate (QS), respectively, at the particular excitation wavelength (λ_{ex}). A_{QS} and A_s are the absorbance values of QS and the sample, respectively. The value 0.51 is the published quantum yield of QS.[212–214]

Fluorescence tends to increase with decreasing molecular weight, likely because of higher rates of intramolecular quenching in higher molecular weight material.[50] In one study, the sample with the highest integrated fluorescence emission from visible excitation wavelengths had the highest H_2O_2 photoproduction rate.[210] The fluorescence quantum yield has been found to be positively correlated to H_2O_2 production for various lake waters.[215]

The summary of the trends of optical properties with structural features of DOM and the production of H_2O_2 are show in **Table 3.1**. Overall, the fluorescence-based correlations are consistent in that lower molecular weight, higher fluorescing structures produce more H_2O_2.

Absorbance-based molecular weight correlations are much more conflicted where some metrics (E2/E3, a_{254}, $SUVA_{\lambda}$) showed direct relation to increased production of H_2O_2 and/or $O_2^{\bullet-}$ while some metrics (E2/E3) showed the opposite or even none at all (spectral slope, slope ratio, and a^*). Absorbance-based metrics for structural properties of DOM have been highly criticized due to a wide variety of possible interferences, particularly in natural waters.[216] For instance, anions like nitrate, nitrite, and halides absorb in the UV range which will affect the absorbance spectra.[217,218] CDOM can also chelate various cations and specifically iron is known to enhance absorbance measurements.[208,219,220] While iron has received the most attention, the presence of magnesium[221] and copper[222] can also impact optical measurements. Changes in pH also significantly change CDOM optical properties[181,223], whereby DOM absorbance typically increases with increasing pH due to the deprotonation of acidic moieties.[224] Other peculiar situations involve algal based samples that contain a high proportion of mycosporine-like amino acids[225] and samples with high phenolic content which will also affect spectra.[226,227] Additional considerations include the fact that not all carbon absorbs[9] and that these metrics do not necessarily correlate to particular functional groups which may be an important consideration in relating optical properties to photochemical reactions.

Table 3.1. Relation of Optical Properties to CDOM Structure and Trends with ROS

Optical Property	Relation to Structure	Trend with ROS and Reference
$S_{300\text{-}700}$	↑ value ↓ MW	None (Le Roux et al., 2021)
S_R	↑ value ↓ MW	None (Le Roux et al., 2021)
E2/E3	↑ value ↓ MW	Inverse H_2O_2 (Dalrymple, 2010) Inverse H_2O_2 (Sharpless et al., 2014) Direct H_2O_2 and OER (Le Roux et al., 2021)
a_{254}	↑ value ↓ MW	Direct H_2O_2 (Garcia et al., 2019)
Fluorescence Intensity	↑ value ↓ MW	Direct H_2O_2 (O'Sullivan et al., 2005)
FQY	↑ value ↓ MW	Direct H_2O_2 (Scully et al., 1996) Direct H_2O_2 and OER (Le Roux et al., 2021)
$SUVA_\lambda$	↑ value ↑ aromaticity	Direct H_2O_2 (Sharpless et al., 2014) Direct H_2O_2 and $O_2^{\bullet-}$ (Fuji and Otani, 2017)
($a^* = a_{350}/[DOC]$)	↑ value ↑ MW and aromaticity	None (O'Sullivan et al., 2005)

As discussed in Chapter 1, the generation of $O_2^{\bullet-}$ and H_2O_2 involves an initial absorption of light (hν) by CDOM, resulting in the formation of excited singlet states ($^1CDOM^*$).[15,52] Based on current evidence, intramolecular electron transfer results in the formation of one-electron reductants ($CDOM^{D\bullet+/A\bullet-}$; OER).[78,86] OER then react with dissolved molecular oxygen to form $O_2^{\bullet-}$ which can then undergo dismutation to form H_2O_2.[7,81,84] Prior work that compared the production rate of OER (R_H) to that of H_2O_2 (R_{H2O2}) for standard humic and fulvic materials from the Suwannee River obtained higher values than expected based on stoichiometry for dismutation (value of two), with some values reaching up to thirteen.[86]

Here the work has been expanded with an increased sample scope. R_H and R_{H2O2} values have been determined for a variety of samples including Suwannee River fulvic acid (SRFA) and natural organic matter (SRNOM), Elliott Soil humic acid (ESHA), exudate from the brown algae *Sargassum natans*, a natural water and extract (C-18 solid phase) from the Delaware River, natural waters from various lakes in New Jersey, and a natural water and extract from St. Mary's River in Maryland. R_H were compared with R_{H2O2} and all samples exhibited ratios far greater

than two, in accordance with past results.[86] Comparisons of yields to optical properties of CDOM indicate higher production of these species from lower molecular weight species. Salinity and the addition of a metal chelator, to test for matrix effect issues in natural waters, have only a slight impact on the results. To delve deeper into the relationship between the reactions as described, preliminary work acquired $R_{O2}^{\bullet-}$ for SRFA and SRNOM. Presented herein are the first measurements of the production rates of all three species under identical conditions, as well as the first direct measurements of the polychromatic wavelength dependence of $R_{O2}^{\bullet-}$ using multiple long-pass cut-off filters.

3.3 Materials and Methods

3.3.1 Materials

Boric acid, sodium carbonate, sodium acetate, monobasic sodium phosphate, sodium hydroxide, phosphoric acid, sulfuric acid, sea salt (S9883), fluorescamine, 3-amino-2,2,5,5-tetramethyl-1-pyrrolidinyloxy (3AP), and 0.1 N potassium permanganate ($KMnO_4$) were purchased from Millipore Sigma. Sodium dithionite was purchased from Acros Organics. Hydrogen peroxide and sodium chloride were purchased from EMD. Acetonitrile, acetone, and ethanol were purchased from Fischer. 10-methyl-9-(p-formylphenyl) acridinium carboxylate trifluoromethanesulfonate (acridinium ester or AE) was obtained from Waterville Analytical Co. 2-methyl-6-(4-methoxyphenyl)-3,7-dihydroimidazo[1,2-a]pyrazin-3(7H)-one) (methyl Cypridina luciferin analogue or MCLA) was purchased from TCI Chemicals. Diethylenetriaminepentaacetic acid (DTPA) was purchased from Fluka. Suwannee River fulvic acid (SRFA; 2S101F), Suwannee River natural organic matter (SRNOM; 2R101N), Ellicott soil humic acid (ESHA; 1S102H) were purchased from the International Humic Substance Society.

Sargassum was sampled in the North Atlantic Ocean, 9 km off the coast of Bermuda, and exudates were collected by solid phase extraction during outdoor leaching experiments described in detail previously.[227] Natural water (NW) from the Delaware River was collected in August of 2006 (St. 19; 40.1 N, -74.8 W). Natural waters from various lakes in northern New Jersey were collected in November and December of 2019: Echo Lake Reservoir (ECL; 41.0, -74.4), Greenwood Lake (GWL; 41.2, -74.4) and Monksville Reservoir (MKR; 41.1, -74.3). Natural water from St. Mary's River in Maryland was collected in January of 2020 (SMR; 38.2, -76.5). C-18 solid phase extractions (EX) were conducted as described previously in section 2.3.2.[195] Purified water (18 MΩcm) was obtained from a Milli-Q purification system.

3.3.2 Sample Preparation

Stock solutions of extracts and reference materials were prepared by diluting/dissolving the extract or reference material in MQ water. These stocks were adjusted to pH 7 using NaOH and HCl and filtered using pre-rinsed 0.2 μM nylon filters. Dilutions of these stocks at desired concentrations for experiments were prepared by diluting the stock solutions with 50 mM borate buffer at a pH of 8 unless otherwise noted. Natural waters were filtered with pre-rinsed 0.2 μm nylon filters and used as is.

To explore the impact of salinity, solutions of 50 mM borate buffer at a pH of 8 with sodium chloride and Sigma Aldrich "Sea Salt" (S9883) concentrations of 18 and 28 ppt were prepared. St. 19 EX samples at concentrations of 5 mg/L were prepared by bringing up the EX in these buffered salt solutions. R_H and R_{H2O2} were measured as described below. The sodium chloride and sea salt had been baked for 24 hours prior to being used to remove any trace organic material. Sonication was done to aid in dissolution and the salt solutions were filtered through

pre-rinsed 0.2 μM nylon filters before use.

To explore the impact of metal chelation, a stock solution of 3.57 mM DTPA was prepared by dissolving the solid in MQ water. Aliquots of the stock were added to St. 19 EX and St. 19 NW to a concentration of 50 μM and were then allowed to sit at 4°C for 24 hours to ensure complexation of metals. R_H and R_{H2O2} were then measured as described below.

3.3.3 Measurement of One-electron Reductants

The production of OER (R_H) was measured as described in section 2.3.4.

3.3.4 Measurement of Hydrogen Peroxide

H_2O_2 was measured through a chemiluminescent reaction with AE (**Figure A3.1**) in a FeLume, a flow-injection analysis instrument from Waterville Analytical Co. (**Figure A3.2**). For freshwater and buffered samples, the carrier was 0.1 M HCl, the buffer was 0.1 M sodium carbonate at a pH of 11.7, and the reagent AE was prepared at 5 μM in 1 mM phosphate buffer at a pH of 3.[228,229] For higher salinity samples, the HCl carrier was increased to 0.3 M, the pH of the sodium carbonate buffer was lowered to 10.7, and the AE concentration was lowered to 1-2 μM in order to prevent precipitation of salts. The photomultiplier tube was set at a voltage of 950 V and an integration time of 400 ms for freshwater and buffered samples. The voltage was increased to 1050 V for higher salinity samples. All of these solutions were drawn into the FeLume system using a peristaltic pump with Teflon tubing.

Standard concentrations of H_2O_2 for measurement were prepared from a stock solution whose concentration was monitored spectrophotometrically ($\varepsilon = 38.1 \pm 1.4\ M^{-1}cm^{-1}$ at 240 nm).[230] This stock was prepared by dilution from a ~30% solution. The H_2O_2 concentration of the ~30% bottle was more specifically determined via potassium permanganate titration (**Text**

A3.1). A concentration of 31.6 ± 0.2 % was obtained. The molar extinction coefficient of H_2O_2 was then confirmed by measuring the absorbance of multiple prepared concentrations (**Figure A3.3**). An extinction coefficient of 40.4 ± 0.3 $M^{-1}cm^{-1}$ (0.5%) at 240 nm was obtained, which differs from the published literature value above by 6%.

To determine R_{H2O2}, a 1 cm quartz cuvette was filled with the sample and irradiated using the lamp, water jacket, and filters as describe above. R_{H2O2} was calculated from the linear regression of H_2O_2 yield over the course of a fifteen-minute irradiation.

3.3.5 Measurement of Superoxide

$O_2^{\bullet-}$ was measured via the chemiluminescent reaction with MCLA (**Figure A3.4**) in the FeLume system (**Figure A3.5**). It was set up to continuously take in MCLA and sample with a peristaltic pump and Teflon tubing with a total flow rate of 6.6 mL/min. MCLA was prepared at 2.5 µM in 500 mM sodium acetate buffer with 50 µM DTPA at a pH of 6.[77,231] A $O_2^{\bullet-}$ stock was generated by the photolysis of a solution of 6 M ethanol, 41 mM acetone, 30 µM DTPA in 1 mM borate buffer at a pH of about 12.5 in a cuvette with a mercury pen-lamp (**Figure A3.6, A3.7**).[231,232] The concentration of the $O_2^{\bullet-}$ stock was monitored spectrophotometrically (ε = 2183 $M^{-1}cm^{-1}$ at 240 nm)[84] with an Ocean Insight DH mini light source connected to an Ocean Optics USB2000 spectrometer (**Figure A3.6**) hooked up to a computer with the SpectraSuite program. When the $O_2^{\bullet-}$ stock concentration in the solution reached ~50 µM, a small volume (µL) was taken and added to ~20 mL of sample to prepare a standard in the nanomolar range. The standards were continuously stirred and taken into the instrument and the signal was monitored as the $O_2^{\bullet-}$ decayed. Linear extrapolation of the plot of the natural log of the signal versus time (~60 s) was used to determine the value of the initial signal at the time of $O_2^{\bullet-}$ injection (t=0).

To quantify $R_{O2\bullet-}$, about 4 mL of sample was placed in a 1 cm cuvette and the sample line

was inserted into the cuvette. The cuvette was placed into the light and the production was monitored over time. Approximately the first 15 seconds of the observed increase in signal over time was used to calculate $R_{O2^{\bullet-}}$ (**Figure A3.8**).

3.3.6 Determination of Optical Properties

Absorbance measurements were conducted on a Shimadzu UVPC 2401 benchtop spectrophotometer in a 1 cm cell. The instrument was always baselined to air and blank measurements (MQ or buffer) were taken and were subtracted from absorbance spectra. Spectral slopes were determined using nonlinear least squares fitting to the exponential function (Equation 3.1) in SigmaPlot®.

Fluorescence excitation-emission spectra (EEMs) were conducted with a Horiba Fluoromax-4. Excitation was scanned from 300-500 nm every 10 nm and the emission was scanned from 300-700 nm every 1 nm. Band passes were 4 nm and the integration time was 0.2 s. First and second order Rayleigh masking settings, within the program, were applied to each scan. The fluorescence of 10 ppb quinine sulfate (QS) in 1 N H_2SO_4 was measured using an excitation wavelength of 350 nm with emission scanned from 290-700 nm. Fluorescence quantum yields (FQY) were calculated using Equation 3.2.

3.3.7 Apparent Quantum Yield Calculations

Apparent quantum yields for hydroxylamine, H_2O_2, and $O_2^{\bullet-}$ were calculated as described in section 2.3.5.

3.4 Results and Discussion

3.4.1 Polychromatic Wavelength Dependence of Rates and Ratios

The wavelength dependence of the production of H_2O_2 has been investigated extensively and has been shown to decrease approximately exponentially through the ultraviolet range, with little to no production in the visible.[233,215,234,235,106,236,210,237,88,238,87] Prior results from limited monochromatic studies have shown that the value for R_H/R_{H2O2} is retained despite the wavelength of light used for irradiation.[78,86,239] This work is the first report of R_H, R_{H2O2}, and $R_{O2^{\bullet-}}$ measurements under identical conditions on the same sample and the first report of the polychromatic wavelength dependence of $R_{O2^{\bullet-}}$ that was acquired directly and not estimated from R_{H2O2} data. The wavelength dependence is similar for all three rates (**Figure 3.1a-c**), with all decreasing proportionally with longer wavelength cut-off filters. Therefore, specific ranges of wavelengths do not favor R_H, $R_{O2^{\bullet-}}$, or R_{H2O2} over another which further supports that the reactions of the three species are inter-related.

Photochemical efficiency is the probability that absorption of radiation by CDOM will lead to a photochemical product. This is typically determined as the apparent quantum yield (AQY; $\Phi(\lambda)$), defined as the ratio of the moles of product produced to the moles of photons absorbed by the sample.[240] **Figure 3.1d-f** provide the wavelength dependence of the Φ values.

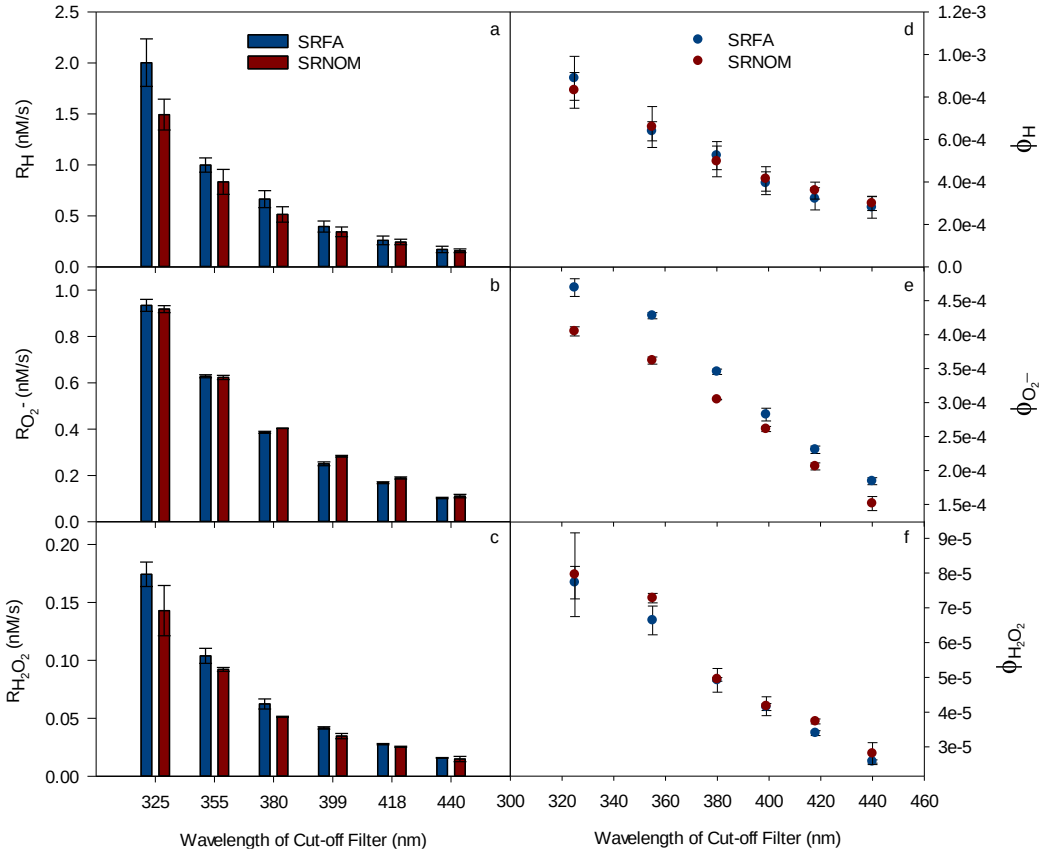

Figure 3.1. (a) R_H, (b) $R_{O2\bullet-}$, (c) R_{H2O2}, (d) Φ_H, (e) $\Phi_{O2\bullet-}$, and (f) ΦH_2O_2 for 1 mg/L SRFA and SRNOM. Error bars for the rates represent standard deviations of triplicate measurements.

These results are similar to the few polychromatic studies that exist for the wavelength dependence of Φ_{H2O2}, although they fall towards the lower end of the values.[87,88,210,238] This may be attributed to the use of an integration range of 300-800 nm here, which is significantly larger than in other studies. Additionally, a cut-off filter of no shorter than 325 nm was explored here and most works have studied as low as 280 nm, which is much more photochemically efficient and these lower wavelengths give the spectra a more exponential trend.[87,88,210,238]

When the production rates are related through ratios ($R_{O2\bullet-}$ to R_H and R_{H2O2}; **Figure 3.2**), a ratio of about one to two is obtained for $R_H/R_{O2\bullet-}$ which indicates that $O_2^{\bullet-}$ measurements are close in magnitude to those of OER, as expected. The slightly lower $R_{O2\bullet-}$ compared to R_H could

be due to the inability to completely capture an accurate $R_{O2^{\bullet-}}$. The rates reported here are "net" in that some unavoidable loss occurs as the $O_2^{\bullet-}$ travels from the sample to the reagent and detector within the FeLume. Alternatively, small systematic variations in the calibration of either R_H or $R_{O2^{\bullet-}}$ could be possible, particularly for $R_{O2^{\bullet-}}$ due to the difficult nature of calibrating for $O_2^{\bullet-}$. In contrast, a ratio of about eleven is obtained for R_H/R_{H2O2}, consistent with previous work[86], with a value of about six to eight obtained for $R_{O2^{\bullet-}}/R_{H2O2}$, further confirming that $R_{O2^{\bullet-}}$ cannot be simply estimated as twice R_{H2O2}, which has been traditionally assumed.[87,241]

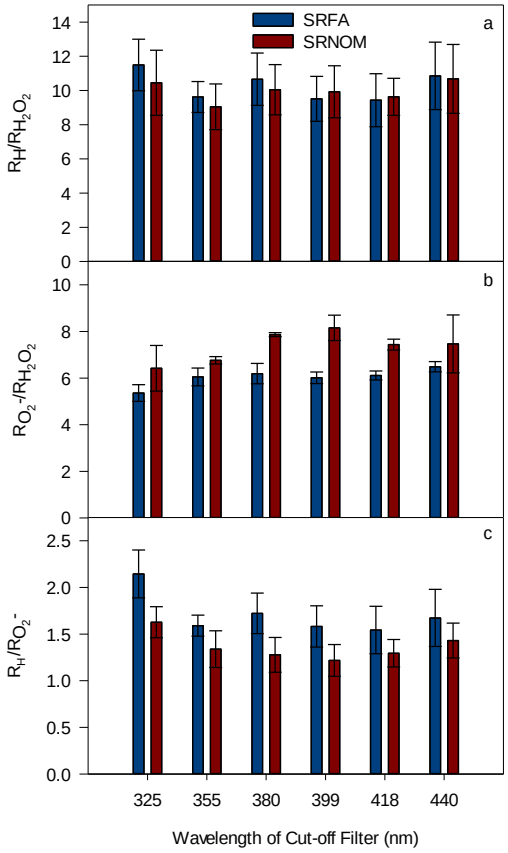

Figure 3.2. (a) R_H/R_{H2O2}, (b) $R_{O2^{\bullet-}}/R_{H2O2}$ and (c) $R_H/R_{O2^{\bullet-}}$ for SRFA and SRNOM. Error bars represent propagation of standard deviation of triplicate measurements for each rate.

3.4.2 Comparison of Apparent Quantum Yields and Ratios Among Samples

R_H and R_{H2O2} were determined for SRFA, SRNOM, ESHA, a natural water and an extract from the Delaware River (St. 19), exudate from *Sargassum*, natural waters from lakes and

reservoirs in northern New Jersey [Echo Lake Reservoir (ECL), Greenwood Lake (GWL) and Monksville Reservoir (MKR)], and a natural water and an extract from St. Mary's River (SMR) in Maryland (**Table 3.2**). For all samples, R_H/R_{H2O2} is greater than two and varies from a value of five to sixteen. Φ_H and Φ_{H2O2} also differ significantly among the samples, from a value of 1.7 to 17 x 10^{-4} for Φ_H and 0.21 to 1.03 x 10^{-4} for Φ_{H2O2}. Literature values for polychromatic Φ_{H2O2} values for a variety of natural waters vary significantly.[87,88,210,215] The results obtained here are on the lower end of published values, which could be due to the differences in experimental methods as described above (wavelength of cut-off filter and integrated wavelength range).

R_H/R_{H2O2} values for SRFA and SRNOM are comparable to one another and to previously published results for SRFA and SRHA.[86] ESHA differs significantly from SRFA and SRNOM as it has a slightly higher R_H/R_{H2O2} yet significantly lower Φ_H and Φ_{H2O2} values. The exudate from *Sargassum* is similar to ESHA in that Φ_H and Φ_{H2O2} are low compared to all of the other samples, however *Sargassum* has an overall R_H/R_{H2O2} of five compared to fifteen obtained for ESHA. This difference could be related to the fact that DOM from *Sargassum* exudates has a high phenolic content and very different molecular properties when compared to standard reference materials.[227] The natural waters and their respective extracts from St. 19 and SMR have fairly close values for both Φ_H and Φ_{H2O2}. The natural water samples from New Jersey have varying values for both Φ_H and Φ_{H2O2}. MKR has the highest Φ_H and Φ_{H2O2} values among the NJ samples tested.

Based on the competition experiment described in section 2.4.1, photoproduced OER that react with 3AP to produce hydroxylamine under anaerobic conditions, should react with molecular oxygen to produce $O_2^{\bullet-}$ under aerobic conditions and assuming the stoichiometry of two $O_2^{\bullet-}$ molecules to produce one H_2O_2, the fraction of $O_2^{\bullet-}$ that is lost to other oxidative

processes (P_{O2^-}) can be determined using the following equation (derivation provided in **Text A3.2**):[86]

$$\frac{R_H}{R_{H2O2}} = \frac{2R_{O_2^-(total)}}{\left[R_{O_2^-(total)}\left(1-P_{O_2^-(oxidative)}\right)\right]} \quad \text{(Eqn. 3.3)}$$

The P_{O2^-} (converted to percent) values range from 65 to 88%, consistent with past results and suggesting that a significant portion of $O_2^{\bullet-}$ is lost through oxidative pathways.[7,77,86,241]

Table 3.2. R_H and R_{H2O2}, Apparent Quantum Yields, and Ratios for Various Samples

Sample	R_H (nM/s)	R_{H2O2} (nM/s)	R_{EX} (nM/s) ($x10^4$)	Φ_H ($x10^{-4}$)	Φ_{H2O2} ($x10^{-4}$)	R_H/R_{H2O2}	P_{O2-} (%)
SRFA	20 ± 2	1.7 ± 0.1	2.3	9 ± 1	0.76 ± 0.05	12 ± 2	83
SRNOM	15 ± 1	1.4 ± 0.2	1.8	8.3 ± 0.8	0.8 ± 0.1	11 ± 2	81
ESHA	10.9 ± 0.5	0.74 ± 0.02	3.6	3.0 ± 0.1	0.21 ± 0.01	15 ± 1	86
Sargassum	6.4 ± 0.5	1.13 ± 0.03	3.8	1.7 ± 0.1	0.30 ± 0.008	5.7 ± 0.4	65
St. 19 (EX)	8.7 ± 0.3	0.67 ± 0.03	1.2	7.4 ± 0.3	0.58 ± 0.03	13.0 ± 0.8	85
St. 19 (NW)	5.3 ± 0.4	0.39 ± 0.02	0.61	8.6 ± 0.6	0.64 ± 0.03	13 ± 1	85
SMR (EX)	3.0 ± 0.3	0.21 ± 0.02	0.27	11 ± 1	0.75 ± 0.06	14 ± 2	86
SMR (NW)	2.1 ± 0.3	0.18 ± 0.01	0.22	10 ± 2	0.85 ± 0.05	11 ± 2	82
ECL (NW)	8.3 ± 0.4	0.661 ± 0.007	1.2	6.8 ± 0.3	0.544 ± 0.006	12.6 ± 0.5	84
GWL (NW)	4.7 ± 0.6	0.45 ± 0.01	0.61	8 ± 1	0.74 ± 0.02	11 ± 1	81
MKR (NW)	4.5 ± 0.6	0.277 ± 0.003	0.27	17 ± 2	1.03 ± 0.01	16 ± 2	88

Uncertainties in the rates represent the standard deviation of triplicate measurements.
Uncertainties were propagated for derived values.

3.4.3 Correlations Between Apparent Quantum Yields and Optical Properties

Variation in the Φ_H and Φ_{H2O2} values among the samples studied could be due to differences in structure or composition of the samples. Optical properties, such as absorbance and fluorescence parameters, have been utilized to relate photochemical reactions to the composition of CDOM.[15] To probe this, several optical properties were obtained for the samples using absorbance and excitation-emission spectra. Φ_H and Φ_{H2O2} were compared to the ratio of the absorbance value at 250 nm to the absorbance value at 365 nm (E_2/E_3), spectral slope ($S_{300-700}$), spectral slope ratio ($S_{275-295}/S_{350-400}$), and fluorescence quantum yield (FQY). A weak correlation was observed for Φ_H and Φ_{H2O2} with E_2/E_3 (R^2 = 0.55 and 0.62, respectively) and FQY (R^2 = 0.40 and 0.39, respectively) (**Figure 3.3**), but no obvious correlation was observed for Φ_H and Φ_{H2O2} and $S_{300-700}$ or $S_{275-295}/S_{350-400}$ (**Figure 3.4**). E_2/E_3, $S_{300-700}$, $S_{275-295}/S_{350-400}$, and FQY all tend to increase with decreasing molecular weight[15,206], so it is interesting that the correlations are stronger with some of these optical properties over others. It has been argued that the more discrete optical properties (E_2/E_3 and $S_{275-295}/S_{350-400}$) are more viable parameters to compare to as opposed to spectral slopes over broad wavelength regions because the analysis of a wide range of wavelengths would be less sensitive to any subtle changes in absorbance.[206] Correlations to $S_{275-295}/S_{350-400}$ were found to be minimal here, but this could be due to the very small range that the samples fall within (~0.8-1.0). Another aspect to note is that the E_2/E_3 includes the absorbance at 250 nm whereas the spectral slope was calculated from 300-700 nm, indicating that the absorbance around 250 nm is of more importance than other wavelengths/regions when making correlations with Φ_H and Φ_{H2O2}. Since the Φ_H and Φ_{H2O2} increase with decreasing molecular weight, the importance of the region around 250 nm could be due to the fact that smaller molecular weight species tend to absorb at shorter wavelengths.

Based on the correlations, it appears that Φ_H and Φ_{H2O2} also increase with decreasing molecular weight, though very little about these correlations exist in the literature. Dalrymple et al. found the opposite trend for Φ_{H2O2} although their range in E_2/E_3 was considerably smaller.[76] Their samples only consisted of extracts from the International Humic Substance Society, whereas the sample set here includes natural waters. Furthermore, their Φ_{H2O2} were based on the irradiation range of approximately 300-400 nm whereas ours are calculated over the range of 300-800 nm. A linear relationship has been found previously between H_2O_2 production and fluorescence, in accordance with the results in **Figure 3.3**.[215]

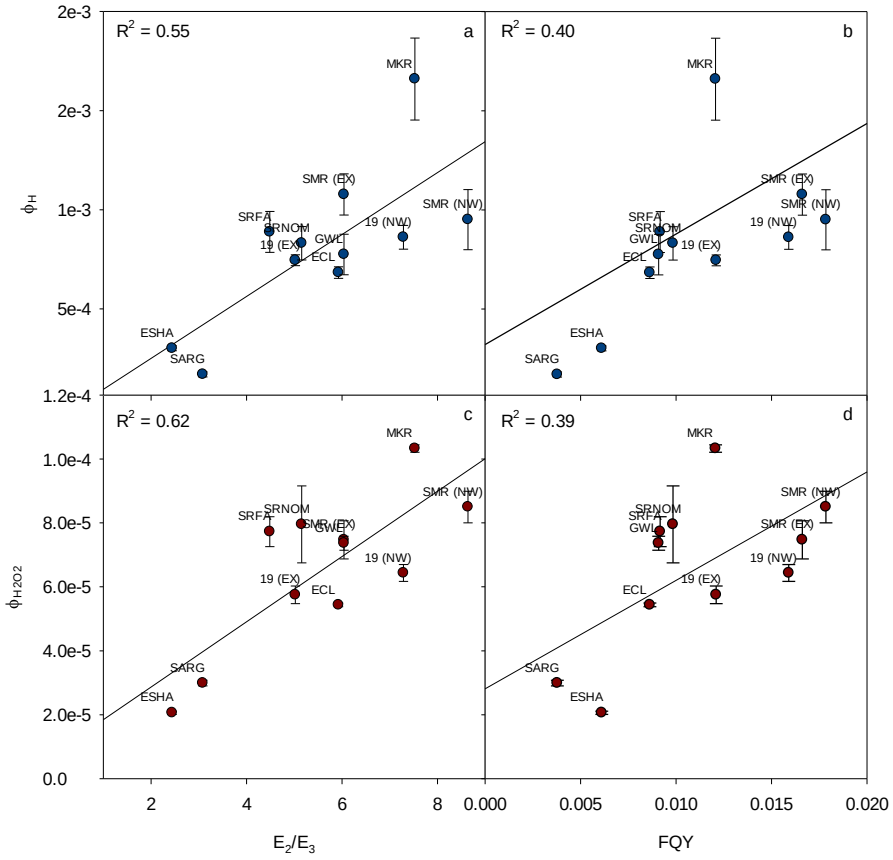

Figure 3.3. Relationships between optical properties and apparent quantum yields: (a) Φ_H vs. E2/E3 (b) Φ_H vs. FQY (c) Φ_{H2O2} vs. E2/E3 and (d) Φ_{H2O2} vs. FQY for all samples given in Table 3.2. Error bars represent propagation of standard deviation of triplicate measurements.

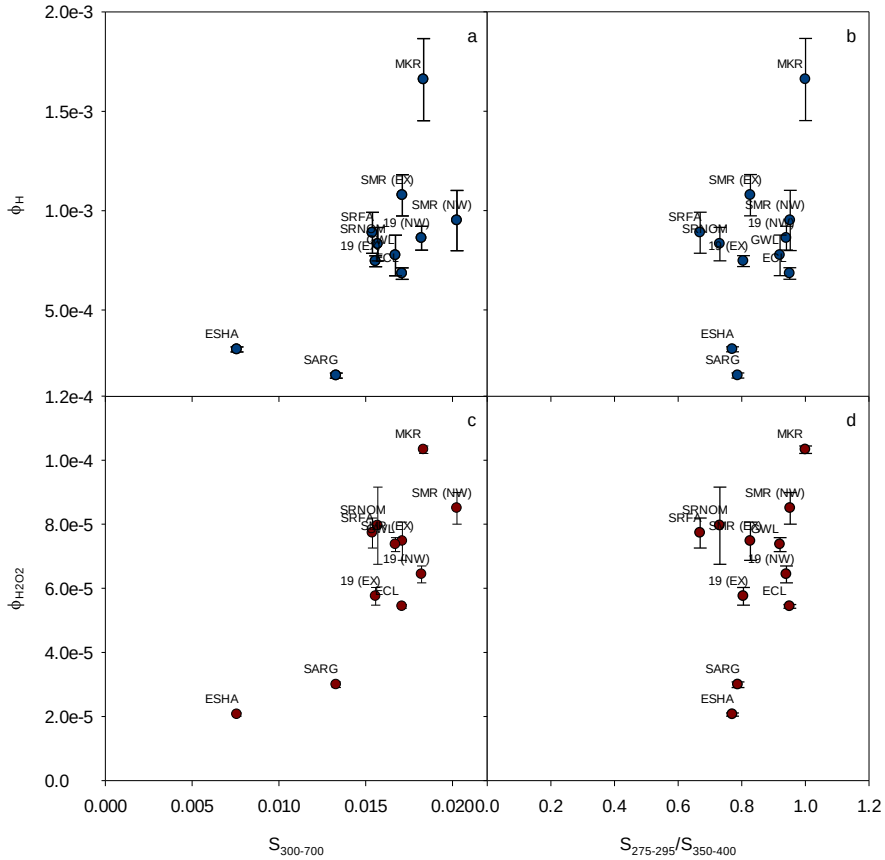

Figure 3.4. Relationships between optical properties and apparent quantum yields: (a) Φ_H vs. S300-700 (b) Φ_H vs. $S_{275-295}/S_{350-400}$ (c) Φ_{H2O2} vs. $S_{300-700}$ and (d) Φ_{H2O2} vs. $S_{275-295}/S_{350-400}$ for all samples given in Table 3.2. Error bars represent propagation of standard deviations of the Φ measurements.

3.4.4 Investigating Possible Matrix Effects

Petasne and Zika calculated that the rate constant for dismutation of $O_2^{\bullet-}$ would decrease in seawater compared to pure water since cations found in seawater stabilize $O_2^{\bullet-}$, increasing its lifetime and therefore decreasing R_{H2O2}.[7,242,243] Sodium chloride did not affect either R_H or R_{H2O2}, but the presence of the sea salt seems to have slightly enhanced R_{H2O2} while possibly decreasing R_H, although the R_H measurements are within error of one another (**Table 3.3**). The increase in R_{H2O2} is the opposite of the work by Petasne and Zika although it is not a substantial increase.[7]

Table 3.3. Effect of Salinity and Addition of DTPA on R_H and R_{H2O2} in St. 19 EX and NW

Sample	Condition	R_H (nM/s)	R_{H2O2} (nM/s)	R_H/R_{H2O2}
St. 19 (EX)	None	8.7 ± 0.3	0.67 ± 0.03	13.0 ± 0.8
	18 ppt NaCl	6.7 ± 0.8	0.77 ± 0.03	9 ± 1
	28 ppt NaCl	8 ± 1	0.71 ± 0.05	11 ± 2
	18 ppt sea salt	7 ± 1	0.73 ± 0.09	9 ± 2
	28 ppt sea salt	6.7 ± 0.6	0.80 ± 0.01	8.4 ± 0.7
	50 μM DTPA	8.8 ± 0.5	0.93 ± 0.03	9.3 ± 0.7
St. 19 (NW)	None	5.3 ± 0.4	0.39 ± 0.02	13 ± 1
	50 μM DTPA	5.5 ± 0.3	0.51 ± 0.02	10.6 ± 0.7

Uncertainties in the rates represent the standard deviation of triplicate measurements. Uncertainties were propagated for derived values.

Transition metals such as copper and iron are both commonly found in natural waters, typically in nanomolar concentrations.[244,245] Several works have demonstrated that copper and iron can catalyze the dismutation of $O_2^{\bullet-}$ with fairly high rate constants (10^7 - 10^9 $M^{-1}s^{-1}$), which would increase R_{H2O2}.[113,126,246] Alternatively, it has been shown that iron and copper can remove H_2O_2 through the Fenton reaction; iron is primarily oxidized by H_2O_2 while copper can be oxidized and reduced by H_2O_2, leading to a catalytic cycle for loss of H_2O_2.[122,123,125,127] Additionally, $O_2^{\bullet-}$ has also been shown to reduce iron.[247–249] These would all decrease the observed R_{H2O2}. Metal chelators such as DTPA can chelate multiple metals including iron, copper, and manganese and make them unable to react.[250] DTPA itself, with or without complexed metals, has been shown to be unreactive or minimally reactive with $O_2^{\bullet-}$ due to its strong binding constants with metals.[251] The addition of 50 μM DTPA to both St. 19 EX and NW had no impact on R_H and slightly increased R_{H2O2} for both samples (**Table 3.3**). The slightly increased values for R_{H2O2} results in lower ratios of R_H/R_{H2O2} but the values are still much larger than two. Therefore, the increase in R_{H2O2} in the presence of DTPA indicates that metals could

be acting as a sink for $O_2^{\bullet-}$, or even H_2O_2, but it is not significant enough to account for the high R_H/R_{H2O2} values. It is interesting that DTPA had the same effect on both the NW and the EX. Due to the process of extraction, it is not expected that both the NW and the EX would contain the same concentrations of metals. However, it has also been shown that metals that are strongly complexed with DOM can be retained during solid phase extraction.[252,253] Another chelator, desferrioxamine (DFOA), was also tested but due to its reaction with fluorescamine, was not explored further (**Figure A3.9**).

3.5 Conclusion

R_H, R_{O2}•-, and R_{H2O2} were measured on identical samples and under identical experimental conditions for the first time. All three rates displayed the same wavelength dependence, supporting a common origin for their formation. R_H/R_{H2O2} was measured for a large variety of samples and the yields were positively correlated with lower molecular weight species of CDOM based on optical properties of CDOM. Matrix effects in NW samples such as salinity and presence of metals have only a slight impact on measured values.

The large values obtained for R_H/R_{H2O2} and for R_{O2}•-/R_{H2O2} imply a significant oxidative sink for $O_2^{\bullet-}$ and verify that $O_2^{\bullet-}$ formation rates cannot be estimated simply by doubling those of H_2O_2. It has been proposed the $O_2^{\bullet-}$ could be lost to a light-dependent sink within DOM which could be a possible pathway for DOM photodegradation. The presence of an additional $O_2^{\bullet-}$ sink that is light-dependent and the possibility of its involvement in the modification of DOM are addressed in more detail in the next chapters.

Chapter 4: Investigating the Presence of a Light-Dependent Sink for Superoxide

The majority of this chapter has been submitted for publication.

Le Roux, D. M.; Powers, L. C.; Blough, N. V. "Direct Evidence of a Light-dependent Sink of Superoxide within Chromophoric Dissolved Organic Matter." (Submitted for publication).

I performed all experiments and data analysis and prepared the first draft of the manuscript. Dr. Powers and Dr. Blough assisted in data analysis and editing the manuscript.

4.1 Abstract

Superoxide ($O_2^{\bullet-}$) is produced photochemically in natural waters by chromophoric dissolved organic matter (CDOM) via the reaction of molecular oxygen with photoproduced one-electron reductants (OER) within CDOM. In the absence of other sinks (metals or organic radicals), $O_2^{\bullet-}$ is believed to primarily undergo dismutation to produce hydrogen peroxide (H_2O_2). However, past studies have implicated the presence of an additional light-dependent sink of $O_2^{\bullet-}$ that does not lead to H_2O_2 production. Direct evidence for a light-dependent sink of $O_2^{\bullet-}$ within CDOM is presented herein through $O_2^{\bullet-}$ spiking experiments. During irradiations, spikes of $O_2^{\bullet-}$ decay much faster than spikes introduced in the dark.

4.2 Introduction

Possible decay pathways for $O_2^{\bullet-}$ in natural waters involve reactions with metals[113,128,246,248,249], DOM itself[254,255], organic radicals[151,152,256], and dismutation to form hydrogen peroxide (H_2O_2).[81] H_2O_2, as a product of $O_2^{\bullet-}$ dismutation, has been employed as a proxy for $O_2^{\bullet-}$ production due to its greater stability and ease of measurement.[6,7,87] The assumption made is that $O_2^{\bullet-}$ production is double the H_2O_2 production, based on the stoichiometry of dismutation. However, using the enzyme superoxide dismutase (SOD), to catalyze the dismutation of $O_2^{\bullet-}$ to H_2O_2, a discrepancy between the rates of $O_2^{\bullet-}$ and H_2O_2

production has been noted. The presence of SOD caused the rates of H_2O_2 production to increase, suggesting that a significant portion of $O_2^{\bullet-}$ produced did not undergo dismutation to form H_2O_2.[6,7,77,87]

Despite difficulty in the method of measurement, direct measurements of $O_2^{\bullet-}$ production have been made and compared to H_2O_2 measurements. Currently, the most widely used method for $O_2^{\bullet-}$ is based on a chemiluminescent reaction employing flow injection analysis that allows for continuous measurement of $O_2^{\bullet-}$.[231] During an irradiation, the establishment of steady-state can be observed, while the dark decay can be monitored following the removal of light.[77,95,238] The production rate can then be calculated from the steady-state concentration and dark decay rate constant, assuming that the dark decay rate reflects the total decay rate. The stoichiometry of the reaction for dismutation should result in a ratio of $O_2^{\bullet-}$:H_2O_2 rates equal to 2. However, values of 2.2-9.8 have been obtained for various natural waters suggesting that an oxidative reaction is competing with dismutation.[257]

Alternatively, some studies have directly measured the initial production rate and compared this to the calculated production rate obtained from the dark decay and steady-state concentration.[257–259] Powers et al.[257] found that the modeled rates were similar to the measured initial rates for samples from the Gulf of Alaska. Shaked et al.[258] also claimed to have obtained similar results for the Gulf of Aqaba but their measured initial rates are slightly higher than the range of their modeled rates. Ma et al.[259] found that the measured initial rates were 2-5 times higher compared to the modeled rates for a variety of reference materials and wastewater effluents. Issues with quantifying initial rates have been raised and include the unavoidable loss of $O_2^{\bullet-}$ during the transit time from the sample to the detector, which Ma et al. attempted to account for by using a correction procedure.[257–259] An additional issue is that the choice of the

time range over which the initial rate is measured can heavily influence the values.[257,258] Regardless, the fact that measured rates have been observed to be larger than calculated rates suggests that a kinetic model using only the dark decay rate constant leads to an underestimation of the production rates, implying the presence of an additional light-dependent decay pathway for $O_2^{\bullet-}$.

Since $O_2^{\bullet-}$ is rather difficult to measure experimentally, recent work has studied the production rates of the OER, the proposed precursor to $O_2^{\bullet-}$.[78,80,260] OER production has recently been compared to $O_2^{\bullet-}$ production with rates similar in magnitude, suggesting that the measurement of OER may currently be the best proxy for $O_2^{\bullet-}$.[260] OER measurements have therefore been compared to H_2O_2 production. Theoretically, a value of 2 should also be obtained here, but values from 5 to 16 have been observed in reference materials, exudates, natural waters, and C-18 extracts, again suggesting the presence of an additional pathway for $O_2^{\bullet-}$ loss.[80,260]

The culmination of these results suggests that there is an additional light-dependent oxidative sink for $O_2^{\bullet-}$ that does not lead to H_2O_2 production. Therefore, current decay models used for $O_2^{\bullet-}$ do not accurately reflect the magnitude of the total decay. This leads to an underestimation of $O_2^{\bullet-}$ production as determined from steady-state concentration and dark decay data. It has been suggested that a light-dependent sink exists that is associated with CDOM, but very little work has been done to investigate this possibility. Work reported by Ma et al. attempted to determine the light-dependent decay rate constant.[259] The initial production rate of $O_2^{\bullet-}$ was divided by the steady-state concentration to calculate a total first-order decay rate constant. This rate constant represents a combination of the light-dependent decay, decay due to dismutation, and other possible pseudo-first order decay pathways. The light-dependent decay rate constant was then determined by subtracting the rate constants for dismutation and the dark

pseudo-first order decay. The light-dependent decay rate constants were found to be in the range of 0.1-0.4 s^{-1}, which constituted between 63-81% of the overall decay constant.[259] However, direct evidence for the presence of this sink does not yet exist.

In this chapter, the existence of an oxidative light-dependent sink was demonstrated through spiking experiments. When a sample has reached steady-state during an irradiation, the sample is spiked with an aliquot of $O_2^{\bullet-}$, and the decay of the spike is monitored. For comparison, the sample is also spiked during the decay phase, when the sample was removed from light. This work demonstrates that $O_2^{\bullet-}$ is consumed rapidly when the light is on, as compared to the much slower decay that occurs when the light is off. Significant quantitative work and modeling of the data has been conducted to directly determine the light-dependent rate constant. These values can be used to modify existing decay models to provide better estimations of $O_2^{\bullet-}$ production rates.

4.3 Materials and Methods

4.3.1 Materials

Boric acid, sodium acetate, hydrochloric acid (HCl), sodium hydroxide (NaOH), and superoxide dismutase (SOD; from bovine erythrocytes) were purchased from Millipore Sigma. Acetone and ethanol were purchased from Fisher Scientific. All reagents and chemicals were ACS grade. 2-methyl-6-(4-methoxyphenyl)-3,7-dihydroimidazo[1,2-a]pyrazin-3(7H)-one) (methyl Cypridina luciferin analogue or MCLA) was purchased from TCI Chemicals. Diethylenetriaminepentaacetic acid (DTPA) was purchased from Fluka. Suwannee River fulvic acid (SRFA; 3S101F) was purchased from the International Humic Substance Society. Purified water (18 MΩcm) was obtained from a Sartorius Arium Mini purification system.

4.3.2 Sample Preparation

Stock solutions of SRFA were prepared by diluting/dissolving the SRFA in ultrapure water. These stocks were adjusted to pH 7 using NaOH and HCl and filtered using pre-rinsed 0.2 μM nylon filters. Dilutions of these stocks at desired concentrations for experiments were then prepared by diluting the stock solutions with 50 mM borate buffer at a pH of 8.

4.3.3 Measurement of Superoxide

$O_2^{\bullet-}$ was measured and standardized as described in section 3.3.5 with some modifications. The photomultiplier tube voltage was reduced to 1000 V. Photoproduction measurements for $O_2^{\bullet-}$ were conducted in a 5 cm pathlength quartz cylindrical cell (15 mL total volume). Irradiations were conducted with the set-up as described in section 2.3.3. The sample was monitored to acquire the time course of $O_2^{\bullet-}$ production and the establishment of steady-state, with the cell then removed from the light to monitor the decay. For spiking experiments, a $O_2^{\bullet-}$ stock was generated as described above and the sample was spiked with appropriate volumes of $O_2^{\bullet-}$ (low μL range) during the steady-state phase or during the decay phase. The sample was continuously stirred using a stir bar and plate. Integration of the data was performed in Excel. Model fits were conducted in MatLab® using the Curve Fitting application.

4.4 Results and Discussion

4.4.1 Wavelength Dependence of Superoxide Data

Upon irradiation of SRFA, $O_2^{\bullet-}$ concentration rises rapidly and approaches steady-state within approximately 1-2 minutes, depending upon the wavelength of the cut-off filter used. As the wavelength of the cut-off filter is increased, the rates of $O_2^{\bullet-}$ production and the steady-state concentrations decreased (**Figure 4.1**). Initial $O_2^{\bullet-}$ production rates were determined based on

~15 seconds of data following the delay time (delay from initiation of irradiation to detection) with no correction for any losses during transit from the irradiation cell. Steady-state concentrations were calculated from the average of ~10 points of the plateau near the time the sample was removed from the light with no correction for losses due to the delay time. Upon removing the sample from the light, the decay of $O_2^{\bullet-}$ is observed. Very little exists in the literature about the wavelength dependence of $O_2^{\bullet-}$ kinetic data, although several studies have estimated it based on H_2O_2 data.[87,238] From **Figure 4.1**, it is evident that the production rate and steady-state concentration decrease with increasing wavelength of the cut-off filter which is in agreement with a limited number of direct studies on $O_2^{\bullet-}$.[259,260]

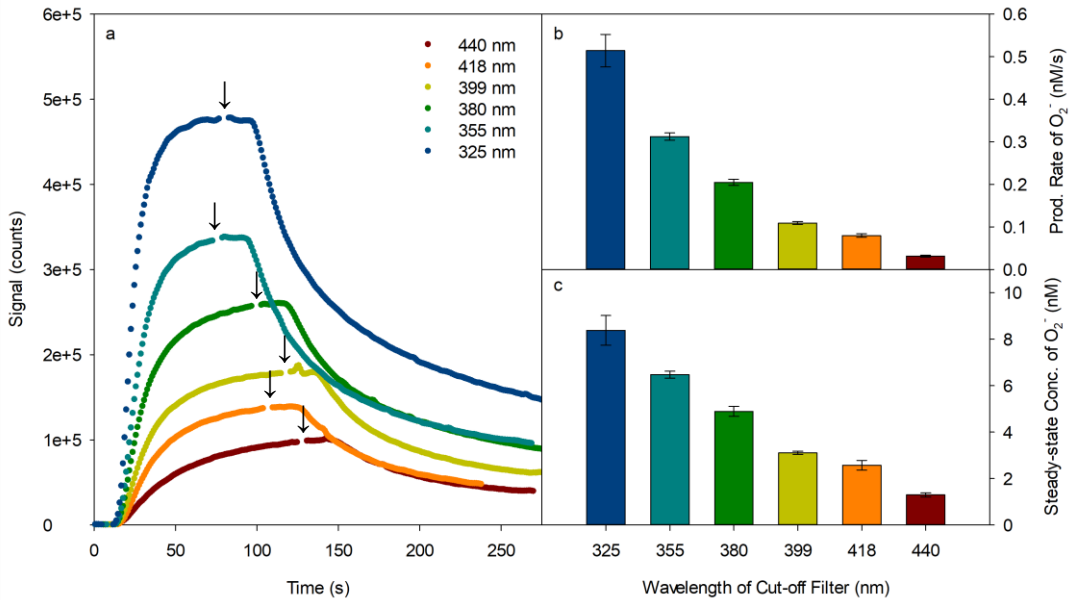

Figure 4.1. Signals for $O_2^{\bullet-}$ production, establishment of steady-state, and decay using a variety of different wavelength cut-off filters (a). t = 0 is when the sample began being irradiated. Down arrows indicate removal of sample from light. Production rates (b) and steady-state concentrations (c) were calculated from standard curves. Error bars are standard deviation for three trials.

4.4.2 Enhanced Decay of Superoxide During Irradiation

Spiking experiments were conducted by introducing known amounts of $O_2^{\bullet-}$ into SRFA during irradiation or during the decay phase (post-irradiation) (**Figure 4.2**). Standard spikes of

$O_2^{\bullet-}$ into SRFA in the dark are also shown for comparison, with the concentrations of the spikes approximately matched. The rate of decay of the standard spikes in the presence of SRFA are faster than the decay rates observed in buffer alone and in solutions containing diethylenetriaminepentaacetic acid (DTPA) (**Text A4.1**). These results indicate that SRFA is involved in $O_2^{\bullet-}$ dark decay, though how much of a contribution is due to complexed metals within SRFA is unknown (**Text A4.1**). Even still, the rates of decay of the steady-state spikes are significantly larger than those of the standards. The rates of decay of the steady-state spikes also appear to be much larger than post-irradiation decay (after removal of the sample from light) and also larger than those of the decay spikes (**Figure 4.2**).

The magnitude of the response between the standard spikes and the steady-state spikes, shows that there is a reduction in amplitude of the steady-state spikes, as well as a more rapid decay of the remaining $O_2^{\bullet-}$. This behavior provides evidence that a significant fraction of the $O_2^{\bullet-}$ spike is consumed at a rate that cannot be resolved within the timescale of these measurements. This has implications on the determination of the rate constants obtained in the following sections. Since a faster decay exists but cannot be observed under our conditions, the rate constants obtained below are lower bound estimates. Comparing the steady-state spikes under the 325 nm and the 440 nm cut-off filters, more of the spike is consumed under the 325 nm filter, indicating that the photoproduction of the sink is wavelength dependent. Comparison of the magnitude of the spikes introduced during the decay phase show that they are not consumed as readily as during irradiation, although some loss still appears to occur. The rate of decay of the decay spikes is slower than that of the steady-state spikes.

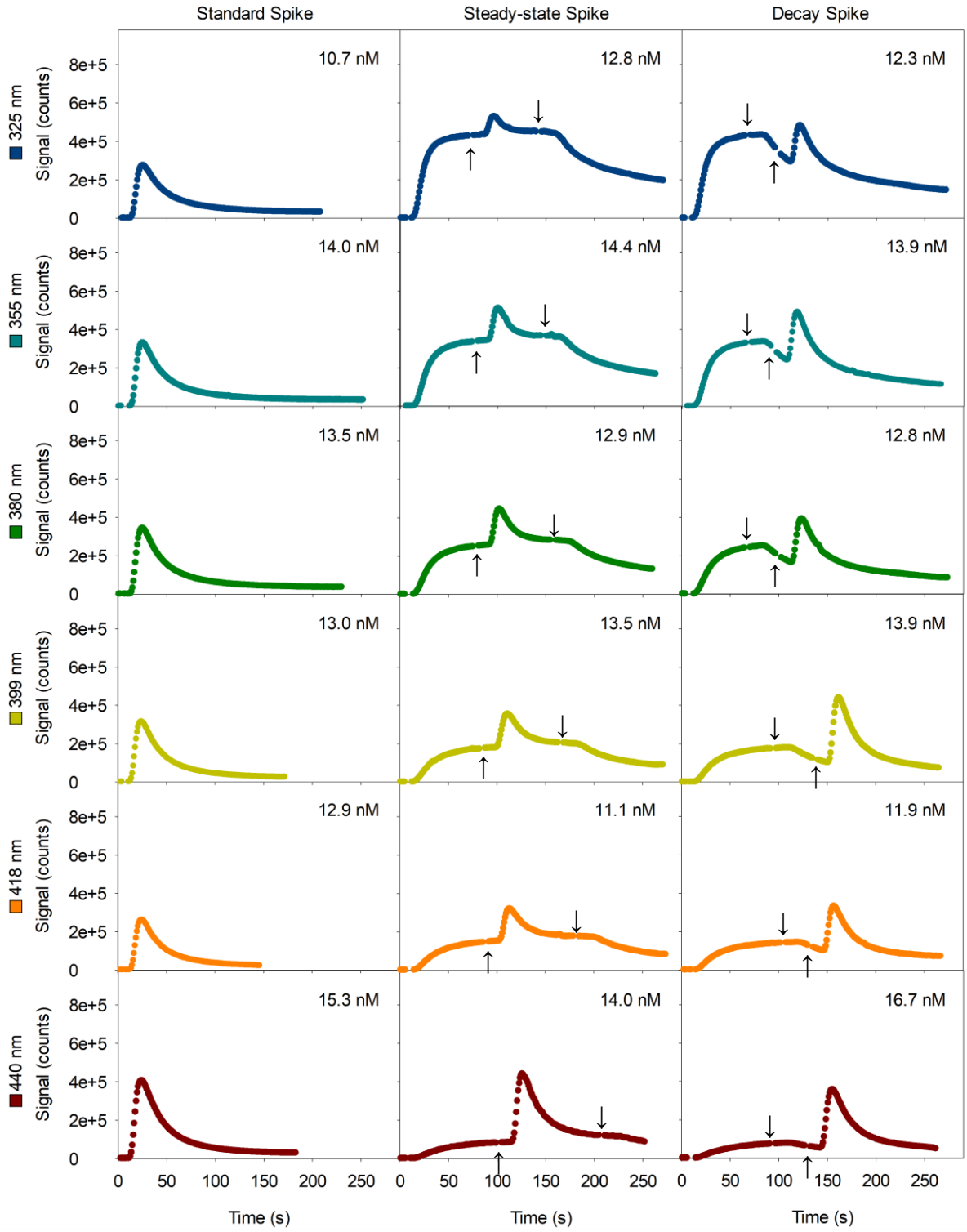

Figure 4.2. Signals for $O_2^{\bullet-}$ spikes: first column are standards, second column are steady-state spikes, and third column are decay spikes. Colors indicate the wavelength cut-off filter used. t = 0 is when the sample began being irradiated. Up-facing arrows indicate time of the spike and down-facing arrows indicate time that the sample was removed from light.

4.4.3 Curve Fitting of Decay Data to Determine Kinetics

First-order (Eqn. 4.1) and second-order fits (Eqn. 4.2) were applied to the $O_2^{\bullet-}$ decay data where $[O_2^{\bullet-}]$ is the $O_2^{\bullet-}$ concentration from the decay trace data, $[O_2^{\bullet-}]_i$ is the initial $O_2^{\bullet-}$ concentration at t=0, k is the decay rate constant, t is the time in seconds, $[O_2^{\bullet-}]_t$ is the $O_2^{\bullet-}$ concentration out at long timescales. In MatLab®, a, b, and c were used to symbolize $[O_2^{\bullet-}]_i$, k, and $[O_2^{\bullet-}]_t$ respectively, for simplicity. Fits were applied to decay of the standards, post-irradiation decay (PID), steady-state spike decay (SSD), the decay in the dark post-steady-state spike (PSD), and to the decay of the decay phase spikes (DSD) (**Figure 4.3**). Decisions based on whether the decay was first or second-order were determined based on correlation between spike concentration and intercept value (a), general alignment of fit to data (R^2 value), as well as reasonable fit to the signal offset at long timescales (c).

$$\ln([O_2^{\bullet-}]_t) = \ln([O_2^{\bullet-}]_i) + kt \qquad \text{(Eqn. 4.1)}$$

$$\frac{1}{[O_2^{\bullet-}]_t} = \frac{1}{kt} + \frac{1}{[O_2^{\bullet-}]_i} \qquad \text{(Eqn. 4.2)}$$

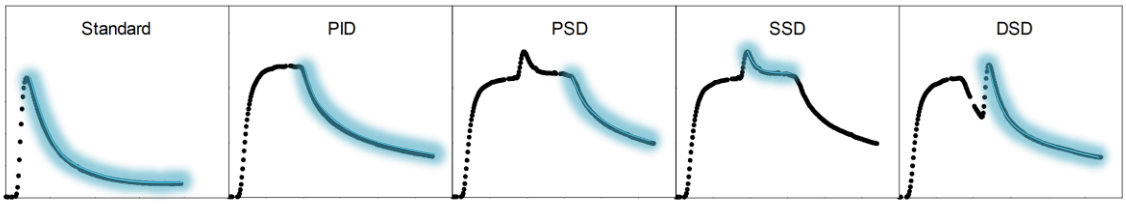

Figure 4.3. Visual representation of modeled decays of $O_2^{\bullet-}$.

The presence of a noticeable offset in the data out at long timescales indicates the continued presence of $O_2^{\bullet-}$ (**Figure 4.2**). Others have also noted the presence of $O_2^{\bullet-}$ at long timescales and the use of the enzyme superoxide dismutase (SOD), which catalyzes the dismutation of $O_2^{\bullet-}$ into H_2O_2, has resulted in the loss of this signal.[88,257] However, it has been observed that SOD interferes with chemiluminescence of MCLA, as well as other analogs, and

therefore the contribution of the loss of signal due to the loss of $O_2^{\bullet-}$ or due to the interference is indistinguishable.[261,262] In the tests with SOD, an apparent plateau of signal loss with SOD concentration was reached, approximately down to baseline, indicating that at least some of the signal loss was due to the presence of $O_2^{\bullet-}$ (**Figure A4.3** and **A4.4**). Therefore, a constant was included in the fit as a variable in all of the first and second-order fits. The value of the constant decreased with increasing wavelength of the cut-off filter (**Figure A4.5**).

Traditionally, $O_2^{\bullet-}$ decay traces have been modeled considering the self-dismutation reaction and a pseudo-first order sink that is meant to combine other decay pathways (**Text A4.2**).[77,126,254,257,259,263] In the analysis done here, standard spikes of $O_2^{\bullet-}$ in SRFA in the dark fit to first-order kinetics (**Figure 4.4**). The decay rate constants obtained from the first-order fitting for standard spikes in the dark (0.037 ± 0.002 s^{-1}; **Figure 4.5**) are generally higher than other studies that have used the traditional modeling method on natural water samples from coastal waters off Georgia (0.013 s^{-1})[238], from the Gulf of Alaska (0.002-0.016 s^{-1})[111] and (0.015-0.035 s^{-1})[257], from the Eastern Pacific Ocean (0.0189-0.0276 s^{-1})[95], from the Southern Ocean (0.004-0.074 s^{-1})[126], and from the Atlantic Ocean (0.009-0.034 s^{-1})[263]. In terms of reference materials, the values fall in line with work by Ma et al. (0.0087-0.038 s^{-1})[259] but are higher than what was observed by Garg et al. (0.0066 s^{-1}).[77]

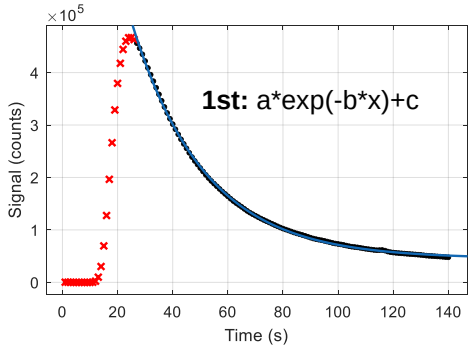

Figure 4.4. Signal for $O_2^{\bullet-}$ decay for standard spike. t = 0 is when 1 mg/L SRFA was spiked with 18.7 nM $O_2^{\bullet-}$.

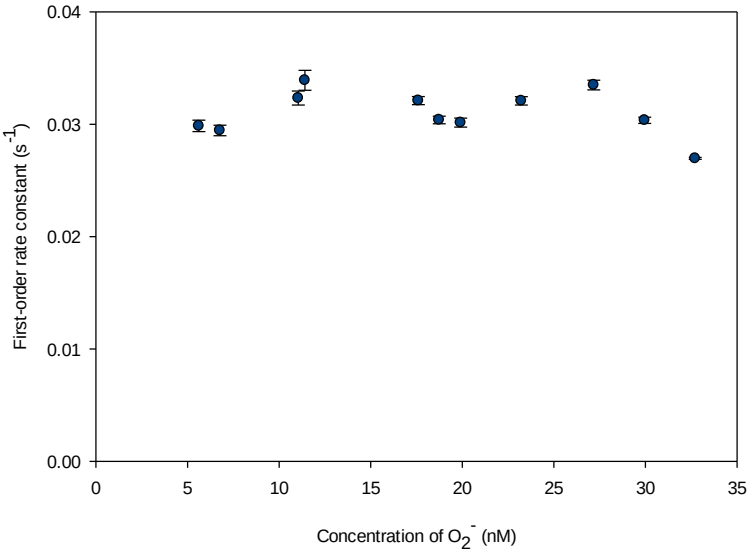

Figure 4.5. Comparison of first-order rate constant values obtained from a variety of standard $O_2^{\bullet-}$ concentrations spiked into 1 mg/L SRFA in the dark. Error bars are from the error in the fit.

Decay kinetics for $O_2^{\bullet-}$ spiked into samples in the dark has been attributed to $O_2^{\bullet-}$ reacting with quinone functionalities within CDOM.[263] Heller and Croot modeled $O_2^{\bullet-}$ reactions with quinones and found that pseudo-first order kinetics would fit decay curves up to around a minute but then the contribution of $O_2^{\bullet-}$ production from reaction of molecular oxygen with semiquinones could start to interfere with the decay curve, causing a divergence from pseudo-first order kinetics.[263] Divergences could also be attributed to the presence of two different reactive pools within CDOM, one of which being significantly more reactive to $O_2^{\bullet-}$ than the other.[263]

The first-order rate constants were determined for all of the 325 nm PID data (0.02095 ± 0.00005 s^{-1}; **Table A4.1**) for comparison to the standard dark decay data. The PID first-order rate constants are ~1.7 times smaller than the first-order rate constants determined for the standard dark decay. The phenomenon of the decay of $O_2^{\bullet-}$ standards being faster than the decay post-irradiation has been previously observed.[88,111,257] However, this is highly dependent upon the method used to fit the data because it has been found that there is no difference between post-

irradiation decay and standard decay.[77] For instances where the decay was observed to be faster in the standards as compared to post-irradiation, it has been suggested that either there was something in the standard $O_2^{\bullet-}$ solution that would cause a faster decay or that differences in temperature of the sample affected the kinetics.[111] Another possibility that was brought up is that there are different decay pathway distributions depending upon the initial $O_2^{\bullet-}$ concentration.[88] However, it has also been found that the rate constant does not change with initial $O_2^{\bullet-}$ concentration which was also observed here (**Figure 4.5**).[254] Another alternative as discussed by Garg et al. is the possibility that the dark decay pathway is somehow deactivated during irradiation.[77] Although first-order kinetics were analyzed here for PID, second-order fit best (see below). Based on the fact that the standard decay in the dark and PID required fits to different kinetics, this later possibility of a deactivated pathway is supported.

For PID and PSD, a second-order decay equation fit the decay traces well while a first-order decay did not (**Figure 4.6**). The fact that both PID and PSD data fit to second-order kinetics and have similar rate constants indicates that the steady-state $O_2^{\bullet-}$ spikes were totally consumed and did not impact the post-spike dark decay (**Figure 4.7**). SSD data fit to first-order kinetics with the steady-state concentration as the offset (or even with moving the SSD trace down to baseline from subtracting the steady-state concentration) (**Figure 4.8**). DSD data are interesting because they appear to fit primarily to first-order although the second-order also sometimes fit, indicating some possible mixed order kinetics. However, the second-order fits yielded unreasonably large intercepts at time zero (time spike was injected into sample) that exceeded the calculated spike concentration (**Table A4.1**), so the first-order fits were used (**Figure 4.8**). First-order fits gave intercept values that were in better agreement with the initial spike concentration (**Table A4.1**).

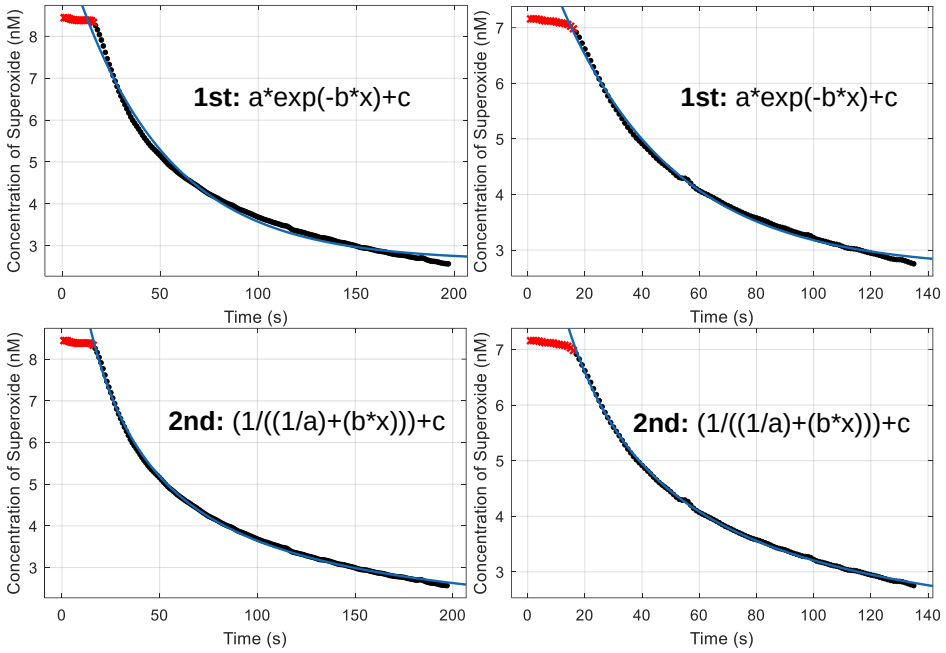

Figure 4.6. Signals for $O_2^{\bullet-}$ decay for PID (left) and PSD (right) fit to first-order (top) and second-order (bottom) fits. t = 0 is when the sample was removed from the light. Black dots are the recorded data, the blue line is the model fit, and red x's are excluded points. Second-order fits both PID and PSD the best.

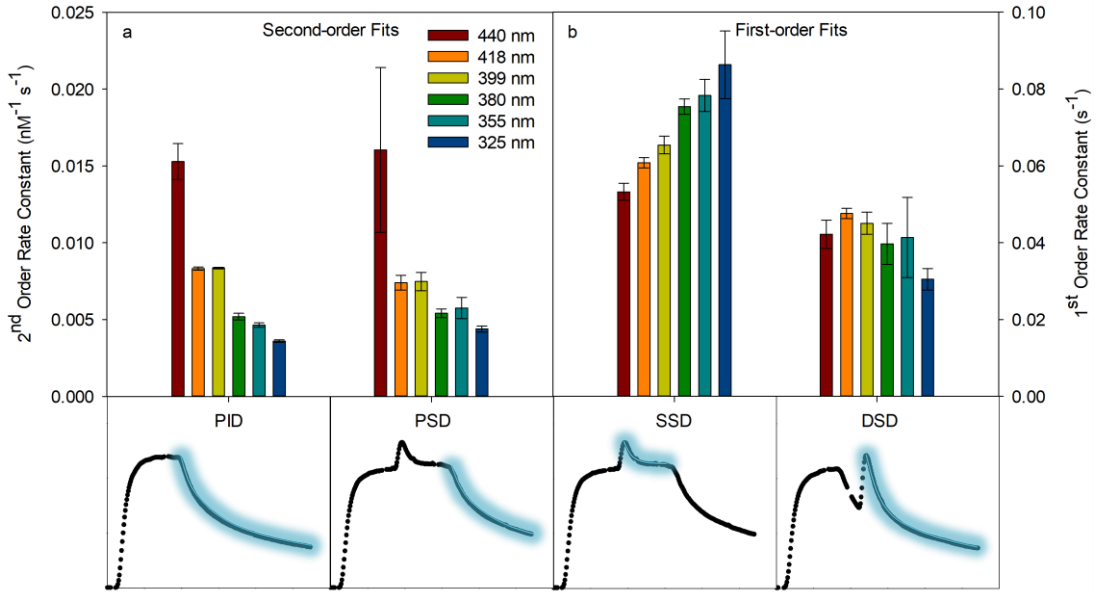

Figure 4.7. Second-order fits to PID and PSD (a) and first-order fits to SSD and DSD (b) for all wavelength cut-off filters. Bottom panel shows a visual for the data that was fit for each category. Error bars are standard deviations for fits to at least three trials.

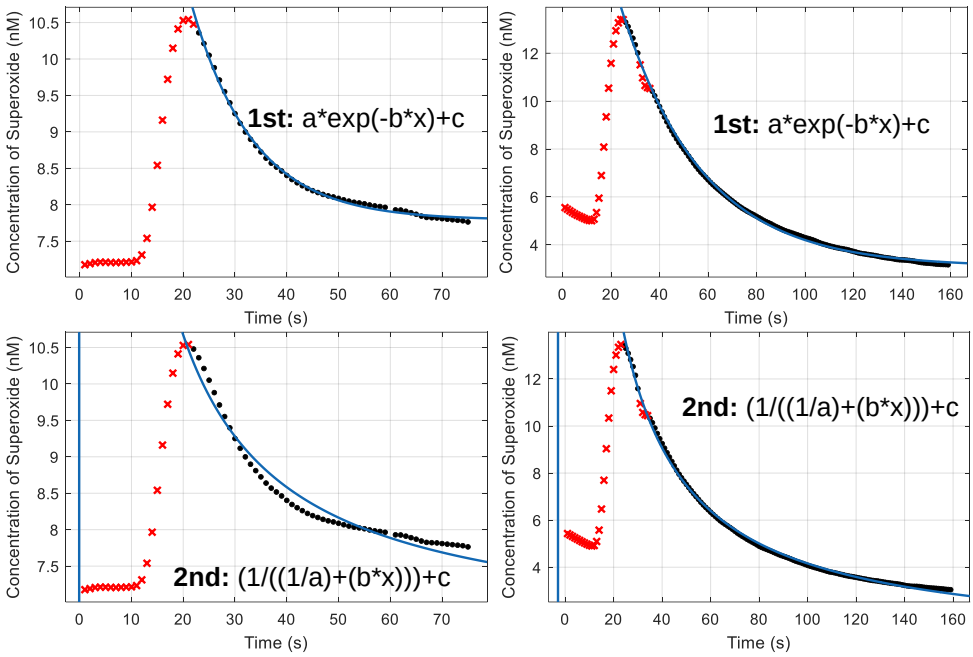

Figure 4.8. Signals for $O_2^{\bullet-}$ decay for SSD (left) and DSD (right) fit to first-order (top) and second-order (bottom) fits. t = 0 is when the sample was spiked with $O_2^{\bullet-}$. Black dots are the recorded data, the blue line is the model fit, and red x's are excluded points. First-order fits both the SSD and DSD the best.

Even though both the standard decay and the SSD fit to first-order kinetics, the magnitude of the rate constants of SSD (0.053 ± 0.002 to 0.086 ± 0.009 s^{-1} for 440 nm to 325 nm respectively) are still significantly larger than that of the standard spikes (0.037 ± 0.003 s^{-1}), indicating faster reaction during irradiation. There is also the possibility that since only the later end of the SSD can be resolved, that there exists a faster decay portion of these decay curves that is unable to be captured due to the delay time of the instrument set-up, which would lower the observed rate constant. Only one other work has attempted to quantify the rate constant for reaction between $O_2^{\bullet-}$ and the light-dependent sink (**Text A4.2**). Interestingly, their values obtained for reference fulvic acids (1S101F and 2S101F) are ~0.12 s^{-1} and the value obtained for 3S101F in this work is about ~0.089 s^{-1}.[259] The difference in value could be due to differences in irradiation conditions. Their experiments were conducted with a 290 nm cut-off filter whereas a 325 nm cut-off filter was used here and considering the evident wavelength dependence of the

rate constant (**Figure 4.7**), it is not surprising that theirs is larger.

Rate constants obtained from SSD data are greater than those of the DSD, with larger discrepancies between the two occurring with shorter wavelength cut-off filters (**Figure 4.7**). These numerical results fall in line with what is observed visually, where shorter wave-length cut-off filters appear to result in greater loss of the $O_2^{\bullet-}$ spike for both the steady-state and decay spikes (**Figure 4.2**). Additionally, the intercept values for SSD are lower than the calculated concentration of the spike injected (**Table A4.1, A4.2**), which further supports the earlier statement that a significant portion of the spike is lost before the decay can be resolved. The loss is more significant for shorter wavelength cut-off filters. This initial loss is also still present in the decay spikes but is not as large (**Table A4.1**).

4.5 Conclusion

The presence of a light-dependent oxidative sink of $O_2^{\bullet-}$ within CDOM was explicitly demonstrated through $O_2^{\bullet-}$ spiking experiments. The first-order rate constants for the light-dependent decay are 40-70% larger than those of the standard spikes conducted in the dark and the light-dependent decay has a wavelength dependence. The rate constants obtained here are a lower estimate due to the limitations of the experimental set-up to capture the decay and it is likely that an initial faster decay exists that was unable to be resolved. The next chapter will analyze the decay data using integration in order to give a fuller understanding of the magnitude of this light-dependent sink and will investigate possibilities for the identity of the sink.

Chapter 5: Possibilities for the Identity of the Light-Dependent Sink

The majority of this chapter has been submitted for publication.

Le Roux, D. M.; Powers, L. C.; Blough, N. V. "Direct Evidence of a Light-dependent Sink of Superoxide within Chromophoric Dissolved Organic Matter." (Submitted for publication).

I performed all experiments and data analysis and prepared the first draft of the manuscript. Dr. Powers and Dr. Blough assisted in data analysis and editing the manuscript.

5.1 Abstract

In the absence of other sinks (metals or organic radicals), $O_2^{\bullet-}$ is believed to undergo primarily dismutation to produce hydrogen peroxide (H_2O_2). However, past studies have implicated the presence of an additional light-dependent sink of $O_2^{\bullet-}$ that does not lead to H_2O_2 production. The previous chapter provided direct evidence for a light-dependent sink of $O_2^{\bullet-}$ through $O_2^{\bullet-}$ spiking experiments. During irradiations, spikes of $O_2^{\bullet-}$ decay much faster than spikes introduced in the dark. H_2O_2 production was tested for by observing the H_2O_2 concentration post $O_2^{\bullet-}$ spike. At low $O_2^{\bullet-}$ spike concentrations, the light-dependent sink does not produce H_2O_2. This work demonstrates that estimating $O_2^{\bullet-}$ production as twice the H_2O_2 production is not as accurate as once believed. Comparing the absorbance and fluorescence of a sample pre- and post-spike indicates possible degradation of CDOM induced by $O_2^{\bullet-}$.

5.2 Introduction

Possibilities for the light-dependent sink for $O_2^{\bullet-}$ within DOM have been previously proposed. It has been proposed that the moieties that could be involved in the one-electron transfer within CDOM are phenols as the donors and quinones as the acceptors.[80,260] If this is the case, then the one-electron transfer would result in the formation of a phenoxy radical. Phenoxy radicals have been shown to have very large rate constants with $O_2^{\bullet-}$, near the diffusion-

controlled limit.[264] Reaction between phenoxy radicals and $O_2^{\bullet-}$ can have several different results depending upon the structure of the phenoxy radical: back reaction to re-form the phenol and molecular oxygen or addition of the $O_2^{\bullet-}$ to the phenol ring to form hydroperoxides, though several studies have demonstrated that the addition reaction is predominant.[265–268] From here, it has been shown that further reaction occurs that leads to ring-opened products.[265,267,268] If this is the case, this could be a possible explanation for how CDOM gets photochemically oxidized/transformed as it is transported from terrestrial sources to the open ocean. More recent studies on phenol transformation (tyrosine, acetaminophen, and 2,4,6-trimethylphenol), in the presence of humic substances, also found that the structure of the phenol dictated its transformation pathways.[151,152] Additionally, the rate of transformation of tyrosine varied among the humic substances tested[152], indicating the importance of the chemical structure of CDOM in this process. Interestingly, the photodegradation of the humic substance was inhibited in the presence of acetaminophen.[151] This result suggests that reaction between $O_2^{\bullet-}$ and external phenoxy radicals to induce their transformation could be interfering with the pathway of $O_2^{\bullet-}$ reacting with phenoxy radicals within DOM to induce its degradation.

Although phenolic groups and quinones are large components of the antioxidant/free-radical scavenging capabilities of DOM[269–271], most studies that have investigated this have only looked at their activity in the dark. Irradiation of CDOM is likely to produce a variety of organic radicals, such as peroxyl radicals, that could also be possible sinks for $O_2^{\bullet-}$.[77]

Since the light-dependent sink of $O_2^{\bullet-}$ has been suggested to be oxidative and therefore not produce H_2O_2, this theory was tested for by monitoring H_2O_2 production after the introduction of the $O_2^{\bullet-}$ spikes. $O_2^{\bullet-}$ spikes were introduced into samples during irradiation and in the dark post-irradiation and these were then tested for H_2O_2. Control experiments were also

conducted to test for H_2O_2 production from $O_2^{\bullet-}$ spikes introduced into samples in the dark. The possibility of the sink being CDOM based and resulting in the structural degradation of CDOM was tested for by observing changes in the absorbance and fluorescence spectra of CDOM post-spike.

5.3 Materials and Methods

5.3.1 Materials

Boric acid, sodium carbonate, monobasic sodium phosphate, hydrochloric acid (HCl), sodium hydroxide (NaOH), and phosphoric acid were purchased from Millipore Sigma. All reagents and chemicals were ACS grade. 10-methyl-9-(p-formylphenyl) acridinium carboxylate trifluoromethanesulfonate (acridinium ester or AE) was purchased from Waterville Analytical Co. Hydrogen peroxide (H_2O_2) was purchased from EMD. Suwannee River fulvic acid (SRFA; 3S101F) was purchased from the International Humic Substance Society. Purified water (18 MΩcm) was obtained from a Sartorius Arium Mini purification system.

5.3.2 Sample Preparation

Stock solutions of SRFA were prepared by diluting/dissolving the SRFA in ultrapure water. These stocks were adjusted to pH 7 using NaOH and HCl and filtered using pre-rinsed 0.2 μM nylon filters. Dilutions of these stocks at desired concentrations for experiments were then prepared by diluting the stock solutions with 50 mM borate buffer at a pH of 8.

5.3.3 Additional Superoxide Data Analysis

Integration of the data obtained in Ch. 5 was performed in Excel using the trapezoid rule. For the standards, two methods were used for integration. The method one, the pre-spike

baselines were subtracted from the decay traces, but no additional subtractions/baseline corrections were conducted, and the traces were integrated. For method two, the constant off-set values that were obtained from the curve fittings were additionally subtracted from the decay traces and they were then integrated. The standard integrated areas from both methods were plotted to produce standard curves.

Steady-state spikes were subtracted out based on the steady-state concentration and then integrated. Decay spikes were first lined up with a post-irradiation decay trace. The decay spike trace and the post-irradiation trace were integrated and the final integrated area was determined by subtracting the integration below the post-irradiation decay trace from the decay spike trace (**Figure A5.1**). All of the integrated areas of the steady-state and decay spikes were converted to concentrations using both standard curves and these results were averaged. All spikes were determined by both standard curves and averaged because the decay phase spikes under longer wavelength cut-off filters appeared to be overestimated because the loss of the spike was small and there was difficulty in lining up a post-irradiation decay trace to perform the proper subtraction (**Figure A5.2**).

The concentrations obtained for the spikes based on the integration analysis are called the "apparent" concentration ($[O_2^{\bullet-}]_{app}$), due to the loss of the spike from consumption by the sink. The "actual" concentration of the spike ($[O_2^{\bullet-}]_{act}$) was determined based on the stock concentration (section 3.3.5) and subsequent dilution of the spike into the sample at the time of injection. The following equation was used to calculate the percent loss of the spike:

$$\%\ Loss = \frac{[O_2^{\bullet-}]_{act} - [O_2^{\bullet-}]_{app}}{[O_2^{\bullet-}]_{act}} * 100\% \qquad \text{(Eqn. 5.1)}$$

5.3.4 Measurement of Hydrogen Peroxide

H_2O_2 was measured as described in section 3.3.4.

5.3.5 Determination of Optical Properties

Absorbance and fluorescence measurements, and associated calculations, were conducted as described in section 3.3.6.

5.4 Results and Discussion

5.4.1 Integration of Superoxide Spike Data

Comparison of the concentration of the spike as it appeared based on integration to the concentration of $O_2^{\bullet-}$ that was actually spiked into the sample based on calculations from the stock, provides the percent loss of the spike (Equation 5.1). Steady-state spikes show a significant loss of about 90 to 40 % of the $O_2^{\bullet-}$ spike whereas decay spikes show a much lower loss of about 45 to 0 % across the wavelength range (**Figure 5.1**). The spikes show a wavelength dependence where more significant loss occurs under irradiation with a shorter wavelength cut-off filter. The losses of the decay spikes also show a similar wavelength dependence.

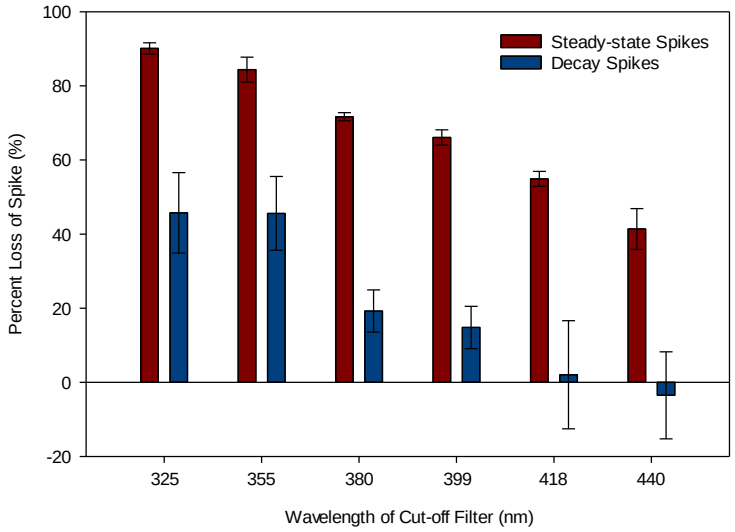

Figure 5.1. Percent loss of steady-state (red) and decay (blue) spikes for each wavelength cut-off filter. Error bars are standard deviation of at least three spikes.

Interestingly, while doing the experiments, it was observed that higher concentrations of spikes needed to be injected into samples during irradiation with the 325 nm filter as compared to the 440 nm filter in order to visibly capture the decay of the spike. In terms of concentrations, 90% of spike concentrations of up to ~45 nM are consumed during irradiation with the 325 nm filter. This drops to 45% consumption of up to ~10 nM with the 440 nm filter. When injecting similar concentrations of spikes into the samples during the decay phase, less loss occurs. For the decay spikes, 45% consumption occurs for spikes up to ~45 nM after irradiation with the 325 nm filter. This drops to no consumption for spikes up to ~10 nM after irradiation with the 440 nm filter.

5.4.2 Quantifying Hydrogen Peroxide Concentration Post-spike

$O_2^{\bullet-}$ has been shown to be primarily formed from photoproduction of reducing radicals within CDOM. The possibilities for a light-dependent sink for $O_2^{\bullet-}$ are as follows: back-reaction with the oxidized group within CDOM ($CDOM^{\bullet+}$) to re-form molecular oxygen (no net reaction),

reaction with $CDOM^{\bullet+}$ and further intermolecular reaction, potentially leading to ring-opened products, reduction to form H_2O_2, or reaction with some other oxidized moiety within CDOM to form molecular oxygen (**Figure 5.2**).

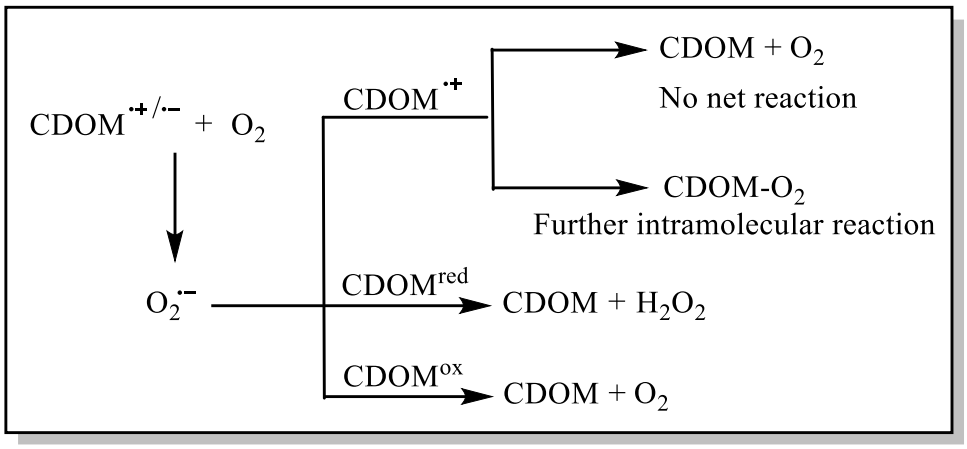

Figure 5.2. Possibilities for the light-dependent, CDOM associated, decay pathways for $O_2^{\bullet-}$.

Although the available evidence indicates that this sink does not produce H_2O_2 [7,80,87,259,260], this proposal was evaluated by measuring the H_2O_2 production after the introduction of $O_2^{\bullet-}$ spikes. H_2O_2 concentrations were analyzed following steady-state, decay, and dark $O_2^{\bullet-}$ injections. Since the detection limit was significantly higher for H_2O_2 than $O_2^{\bullet-}$, 10 mg/L SRFA was employed in place of 1 mg/L SRFA used above for the $O_2^{\bullet-}$ experiments. The stoichiometry expected for $O_2^{\bullet-}$ dismutation is 2:1.[81] However, the stoichiometry for $O_2^{\bullet-}$ spikes introduced during irradiation were much greater than 2:1 for spike concentrations ≤ 500 nM where the 2:1 ratio is observed (**Figure 5.3**).

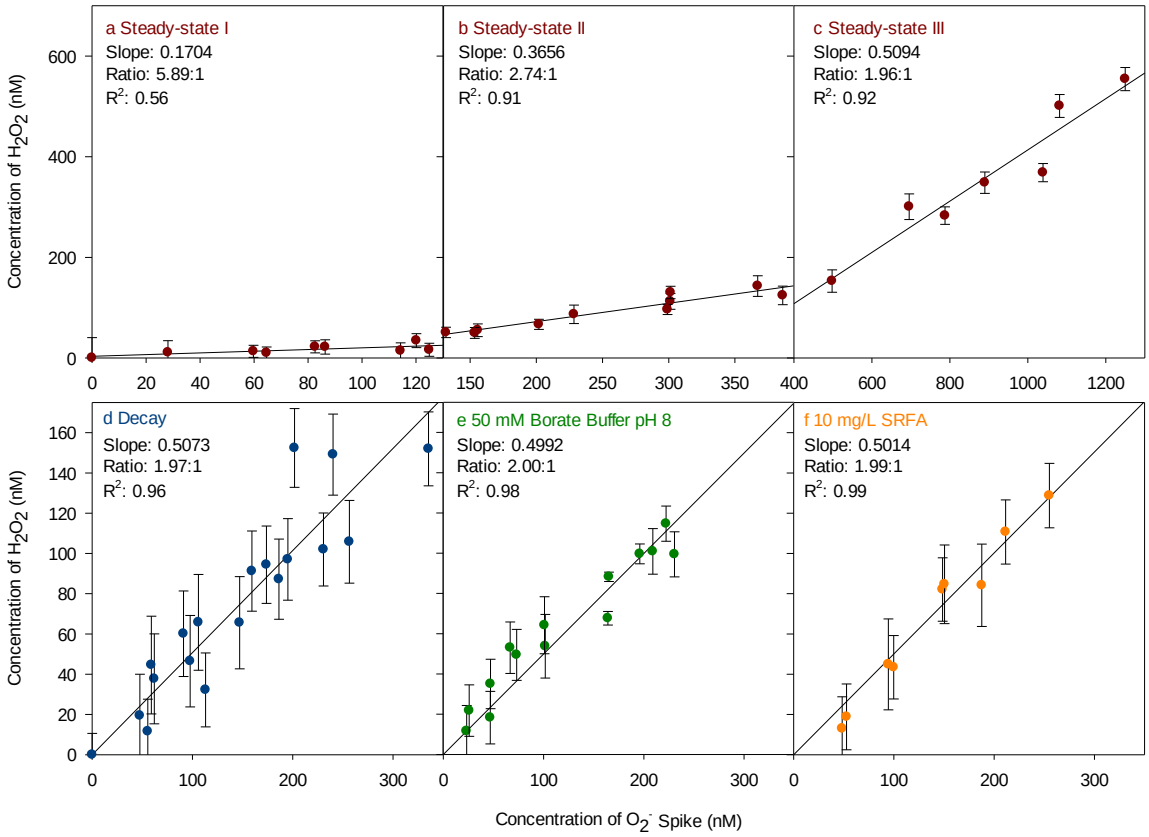

Figure 5.3. Concentration of H_2O_2 produced from $O_2^{\bullet-}$ spikes conducted at steady-state (a-c), during decay (d), in the dark in 50 mM borate buffer pH 8 (e), and in the dark in 10 mg/L SRFA (f). Irradiations were done with the 325 nm cut-off filter. Steady-state spikes were split into 3 regions to emphasize the changes in slope. Ratio values are the inverse of the slope and are therefore the ratio of H_2O_2 produced to $O_2^{\bullet-}$ injected. H_2O_2 produced photochemically by SRFA over the irradiation timeframe of the experiment was subtracted from the steady-state and decay measurements. Error bars are for standard deviation of triplicate measurements post-spike.

This result indicates that $O_2^{\bullet-}$ introduced during irradiation is being consumed by another pathway that is not producing H_2O_2. The sink is largest at spike concentrations ≤ 120 nM, indicating that the sink is smaller than this value. A ratio of 5.89:1 indicates that at least 66% of the $O_2^{\bullet-}$ is being consumed by this sink. Spikes introduced during the decay phase led to the expected 2:1 stoichiometry which was also observed in the controls where $O_2^{\bullet-}$ spikes were introduced in the dark for both 10 mg/L SRFA and 50 mM borate buffer. Other groups have also observed a 2:1 stoichiometry of H_2O_2 production from $O_2^{\bullet-}$ spikes in various samples in the dark.[77,254] Garg et al.[77] further compared the dark results to irradiated conditions and noted that

the H_2O_2 concentration did not increase much post-irradiation despite observable $O_2^{\bullet-}$ decay. It was concluded that the decay occurring post-irradiation was not producing H_2O_2 and that catalyzed dismutation that occurs in the dark is possibly deactivated during irradiation.

5.4.3 Testing for Photodegradation by Superoxide

The possibility of $O_2^{\bullet-}$ being involved in oxidation of CDOM was explored by measuring the absorbance and fluorescence before and after additions of $O_2^{\bullet-}$ spikes during irradiation. Small absorbance changes were observed between the wavelengths (200-450 nm) amounting to about a 5% loss (**Figure 5.4a**). A more significant change was observed in the fluorescence intensity, where up to about a 15% loss was obtained (**Figure 5.4b**). Both percent changes are outside of the range of reproducibility of the instruments (0.6 ± 0.3 % and 2.7 ± 0.5 % for the absorbance spectrophotometer and the fluorometer, respectively). Although a fairly large spike concentration was used (~1250 nM), it is evident from **Figure 5.3** that a large portion of this likely produced H_2O_2. This could be due to issues of injecting such a large quantity of $O_2^{\bullet-}$ into the sample in a single moment. Regardless, the observation of optical changes supports the theory that $O_2^{\bullet-}$ does indeed react with and chemically alter CDOM.

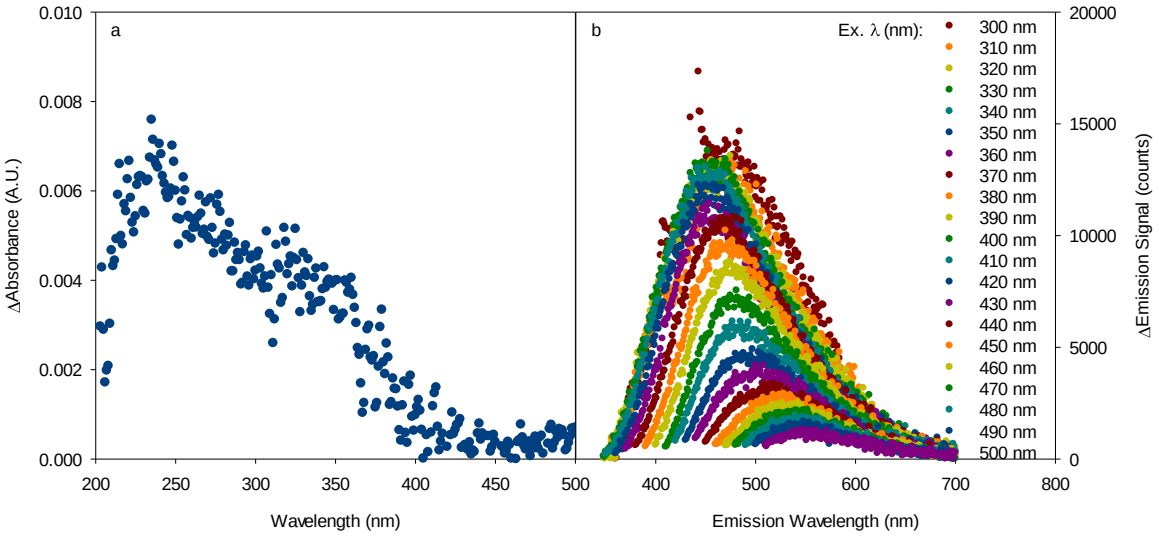

Figure 5.4. Change in absorbance (a) and fluorescence (b) of 10 mg/L SRFA from a 1250 nM superoxide spike injected into the sample during irradiation with a 325 nm cut-off filter. Absorbance decrease amounted to about 5% while the fluorescence decrease was 15% of the original signal.

5.5 Conclusion

Integration analysis of the $O_2^{\bullet-}$ spike data indicates that 40-90% of the $O_2^{\bullet-}$ spike is consumed during irradiation, with more consumption with shorter wavelength cut-off filters. Tests for the production of H_2O_2 post $O_2^{\bullet-}$ spike show that at least 66% of the $O_2^{\bullet-}$ spike does not produce H_2O_2. H_2O_2 production is shown in controls experiments when $O_2^{\bullet-}$ is spiked into samples in the dark, further confirming that the light-dependent sink does not produce H_2O_2. Observations of the changes in the optical properties of CDOM as a result of introducing $O_2^{\bullet-}$ spikes during irradiation show some loss of absorbance and fluorescence, indicating that some of the $O_2^{\bullet-}$ may be reacting with and breaking down CDOM.

Chapter 6: Conclusions and Future Work

6.1 Summary

A nitroxide probe-fluorophore based method to measure OER photoproduced by DOM was developed to be conducted simply and quickly using a fluorometer. Validation and control experiments were conducted that verify the accuracy and precision of the method. Detailed exploration of modifications to the method were also performed to ensure the applicability of the method to natural waters. This method provides reasonable estimates for $O_2^{\bullet-}$ production and has the benefit of being faster and much easier to conduct than the traditional chemiluminescence method for $O_2^{\bullet-}$ detection.

Measurements of photoproduced OER, as hydroxylamine, were successfully performed on a wide variety of reference materials, natural waters, and extracts. The rates of production of hydroxylamine, $O_2^{\bullet-}$, and H_2O_2 (R_H, R_{O2}•-, and R_{H2O2}) were measured on identical samples and under identical experimental conditions, for the first time, which provided insightful evidence for the interconnected relationship of the three species. Apparent quantum yields (Φ_H and Φ_{H2O2}) were measured for a large variety of samples. The yields were positively correlated with smaller molecular weight species of CDOM, as determined by the optical properties of CDOM. The ratio, R_H/R_{H2O2}, was also measured for the suite of samples. Based on the stoichiometry for $O_2^{\bullet-}$ dismutation, and assuming that hydroxylamine production is equivalent to $O_2^{\bullet-}$ production, the ratio should have a value of two. However, values from about five to fifteen were obtained. The large values imply a significant oxidative sink for $O_2^{\bullet-}$ and verify that $O_2^{\bullet-}$ cannot be estimated from doubling H_2O_2 measurements, which was traditionally done.

The theory of a light-dependent oxidative sink for $O_2^{\bullet-}$ had been previously proposed, but no direct evidence for its presence existed. The presence of this light-dependent oxidative sink of $O_2^{\bullet-}$ was directly demonstrated here through $O_2^{\bullet-}$ spiking experiments. $O_2^{\bullet-}$ spikes introduced into a sample during irradiation decayed much faster than $O_2^{\bullet-}$ spikes introduced into a sample post-irradiation or into a sample in the dark. Kinetic modeling of the decay traces allowed for the determination of the first-order rate constants for the light-dependent decay. It was found that they are at least 40-70% larger than those of the $O_2^{\bullet-}$ spikes conducted in the dark, with shorter wavelength irradiation leading to faster decay.

Integration analysis of the $O_2^{\bullet-}$ spike data indicates that 40-90% of the $O_2^{\bullet-}$ spike is consumed during irradiation. To ensure that the sink was oxidative, and did not produce H_2O_2, samples that were spiked with $O_2^{\bullet-}$ were tested for their H_2O_2 concentration post-spike. Spikes introduced during irradiation showed, within a certain spike concentration range, that at least 66% of the $O_2^{\bullet-}$ spike does not produce H_2O_2. H_2O_2 production was at the level expected in control experiments where $O_2^{\bullet-}$ was spiked into samples in the dark, further confirming the light-dependency of the sink.

Several possibilities exist for what the light-dependent, oxidative sink of $O_2^{\bullet-}$ is, though the most intriguing is phenoxy radicals within CDOM. Reaction between $O_2^{\bullet-}$ and model phenoxy radicals have high rate constants of reaction and primarily lead to the loss of the parent phenol. This reaction could be a possible pathway for the transformation of terrestrial DOM as it moves to marine waters. This sink possibility was briefly tested by observing the changes in the absorbance and fluorescence of CDOM as a result of introducing $O_2^{\bullet-}$ spikes during irradiation. Some loss of absorbance and fluorescence was observed, indicating that some of the $O_2^{\bullet-}$ is indeed involved in the degradation of CDOM.

$O_2^{\bullet-}$ and H_2O_2 are reactive oxygen species that are prevalent throughout natural waters and are important in a multitude of environmental processes. Publications have been increasing in attempts at modeling their photoproduction rates to be able to predict their concentrations and subsequently their impact on aquatic environments. The work contained in this dissertation provided insight into the greater magnitude of $O_2^{\bullet-}$ production by CDOM than what was previously believed and provided direct evidence for its light-dependent oxidative sink. This work will hopefully aid in more accurate modeling efforts and provides an additional piece of information for the study of the photodegradation of DOM.

6.2 Future Work

6.2.1 Hydroxylamine Measurements and Optical/Structural Properties

With the development of the fluorescence-based nitroxide probe method that is relatively easy to conduct, more measurements need to be made to continue to increase the diversity of the data available. More OER measurements made in conjunction with the determination of optical properties will continue to enhance the elucidation of the relationship between OER production and the structural features of DOM. Although a variety of possible optical properties were tested, the determination of OER production and dissolved organic carbon content of a given sample will provide even more correlations to optical properties such as $SUVA_\lambda$ and mass normalized absorption coefficients.

6.2.2 Additional Superoxide Spiking Experiments

Though I demonstrated the presence of a significant oxidative, light-dependent sink within CDOM, only SRFA has been studied so far. Other reference materials should be studied next to compare the magnitude of the sink among them. This would be the next logical step since

a significant amount of data exists on the optical/structural features of these materials and is readily available from the International Humic Substance Society website. From there, spiking experiments should be conducted on natural waters and extracts for comparison. The concentration dependence of CDOM on $O_2^{\bullet-}$ spike consumption should also be examined.

Additionally, competition experiments should be developed where external sinks for $O_2^{\bullet-}$ are added into the sample to test for competition between the external sink and the sink within CDOM. Another complement experiment to this would be to perform $O_2^{\bullet-}$ spikes on sodium borohydride reduced samples. Sodium borohydride reduces aldehydes and ketones (irreversibly) and quinones (reversibly).[79] Although the $O_2^{\bullet-}$ sink is believed to be due to phenols, performing spikes on reduced samples would confirm the lack of involvement of aldehydes/ketones if the reduction shows to have no impact on the rate or magnitude of loss of the $O_2^{\bullet-}$ spike.

6.2.3 Effect of Fractionation

Fractionation of DOM, either by polarity or size, and relations between different fractions and their photochemical efficiencies for producing reactive oxygen species is a fairly new area of research. Correlations have been observed between photochemical efficiencies and optical properties wherein optical properties are then tied to structural properties of the DOM as discussed in Chapter 3. One study found that the < 1 kDa fraction had a higher quantum yield for H_2O_2 production than the > 1 kDa fraction.[272] In regards to polarity, one study separated wastewater into hydrophobic, transphilic, and hydrophilic fractions. The apparent quantum yields of $O_2^{\bullet-}$ and H_2O_2 increased going from hydrophilic to hydrophobic to transphilic.[273] A study that looked at adsorption of DOM to ferrihydrite, which selects for highly unsaturated (oxygen-rich) structures (oxidized polycyclic aromatics or polyphenols), found decreased in $O_2^{\bullet-}$ production.[274] In order to fully study structural/compositional trends with ROS production, more

research needs to be conducted using these fractionation/adsorption methods. These studies will help better define relationships between ROS production to the size of DOM and its composition/polarity, since the presence of smaller structures does not always necessarily mean the presence of more oxygen-containing functional groups or increased polarity.

Appendix 1: Supporting Information for Chapter 2

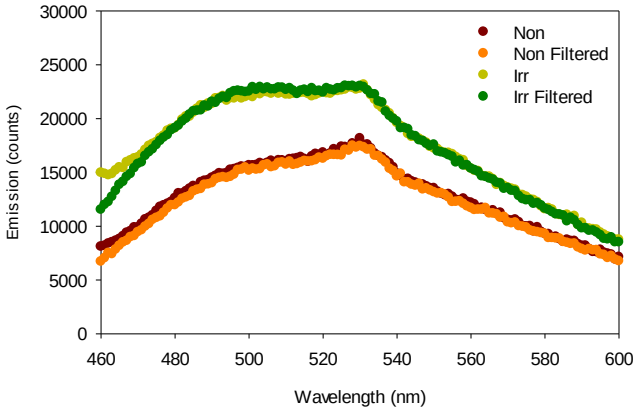

Figure A2.1. Raw emission intensity for a non-irradiated (Non) and 325 nm irradiated (Irr) DR EX (St. 19) sample that was allowed to settle before measurement and was then filtered with a 0.2 µm nylon filter and measured again.

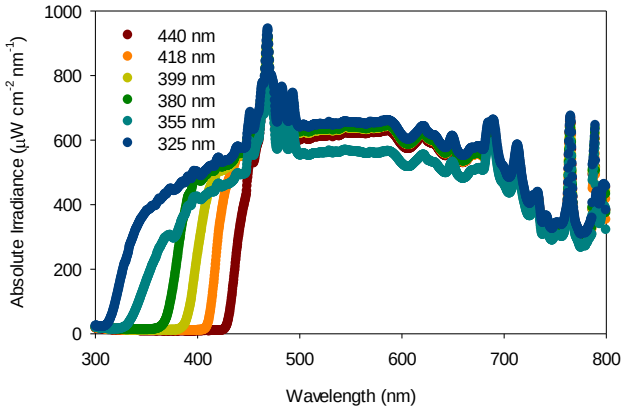

Figure A2.2. Absolute irradiance measurements of 300 W xenon arc lamp with 20 cm water jacket and various long-pass cut-off filters. Ocean Optics USB2000 spectroradiometer fitted with a fiber optic cable and cosine corrector. Cosine corrector was placed at the location of where a cuvette would stand for irradiation. Integration time 57 s, boxcar width 5 nm, number of scans averaged 3.

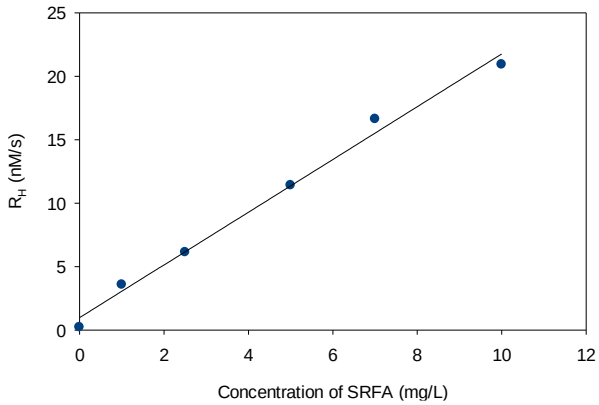

Figure A2.3. Dependence of R_H on concentration of SRFA. Irradiations were done with 325 nm cut-off for 15 minutes. Linear fit has an equation of y = 2.1(±0.1)x + 1.0(±0.5) with an R^2 of 0.99.

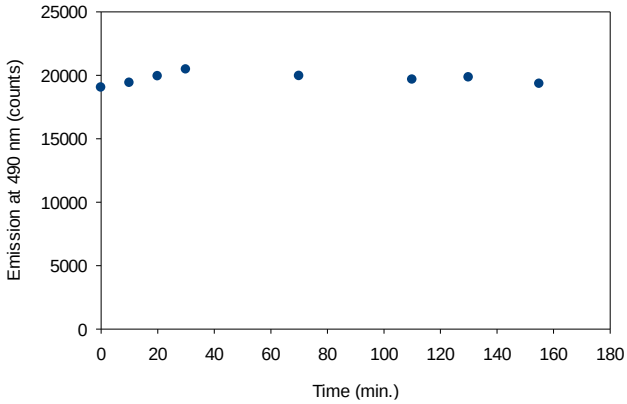

Figure A2.4. Emission intensity for an irradiated and derivatized 10 mg/L SRNOM with 600 µM 3AP. The sample was exposed to air post-derivatization and was monitored over time. Irradiation was conducted with the 380 nm cut-off filter.

Text A2.1 Derivation of Initial Production Rate of Hydroxylamine Equation (Eqn. 2.4)

The initial production rate of hydroxylamine is given by:

$$R_H = \left(\frac{d[H]}{dt}\right)_0 = k_{3AP}[3AP][OER] \qquad \text{(Eqn. A2.1)}$$

The change of OER over time is given by:

$$\left(\frac{d[OER]}{dt}\right) = R_f - k_{O_2}[O_2][OER] - k_{3AP}[3AP][OER] - k_d[OER] \qquad \text{(Eqn. A2.2)}$$

Using the steady-state approximation, $\frac{d[OER]}{dt} = 0$, and it is assumed that the formation rate of OER is equal to its loss. Rearranging Eqn. A2.2 and solving for [OER] gives:

$$[OER] = \frac{R_f}{k_{O_2}[O_2]+k_{3AP}[3AP]+k_d} \quad \text{(Eqn. A2.3)}$$

Plugging Eqn. A2.3 into Eqn. A2.1 gives:

$$R_H = \left(\frac{d[H]}{dt}\right)_0 = k_{3AP}[3AP]\left(\frac{R_f}{k_{O_2}[O_2]+k_{3AP}[3AP]+k_d}\right) \quad \text{(Eqn. A2.4)}$$

Re-arrangement of the equation gives the final form (Eqn. 2.4 in main text):

$$R_H = \left(\frac{d[H]}{dt}\right)_0 = \frac{R_f[3AP]}{\left(\frac{(k_d + k_{O2}[O_2])}{k_{3AP}} + [3AP]\right)} \quad \text{(Eqn. A2.5)}$$

Other possible side reactions include oxidation of the hydroxylamine by $O_2^{\bullet-}$ and oxidation of the nitroxide by $O_2^{\bullet-}$. However, the rate constant for reaction between hydroxylamine and $O_2^{\bullet-}$ has been found to be ~10^3 $M^{-1}s^{-1}$ [275], which is an order of magnitude smaller than the rate constant for $O_2^{\bullet-}$ dismutation. The reaction between the nitroxide with $O_2^{\bullet-}$ to produce the oxoammonium cation, could then be reduced by $O_2^{\bullet-}$ to form a catalytic cycle for $O_2^{\bullet-}$ dismutation and recycle the probe, but the rate constants for these reactions are also small.[190,276]

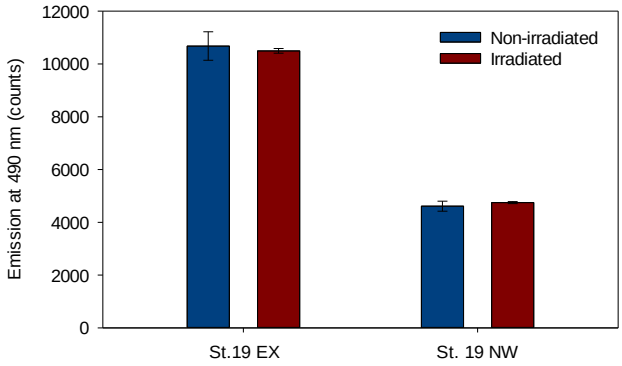

Figure A2.5. Emission signals for non-irradiated and irradiated 5 mg/L DR St. 19 EX and St. 19 NW. Samples were irradiated without 3AP and were derivatized after. Error bars represent the standard deviation of triplicate measurements.

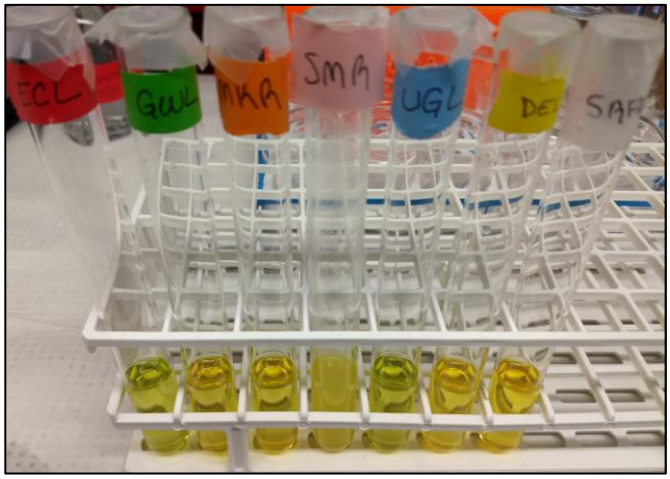

Figure A2.6. Presence of ammonia test results. Test was conducted with an API ammonia (NH_3/NH_4^+) test kit. Golden yellow color indicated 0 mg/L ammonia (as in Suwannee River Fulvic Acid; far right). Light green color indicated 0.25 mg/L ammonia (as in Echo Lake and Upper Greenwood Lake; red and blue label respectively. St. Mary's River (pink label) is a cloudy yellow due to slight salinity of the sample.

Appendix 2: Supporting Information for Chapter 3

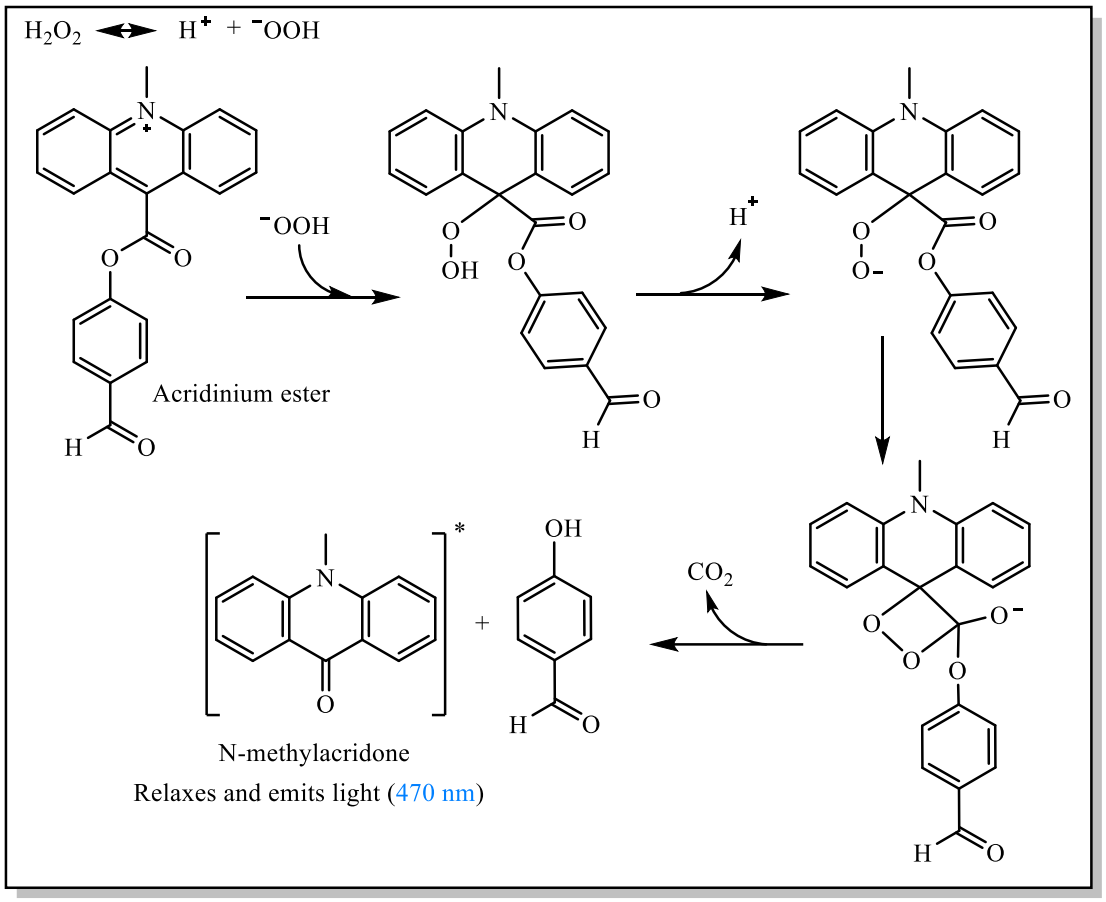

Figure A3.1. Reaction scheme for the production of chemiluminescence from the breakdown of AE by H_2O_2.

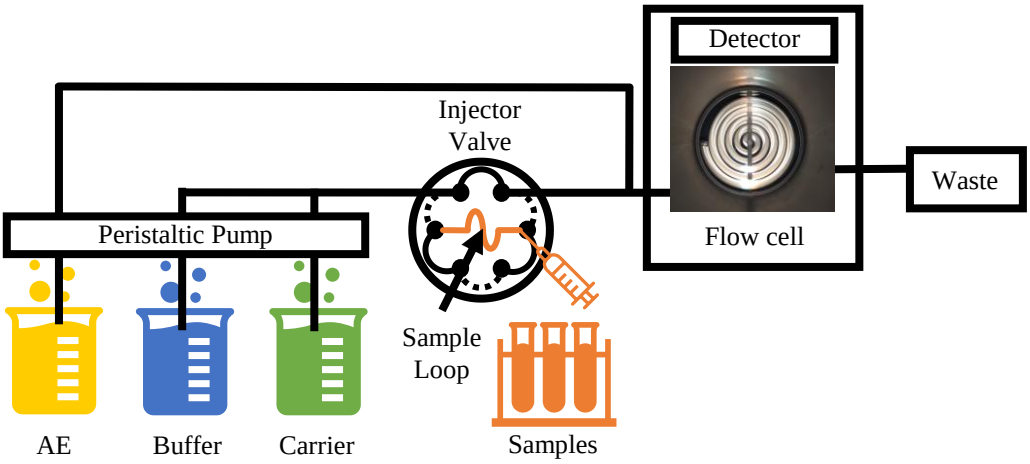

Figure A3.2. FeLume instrument set-up for H_2O_2 analysis. Detector is a photomultiplier tube.

Text A3.1. Potassium Permanganate Titration of Hydrogen Peroxide

About 2 grams of the ~30% H_2O_2 solution was weighed in a 250 mL volumetric flask and filled to the mark with MQ water. The solution was mixed thoroughly and 25 mL was transferred to a 400 mL beaker that contained 250 mL MQ water and 10 mL of concentrated sulfuric acid. A stir bar was placed in the beaker, and this was placed on a stir plate. The solution was titrated with 0.1 N $KMnO_4$ until the presence of a faint pink color stayed permanently. The titration was performed in triplicate. This procedure is based on the assay by USP technologies™. The percent H_2O_2 was calculated with the following equation:

$$\%H_2O_2 = \frac{vol.\ KMnO_4\ (mL) * 0.3\ N * 0.01701 * 1000}{mass\ H_2O_2\ (g)} \qquad \text{(Eqn. A3.1)}$$

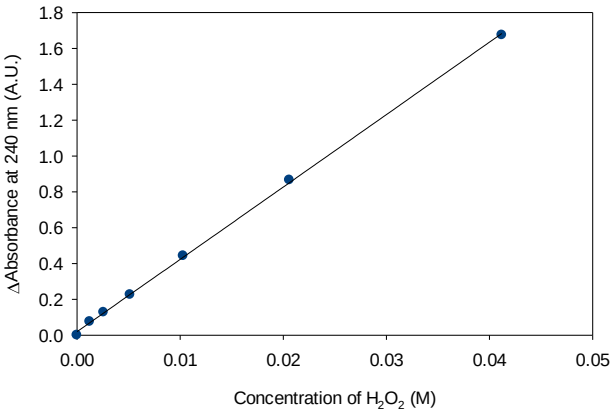

Figure A3.3. Blank subtracted absorbance obtained for various standard concentrations of hydrogen peroxide. MQ was used as the blank. Linear fit has an equation of y = 40.4 (±0.3)x with an R^2 of 0.99.

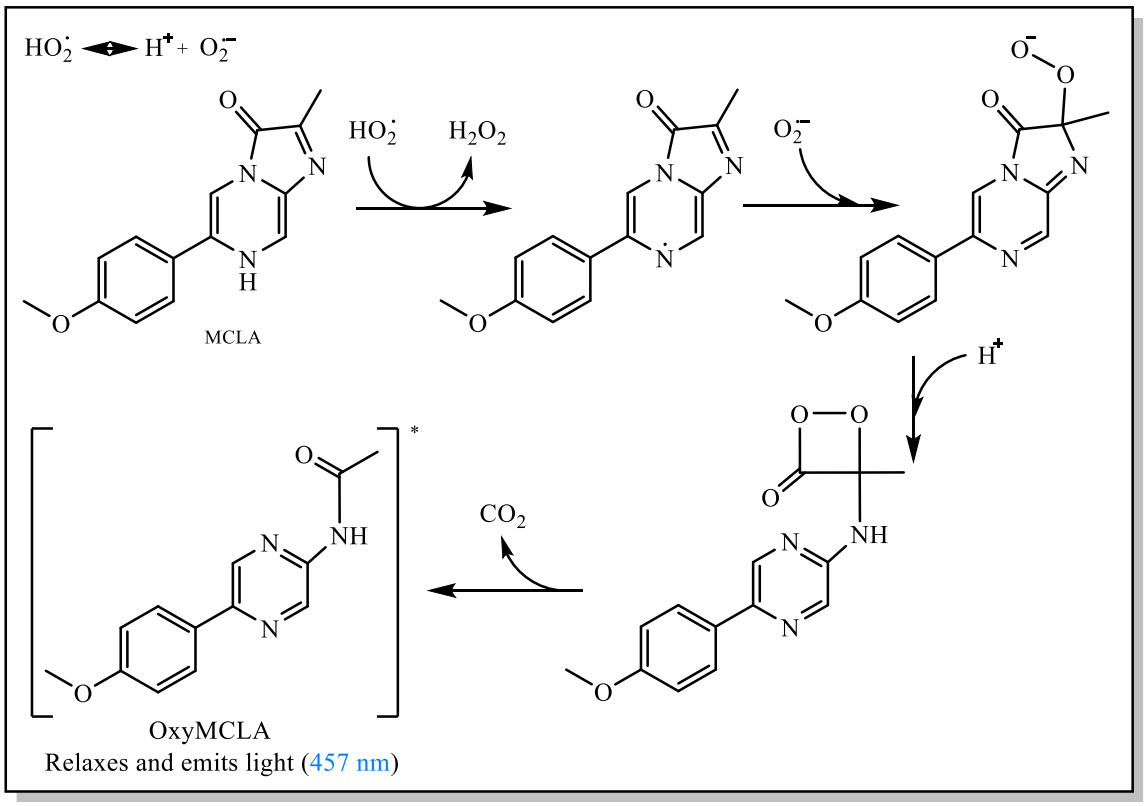

Figure A3.4. Reaction scheme for the production of chemiluminescence from the breakdown of MCLA by $O_2^{\bullet-}$.

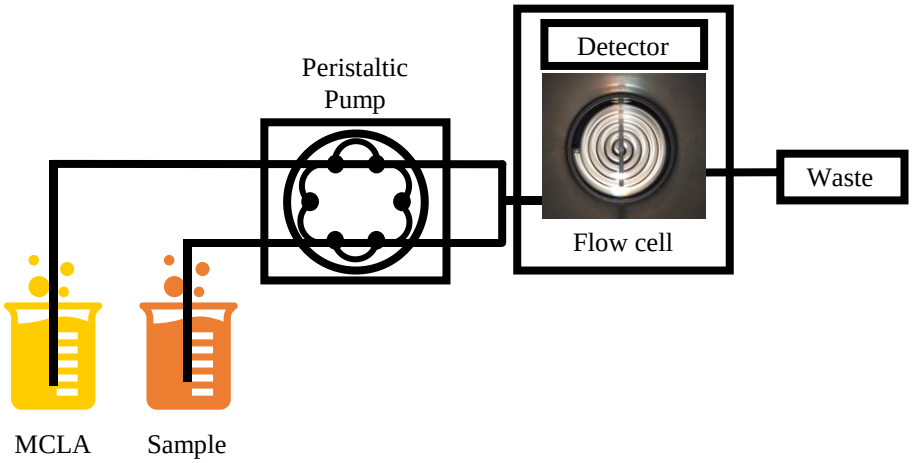

Figure A3.5. FeLume instrument set-up for $O_2^{\bullet-}$ analysis. Detector is a photomultiplier tube.

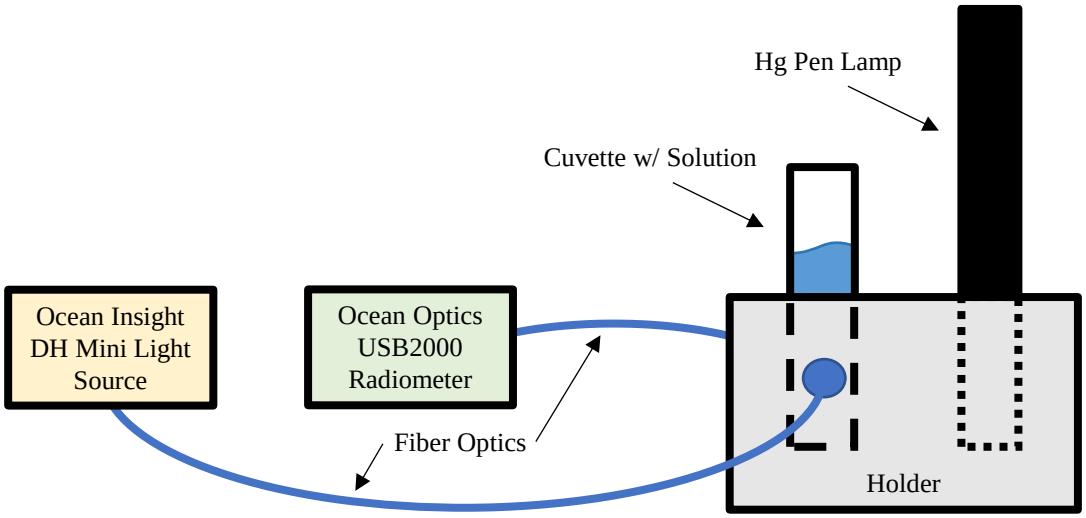

Figure A3.6. Instrument set-up for photolysis of acetone/ethanol solution for generation of $O_2^{\bullet-}$ stock solution.

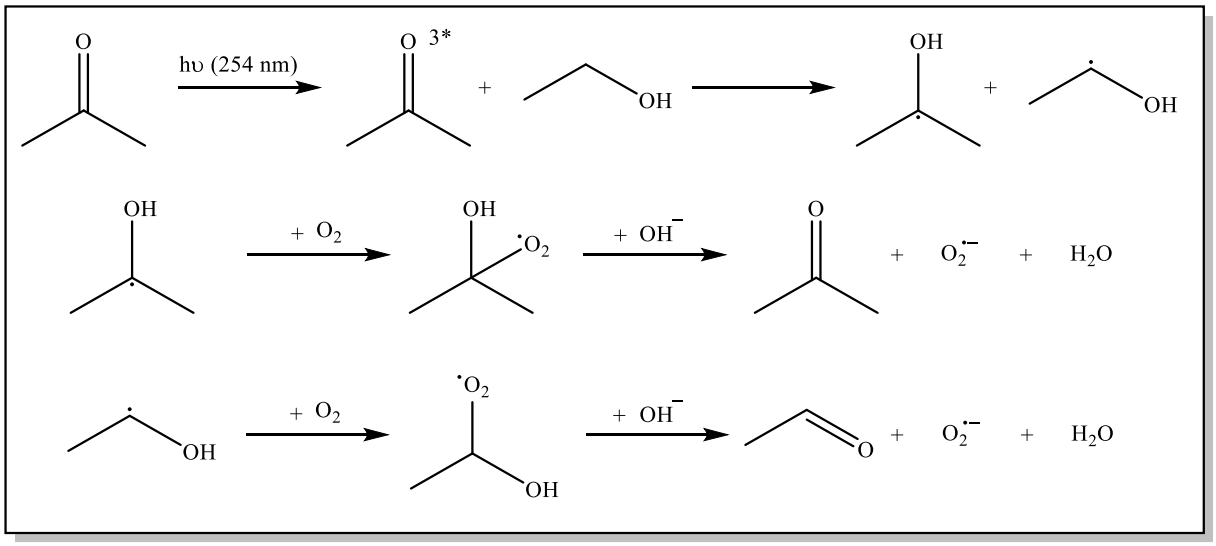

Figure A3.7. Reaction sequence for the generation of $O_2^{\bullet-}$ from the photolysis of the acetone/ethanol solution.

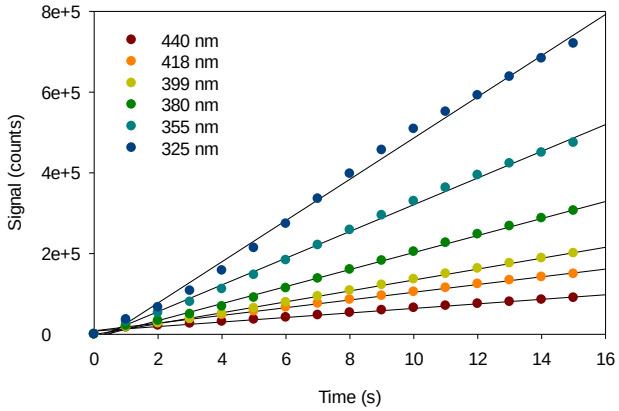

Figure A3.8. Signal vs. time for the wavelength dependence of the initial net $R_{O2^{\bullet-}}$ during the first 15 seconds of irradiation of 1 mg/L SRFA.

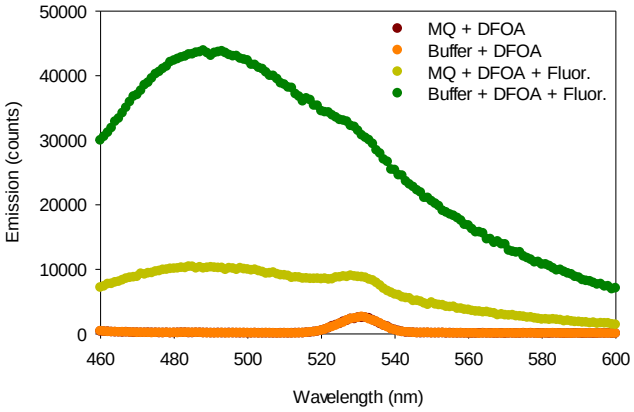

Figure A3.9. Derivatization of DFOA in MQ and 50 mM borate buffer pH 8. MQ + DFOA and buffer + DFOA overlap.

Text A3.2. Derivation of Percent Loss of Superoxide Equation (Eqn. 3.3)

Assuming that all one-electron reductants that react with molecular oxygen to produce $O_2^{\bullet-}$ under aerobic conditions also react with the radical probe 3AP to produce hydroxylamine under anaerobic conditions, then $R_H = R_{O2^{\bullet-}}$ and the following relationship is obtained:

$$\frac{R_H}{R_{H2O2}} = \frac{R_{O2-}}{R_{H2O2}} \qquad \text{(Eqn. A3.1)}$$

The production rate of H_2O_2 (R_{H2O2}) will be half the value of $R_{O2^{\bullet-}}$ that is not consumed by other oxidative pathways (P_{O2-}):

$$R_{H2O2} = \frac{1}{2}[R_{O2}(1 - P_{O2-})] \qquad \text{(Eqn. A3.2)}$$

Plugging Eqn. A3.2 into Eqn. A3.1 provides the final form for Eqn. 3.3 in the main text:

$$\frac{R_H}{R_{H2O2}} = \frac{2R_{O2-}}{[R_{O2-}(1-P_{O2-})]} \qquad \text{(Eqn. A3.3)}$$

Appendix 3: Supporting Information for Chapter 4

Text A4.1. Comment on the Use of Metal Chelators in Superoxide Studies

Diethylenetriaminepentaacetic acid (DTPA) has been commonly added to samples for $O_2^{\bullet-}$ studies to prevent metal-catalyzed reactions.[126,231,254,255,259] However, the use of DTPA in samples that undergo irradiation has been criticized due to the photodegradation of DTPA and its metal complexes.[277–279] $O_2^{\bullet-}$ dark decay was also tested in 50 mM borate buffer pH 8 with and without 30 µM DTPA as well as in solutions of 1 mg/L SRFA in 50 mM borate buffer pH 8 with and without 30 µM DTPA. Samples with DTPA were allowed to equilibrate overnight. Only small differences in $O_2^{\bullet-}$ decay were observed between the solutions of the buffer with and without DTPA (**Figure A4.1a, 4.1b**). The theoretical rate constant for dismutation in seawater is $5x10^{12}$ x $[H^+]$ $M^{-1}s^{-1}$ so at a pH of 8 in the experiments here, a value of $5x10^4$ $M^{-1}s^{-1}$ would be expected.[85] The value obtained for buffer with DTPA was $1.84x10^5$ $M^{-1}s^{-1}$ (**Figure A4.2**) which is higher than the expected value but this is also in a non-saline buffer solution. Dismutation rates are expected to be roughly 3-5 times faster in purer water as compared to seawater.[243] More significant differences were observed for 1 mg/L SRFA with and without DTPA (**Figure A4.1c, A4.1d; Figure A4.2**). These results indicate that either DTPA interferes in some way with the dark reaction between $O_2^{\bullet-}$ and SRFA or that SRFA itself contains metal ions that react with $O_2^{\bullet-}$.

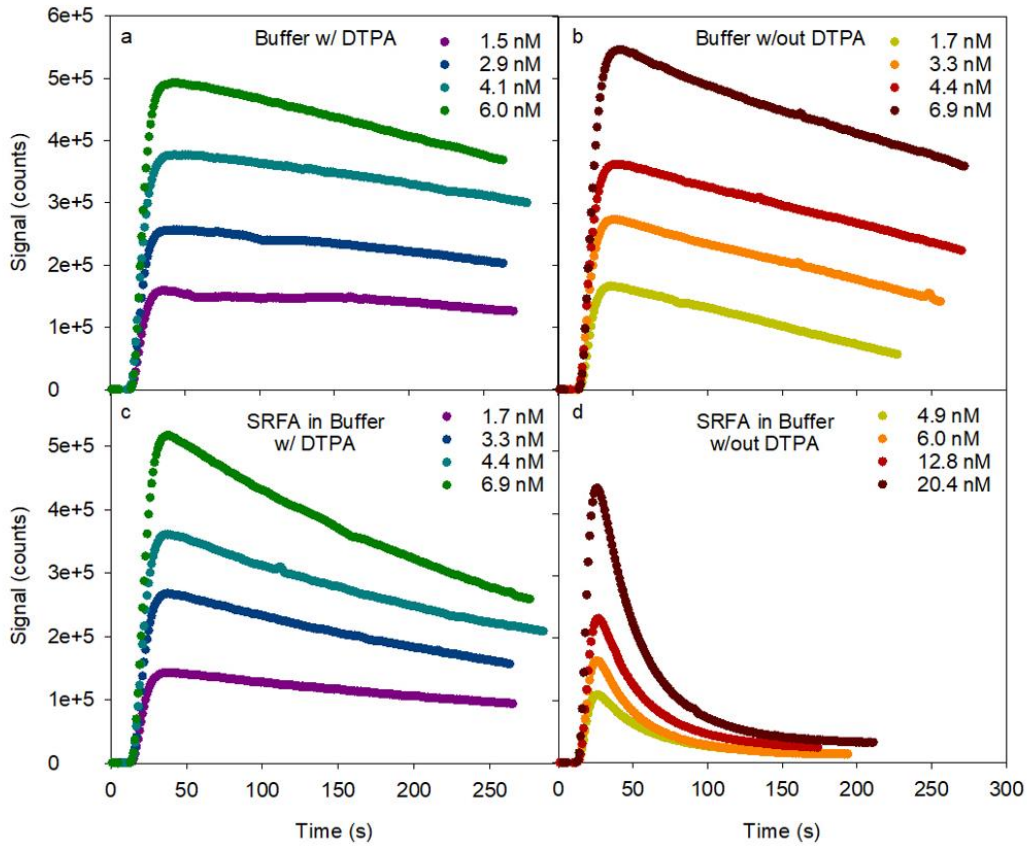

Figure A4.1. Signals for $O_2^{\bullet-}$ decay in 50 mM borate buffer pH 8 with 30 µM DTPA (a) and without DTPA (b) and in 1 mg/L SRFA in buffer with (c) and without DTPA (d). t = 0 is when the sample was spiked.

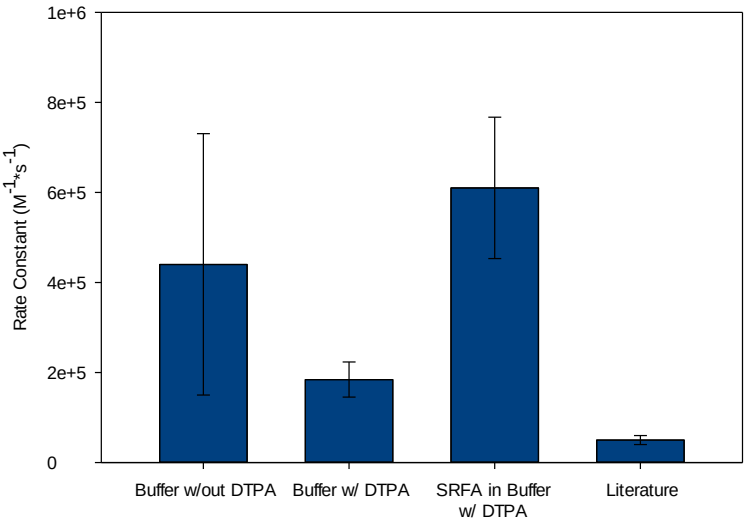

Figure A4.2. Second-order rate constants obtained from fits to the data presented in panels a-c of Figure A4.1 and the literature value for uncatalyzed $O_2^{\bullet-}$ dismutation.

A variety of DTPA concentrations have been used in the literature (from 1-50 µM) though no studies exist, to our knowledge, on the concentration dependence of rate constants with DTPA concentration with regards to the presence of CDOM (separate from affects due to trace metal contaminated buffer). One study found a 16% decrease in the rate constant of $O_2^{\bullet-}$ decay in a low concentration of SRFA (0.041 mM_c) with 1 µM DTPA but no change occurred thereafter going up to 10 µM DTPA.[255] Even though SRFA is an extracted material, it has been shown that strongly complexed metals can be extracted so it is possible that SRFA contains them.[252,253,280] DTPA was not used in further experiments to prevent having issues with possible interferences or having concerns about degradation of the DTPA.

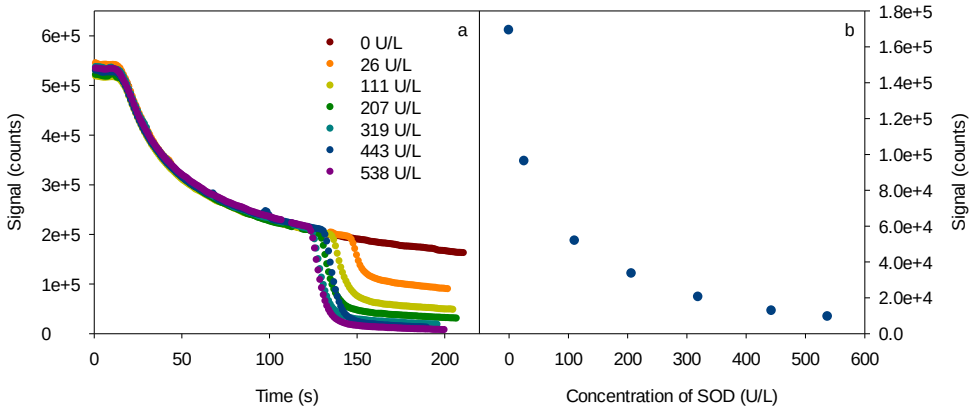

Figure A4.3. Signal for $O_2^{\bullet-}$ decay post-irradiation of 1 mg/L SRFA with a 325 nm cut-off filter. t=0 is the time the sample was removed from the light. Various concentrations of SOD were added at approximately 100 s to observe the loss of signal. Pre-irradiation baselines obtained for 1 mg/L SRFA were subtracted from the data.

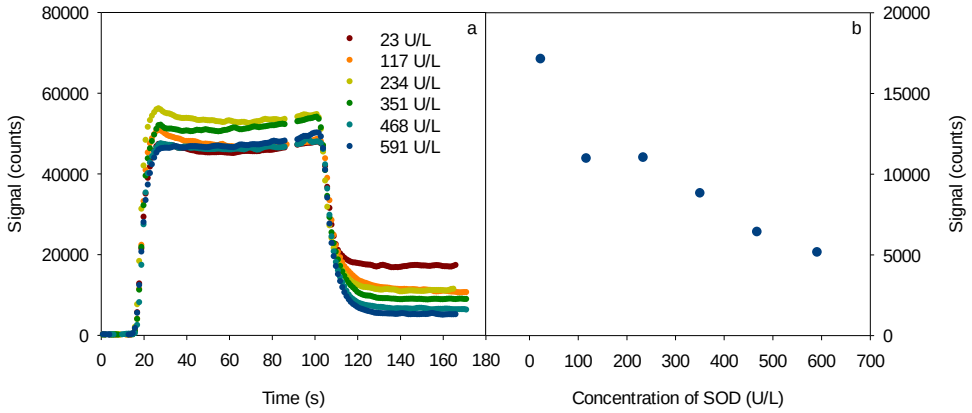

Figure A4.4. Baseline chemiluminescence signal in the presence of 1 mg/L SRFA in 50 mM borate buffer pH 8. t=0 is the time that the sample line was switched from MQ to 1 mg/L SRFA. Various concentrations of SOD were added at approximately 90 s to observe the loss of signal in the blank. MQ baselines were subtracted from the data.

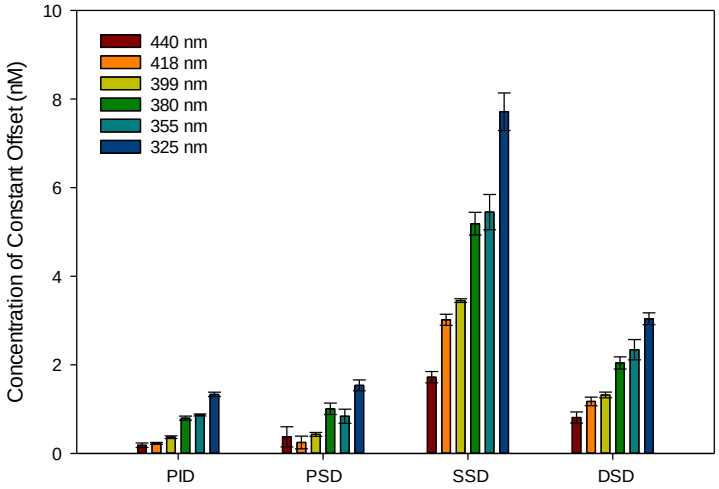

Figure A4.5. Values obtained for the constant value in the fits for each wavelength cut-off filter and for all $O_2^{\bullet-}$ decay modeled. SSD constant offsets are the steady-state concentrations themselves. Error bars are for standard deviation of triplicate measurements.

Text A4.2. Previously Used Modeling Methods for Superoxide

$O_2^{\bullet-}$ decay traces have been modeled by combining the self-dismutation reaction and a pseudo-first order sink that is meant to encompass other decay pathways.[77,126,254,257,259,263] By

assuming that at steady-state, production is equal to decay, the following rate equation is obtained:

$$\frac{-d[O_2^{\bullet-}]}{dt} = 2k_D[O_2^{\bullet-}]_{SS}^2 + k_{pseudo}[O_2^{\bullet-}]_{SS} \quad \text{(Eqn. A4.1)}$$

where k_D is the self-dismutation rate constant, k_{pseudo} is the rate constant for the culmination of other dark decay pathways, and $[O_2^{\bullet-}]_{SS}$ is the steady-state concentration of $O_2^{\bullet-}$. The following equation is obtained after integration of the above equation and solving for $[O_2^{\bullet-}]$:

$$[O_2^{\bullet-}] = \frac{k_{pseudo}[O_2^{\bullet-}]_0}{k_{pseudo}e^{k_{pseudo}t} + 2k_D[O_2^{\bullet-}]_0\left(e^{k_{pseudo}t} - 1\right)} \quad \text{(Eqn. A4.2)}$$

where k_D is the self-dismutation rate constant, k_{pseudo} is the rate constant for the culmination of other dark decay pathways, t is time, and $[O_2^{\bullet-}]_0$ is the initial concentration of $O_2^{\bullet-}$. Since the FeLume signal is presumably directly proportional to the $O_2^{\bullet-}$ concentration, the equation can be re-written based on $[O_2^{\bullet-}] = S/C$ (where S is the signal and C is the calibration coefficient) to give [77,126,257,263]:

$$S = \frac{k_{pseudo}S_0}{k_{pseudo}e^{k_{pseudo}t} + 2k_D[O_2^{\bullet-}]_0\left(e^{k_{pseudo}t} - 1\right)} \quad \text{(Eqn. A4.3)}$$

Typically, only the first minute of decay data is fit to this equation, though some works have found the equation to fit out past that timescale.[77,257] If this equation is fit to a post-irradiation decay, the $[O_2^{\bullet-}]_0$ is the $[O_2^{\bullet-}]_{SS}$ and this can be used with the k_{pseudo} to calculate the decay rate with equation A4.1. kD is usually determined using the pH-dependent equation and plugging in the experimental pH ($k = 5 \pm 1 \times 10^{12} \times [H^+]$).[81] Assuming that at steady-state, the decay rate of $O_2^{\bullet-}$ is equal to the production rate, then the calculated decay rate is the production rate. The problem with this method is that k_{pseudo} is measured post-irradiation, in the dark, so any light-dependent pathways are unaccounted for.

Ma et al. used an alternative of the steady-state approximation, where they measured the initial production rate and steady-state concentration and used these to back calculate the decay rate constant.[259] The calculated decay rate constant is then considered a total decay rate constant which is the summation of the rate constants for all decay routes:

$$k_{decay} = k_{light} + k_{dark} = k_{light} + k_{pseudo} + 2k_D[O_2^{\bullet -}]_{SS} \qquad \text{(Eqn. A4.4)}$$

Subtracting out the dark decay terms (k_{pseudo} for dark decay and k_D for self-dismutation) provides the remaining decay constant due to light-dependent pathways. The issue with this method is that the initial production rates are still considered net production rates, because loss is still occurring even during the initial stages of irradiation.

Table A4.1. Kinetic Fitting Data for Irradiations with 325 nm Cut-off Filter

Fit	Trial	$[O_2^{\bullet-}]$ (nM)	a (nM)	SD	b	SD	+ c (nM)	SD	R^2
PID 1st	1	-	7.6	0.1	0.0211	0.0007	2.65	0.05	0.9927
	2	-	7.7	0.1	0.0217	0.0007	2.58	0.04	0.9944
	3	-	7.1	0.2	0.0201	0.0007	2.55	0.05	0.9917
PID 2nd	1	-	12.0	0.2	0.00360	0.00008	1.39	0.03	0.9990
	2	-	12.2	0.1	0.00368	0.00006	1.32	0.02	0.9995
	3	-	11.1	0.2	0.00351	0.00009	1.30	0.04	0.9988
SSD 1st	1	19.1	9	1	0.099	0.004	7.10	0.01	0.9970
	2	44.5	16	1	0.080	0.003	7.97	0.02	0.9967
	3	41.2	16	1	0.084	0.003	8.02	0.02	0.9980
	4	44.5	17	1	0.082	0.003	7.78	0.02	0.9976
	5	12.8	15	2	0.100	0.006	8.61	0.02	0.9946
PSD 1st	1	19.1	6.4	0.1	0.0251	0.0008	2.66	0.04	0.9985
	2	44.5	7.27	0.09	0.0283	0.0008	3.15	0.04	0.9967
	3	41.2	7.4	0.1	0.0273	0.0009	3.00	0.04	0.9976
	4	44.5	7.4	0.1	0.0269	0.0007	2.89	0.04	0.9976
	5	12.8	7.4	0.1	0.0260	0.0009	3.59	0.05	0.9971
PSD 2nd	1	19.1	9.7	0.1	0.0045	0.0001	1.39	0.03	0.9996
	2	44.5	10.9	0.2	0.0041	0.0002	1.57	0.06	0.9992
	3	41.2	12.0	0.2	0.0046	0.0001	1.68	0.03	0.9995
	4	44.5	11.8	0.2	0.0044	0.0001	1.51	0.04	0.9995
	5	12.8	11.2	0.2	0.0039	0.0001	2.06	0.06	0.9992
DSD 1st	1	16.7	9.4	0.2	0.0269	0.0007	2.86	0.03	0.9974
	2	42.2	22.3	0.3	0.0299	0.0004	3.08	0.03	0.9991
	3	38.6	27.5	0.4	0.0335	0.0004	3.18	0.04	0.9989
	4	41.3	22.3	0.4	0.0316	0.0005	3.04	0.04	0.9985
	5	12.3	11.8	0.4	0.031	0.001	2.98	0.05	0.9904
DSD 2nd	1	16.7	39	4	0.00518	0.00008	1.72	0.02	0.9976
	2	42.2	104	22	0.00254	0.00008	0.57	0.09	0.9984
	3	38.6	213	103	0.0025	0.0001	0.5	0.1	0.9970
	4	41.3	116.6	28	0.00275	0.00009	0.63	0.09	0.9982
	5	12.3	50	8	0.0051	0.0001	1.74	0.04	0.9983

PID – post-irradiation decay, SSD – steady-state spike decay, PSD – post-steady-state spike decay, DSD – decay spike decay. $[O_2^{\bullet-}]$ is the concentration of the spike determined by absorbance of the stock solution. First-order equation is [a*exp(-b*x)+c] and second-order equation is [(1/((1/a)+(b*x)))+c]Term a is the intercept value for the $[O_2^{\bullet-}]$ from the fitting. Term b is the rate constant (s^{-1} for first-order or $nM^{-1}*s^{-1}$ for second-order) from the fitting. Term +c is the constant offset term from the fitting. SD values are from the error in the fit.

Table A4.2. Kinetic Fitting Data for SSD for all Wavelength Cut-off Filters

Fit	Trial	$[O_2^{\bullet-}]$ (nM)	a (nM)	SD	b	SD	+c (nM)	SD	R^2
325 nm SSD 1st	1	19.1	9	1	0.099	0.004	7.10	0.01	0.9970
	2	44.5	16	1	0.080	0.003	7.97	0.02	0.9967
	3	41.2	16	1	0.084	0.003	8.02	0.02	0.9980
	4	44.5	17	1	0.082	0.003	7.78	0.02	0.9976
	5	12.8	15	2	0.100	0.006	8.61	0.02	0.9946
355 nm SSD 1st	1	19.0	24	3	0.084	0.005	4.86	0.04	0.9936
	2	19.4	14	1	0.076	0.004	5.57	0.03	0.9961
	3	21.3	16	1	0.078	0.003	5.62	0.03	0.9964
	4	35.4	17	1	0.074	0.003	5.75	0.03	0.9972
	5	14.4	23	3	0.088	0.005	6.92	0.06	0.9935
380 nm SSD 1st	1	13.8	22	1	0.077	0.003	4.81	0.02	0.9968
	2	9.5	14.8	0.8	0.075	0.002	5.27	0.01	0.9980
	3	12.9	21	1	0.076	0.002	5.35	0.02	0.9985
	4	11.7	18	1	0.073	0.003	5.33	0.03	0.9967
399 nm SSD 1st	1	14.6	16	1	0.063	0.003	3.47	0.04	0.9981
	2	17.0	19.5	0.9	0.064	0.002	3.47	0.03	0.9982
	3	15.6	19.6	0.9	0.068	0.002	3.47	0.03	0.9985
	4	13.5	15.3	0.7	0.066	0.002	3.39	0.02	0.9987
418 nm SSD 1st	1	15.3	16.6	0.5	0.060	0.001	3.11	0.02	0.9990
	2	17.6	21.2	0.8	0.061	0.001	3.12	0.02	0.9986
	3	10.5	10.7	0.6	0.059	0.002	2.98	0.02	0.9973
	4	11.1	11.0	0.3	0.063	0.001	2.856	0.009	0.9989
440 nm SSD 1st	1	14.0	19.5	0.4	0.0511	0.0008	1.94	0.02	0.9991
	2	8.7	9.6	0.3	0.051	0.001	1.71	0.02	0.9990
	3	4.5	4.5	0.2	0.056	0.001	1.641	0.007	0.9986
	4	9.6	9.1	0.2	0.0550	0.0009	1.680	0.007	0.9993
	5	4.4	4.5	0.2	0.054	0.002	1.64	0.01	0.9979

SSD – steady-state spike decay. $[O_2^{\bullet-}]$ is the concentration of the spike determined by absorbance of the stock solution. First-order equation is [a*exp(-b*x)+c]. Term a is the intercept value for the $[O_2^{\bullet-}]$ from the fitting. Term b is the rate constant (s^{-1} for first-order) from the fitting. Term +c is the constant offset term from the fitting. SD values are from the error in the fit.

Appendix 4: Supporting Information for Chapter 5

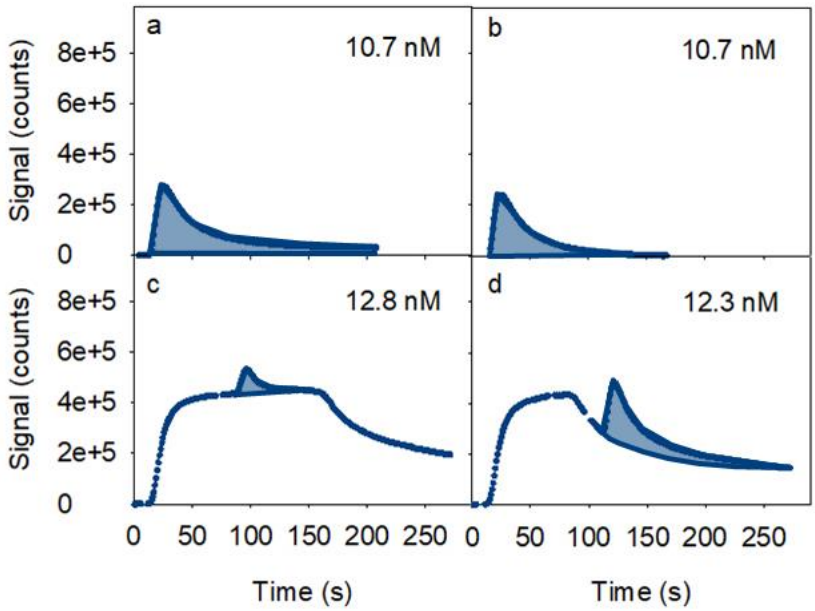

Figure A5.1. Visual representation of integration areas. Shaded regions indicate the area that was integrated for standards for method 1 (a) and method 2 (b) as well as for steady-state spikes (c) and decay spikes (d). Irradiations for this data were done with the 325 nm cut-off filter.

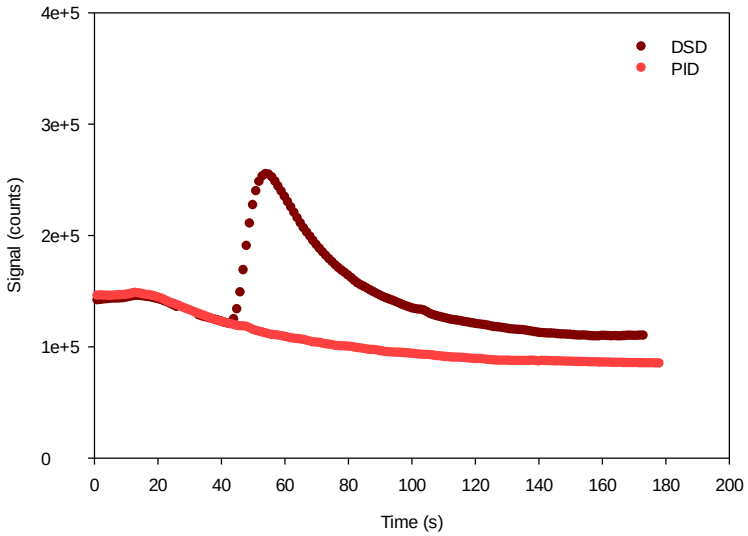

Figure A5.2. Demonstration of the alignment issue of normal post-irradiation decay (PID) curve below the decay spike trace (DSD). Irradiation was conducted with 440 nm cut-off filter.

Bibliography

(1) Baalen, C. V.; Marler, J. E. Occurrence of Hydrogen Peroxide in Sea Water. *Nature* **1966**, *211* (5052), 951. https://doi.org/10.1038/211951a0.

(2) Zafiriou, O. C. Marine Organic Photochemistry Previewed. *Mar. Chem.* **1977**, *5* (4), 497–522. https://doi.org/10.1016/0304-4203(77)90037-8.

(3) Baxter, R. M.; Carey, J. H. Evidence for Photochemical Generation of Superoxide Ion in Humic Waters. *Nature* **1983**, *306* (5943), 575–576. https://doi.org/10.1038/306575a0.

(4) Draper, W. M.; Crosby, D. G. The Photochemical Generation of Hydrogen Peroxide in Natural Waters. *Arch. Environ. Contam. Toxicol.* **1983**, *12* (1), 121–126. https://doi.org/10.1007/BF01055010.

(5) Cudd, A.; Fridovich, I. Electrostatic Interactions in the Reaction Mechanism of Bovine Erythrocyte Superoxide Dismutase. *J. Biol. Chem.* **1982**, *257* (19), 11443–11447.

(6) Cooper, W. J.; Zika, R. G. Photochemical Formation of Hydrogen Peroxide in Surface and Ground Waters Exposed to Sunlight. *Science* **1983**, *220* (4598), 711–712. https://doi.org/10.1126/science.220.4598.711.

(7) Petasne, R.; Zika, R. G. Fate of Superoxide in Coastal Sea Water. *Nature* **1987**, *325*, 516–518.

(8) Perdue, E. M.; Ritchie, J. D. 5.10 - Dissolved Organic Matter in Freshwaters. In *Treatise on Geochemistry*; Holland, H. D., Turekian, K. K., Eds.; Pergamon: Oxford, 2003; pp 273–318. https://doi.org/10.1016/B0-08-043751-6/05080-5.

(9) Sharpless, C. M.; Blough, N. V. The Importance of Charge-Transfer Interactions in Determining Chromophoric Dissolved Organic Matter (CDOM) Optical and Photochemical Properties. *Env. Sci Process. Impacts* **2014**, *16* (4), 654–671. https://doi.org/10.1039/C3EM00573A.

(10) Ridgwell, A.; Arndt, S. Chapter 1 - Why Dissolved Organics Matter: DOC in Ancient Oceans and Past Climate Change A2 - Hansell, Dennis A. In *Biogeochemistry of Marine Dissolved Organic Matter (Second Edition)*; Carlson, C. A., Ed.; Academic Press: Boston, 2015; pp 1–20. https://doi.org/10.1016/B978-0-12-405940-5.00001-7.

(11) Artifon, V.; Zanardi-Lamardo, E.; Fillmann, G. Aquatic Organic Matter: Classification and Interaction with Organic Microcontaminants. *Sci. Total Environ.* **2019**, *649*, 1620–1635. https://doi.org/10.1016/j.scitotenv.2018.08.385.

(12) McKay, G. Emerging Investigator Series: Critical Review of Photophysical Models for the Optical and Photochemical Properties of Dissolved Organic Matter. *Environ. Sci. Process. Impacts* **2020**, *22* (5), 1139–1165. https://doi.org/10.1039/D0EM00056F.

(13) Carlson, C. A.; Hansell, D. A. Chapter 3 - DOM Sources, Sinks, Reactivity, and Budgets. In *Biogeochemistry of Marine Dissolved Organic Matter (Second Edition)*; Academic Press: Boston, 2015; pp 65–126. https://doi.org/10.1016/B978-0-12-405940-5.00003-0.

(14) Mostofa, K.; Liu, C.-Q.; Mottaleb, M. A.; Wan, G.; Ogawa, H.; Vione, D.; Yoshioka, T.; Wu, F. Dissolved Organic Matter in Natural Waters. In *Environmental Science and Engineering (Subseries: Environmental Science)*; 2013; pp 1–137. https://doi.org/10.1007/978-3-642-32223-5_1.

(15) Sharpless, C. M.; Blough, N. V. The Importance of Charge-Transfer Interactions in Determining Chromophoric Dissolved Organic Matter (CDOM) Optical and Photochemical Properties. *Environ. Sci. Process. Impacts* **2014**, *16* (4), 654. https://doi.org/10.1039/c3em00573a.

(16) What Are Humic Substances | IHSS.
(17) Choudhry, G. G. Humic Substances: Part Structural Aspects. *Toxicol. Environ. Chem.* **1981**, *4* (3–4), 209–260. https://doi.org/10.1080/02772248109356963.
(18) Mopper, K.; Stubbins, A.; Ritchie, J. D.; Bialk, H. M.; Hatcher, P. G. Advanced Instrumental Approaches for Characterization of Marine Dissolved Organic Matter: Extraction Techniques, Mass Spectrometry, and Nuclear Magnetic Resonance Spectroscopy. *Chem. Rev.* **2007**, *107* (2), 419–442. https://doi.org/10.1021/cr050359b.
(19) Perdue, E. M.; Hertkorn, N.; Kettrup, A. Substitution Patterns in Aromatic Rings by Increment Analysis. Model Development and Application to Natural Organic Matter. *Anal. Chem.* **2007**, *79* (3), 1010–1021. https://doi.org/10.1021/ac061611y.
(20) Sulzberger, B.; Durisch-Kaiser, E. Chemical Characterization of Dissolved Organic Matter (DOM): A Prerequisite for Understanding UV-Induced Changes of DOM Absorption Properties and Bioavailability. *Aquat. Sci.* **2009**, *71* (2), 104–126. https://doi.org/10.1007/s00027-008-8082-5.
(21) Nebbioso, A.; Piccolo, A. Molecular Characterization of Dissolved Organic Matter (DOM): A Critical Review. *Anal. Bioanal. Chem.* **2013**, *405* (1), 109–124. https://doi.org/10.1007/s00216-012-6363-2.
(22) Hertkorn, N.; Harir, M.; Koch, B. P.; Michalke, B.; Schmitt-Kopplin, P. High-Field NMR Spectroscopy and FTICR Mass Spectrometry: Powerful Discovery Tools for the Molecular Level Characterization of Marine Dissolved Organic Matter. *Biogeosciences* **2013**, *10* (3), 1583–1624. https://doi.org/10.5194/bg-10-1583-2013.
(23) Minor, E. C.; Swenson, M. M.; Mattson, B. M.; Oyler, A. R. Structural Characterization of Dissolved Organic Matter: A Review of Current Techniques for Isolation and Analysis. *Environ. Sci. Process. Impacts* **2014**, *16* (9), 2064–2079. https://doi.org/10.1039/C4EM00062E.
(24) Kujawinski, E. B.; Hatcher, P. G.; Freitas, M. A. High-Resolution Fourier Transform Ion Cyclotron Resonance Mass Spectrometry of Humic and Fulvic Acids: Improvements and Comparisons. *Anal. Chem.* **2002**, *74* (2), 413–419. https://doi.org/10.1021/ac0108313.
(25) Kujawinski, E. B.; Freitas, M. A.; Zang, X.; Hatcher, P. G.; Green-Church, K. B.; Jones, R. B. The Application of Electrospray Ionization Mass Spectrometry (ESI MS) to the Structural Characterization of Natural Organic Matter. *Org. Geochem.* **2002**, *33* (3), 171–180. https://doi.org/10.1016/S0146-6380(01)00149-8.
(26) Stenson, A. C.; Landing, W. M.; Marshall, A. G.; Cooper, W. T. Ionization and Fragmentation of Humic Substances in Electrospray Ionization Fourier Transform-Ion Cyclotron Resonance Mass Spectrometry. *Anal. Chem.* **2002**, *74* (17), 4397–4409. https://doi.org/10.1021/ac020019f.
(27) Stenson, A. C.; Marshall, A. G.; Cooper, W. T. Exact Masses and Chemical Formulas of Individual Suwannee River Fulvic Acids from Ultrahigh Resolution Electrospray Ionization Fourier Transform Ion Cyclotron Resonance Mass Spectra. *Anal. Chem.* **2003**, *75* (6), 1275–1284. https://doi.org/10.1021/ac026106p.
(28) Ohno, T.; Sleighter, R. L.; Hatcher, P. G. Comparative Study of Organic Matter Chemical Characterization Using Negative and Positive Mode Electrospray Ionization Ultrahigh-Resolution Mass Spectrometry. *Anal. Bioanal. Chem.* **2016**, *408* (10), 2497–2504. https://doi.org/10.1007/s00216-016-9346-x.
(29) Baluha, D. R.; Blough, N. V.; Del Vecchio, R. Selective Mass Labeling for Linking the Optical Properties of Chromophoric Dissolved Organic Matter to Structure and

Composition via Ultrahigh Resolution Electrospray Ionization Mass Spectrometry. *Environ. Sci. Technol.* **2013**, *47* (17), 9891–9897. https://doi.org/10.1021/es402400j.
(30) Bianca, M. R.; Baluha, D. R.; Gonsior, M.; Schmitt-Kopplin, P.; Del Vecchio, R.; Blough, N. V. Contribution of Ketone/Aldehyde-Containing Compounds to the Composition and Optical Properties of Suwannee River Fulvic Acid Revealed by Ultrahigh Resolution Mass Spectrometry and Deuterium Labeling. *Anal. Bioanal. Chem.* **2020**, *412* (6), 1441–1451. https://doi.org/10.1007/s00216-019-02377-x.
(31) Hertkorn, N.; Benner, R.; Frommberger, M.; Schmitt-Kopplin, P.; Witt, M.; Kaiser, K.; Kettrup, A.; Hedges, J. I. Characterization of a Major Refractory Component of Marine Dissolved Organic Matter. *Geochim. Cosmochim. Acta* **2006**, *70* (12), 2990–3010. https://doi.org/10.1016/j.gca.2006.03.021.
(32) Kim, S.; Simpson, A. J.; Kujawinski, E. B.; Freitas, M. A.; Hatcher, P. G. High Resolution Electrospray Ionization Mass Spectrometry and 2D Solution NMR for the Analysis of DOM Extracted by C18 Solid Phase Disk. *Org. Geochem.* **2003**, *34* (9), 1325–1335. https://doi.org/10.1016/S0146-6380(03)00101-3.
(33) Wagner, S.; Jaffé, R.; Cawley, K.; Dittmar, T.; Stubbins, A. Associations Between the Molecular and Optical Properties of Dissolved Organic Matter in the Florida Everglades, a Model Coastal Wetland System. *Front. Chem.* **2015**, *3*. https://doi.org/10.3389/fchem.2015.00066.
(34) Hertkorn, N.; Harir, M.; Cawley, K. M.; Schmitt-Kopplin, P.; Jaffé, R. Molecular Characterization of Dissolved Organic Matter from Subtropical Wetlands: A Comparative Study through the Analysis of Optical Properties, NMR and FTICR/MS. *Biogeosciences* **2016**, *13* (8), 2257–2277. https://doi.org/10.5194/bg-13-2257-2016.
(35) Woods, G. C.; Simpson, M. J.; Koerner, P. J.; Napoli, A.; Simpson, A. J. HILIC-NMR: Toward the Identification of Individual Molecular Components in Dissolved Organic Matter. *Environ. Sci. Technol.* **2011**, *45* (9), 3880–3886. https://doi.org/10.1021/es103425s.
(36) Zherebker, A.; Shirshin, E.; Rubekina, A.; Kharybin, O.; Kononikhin, A.; Kulikova, N. A.; Zaitsev, K. V.; Roznyatovsky, V. A.; Grishin, Y. K.; Perminova, I. V.; Nikolaev, E. N. Optical Properties of Soil Dissolved Organic Matter Are Related to Acidic Functions of Its Components as Revealed by Fractionation, Selective Deuteromethylation, and Ultrahigh Resolution Mass Spectrometry. *Environ. Sci. Technol.* **2020**, *54* (5), 2667–2677. https://doi.org/10.1021/acs.est.9b05298.
(37) Hawkes, J. A.; Patriarca, C.; Sjöberg, P. J. R.; Tranvik, L. J.; Bergquist, J. Extreme Isomeric Complexity of Dissolved Organic Matter Found across Aquatic Environments. *Limnol. Oceanogr. Lett.* **2018**, *3* (2), 21–30. https://doi.org/10.1002/lol2.10064.
(38) Zark, M.; Christoffers, J.; Dittmar, T. Molecular Properties of Deep-Sea Dissolved Organic Matter Are Predictable by the Central Limit Theorem: Evidence from Tandem FT-ICR-MS. *Mar. Chem.* **2017**, *191*, 9–15. https://doi.org/10.1016/j.marchem.2017.02.005.
(39) Mannino, A.; Novak, M. G.; Nelson, N. B.; Belz, M.; Berthon, F.; Blough, N. V.; Boss, E.; Bricaud, A.; Castillo, C. D.; Vecchio, R. D.; D'Sa, E. J.; Matsuoka, A.; Miller, R. L.; Neeley, A.; Tzortziou, M.; Werdell, J. Measurement Protocol of Absorption by Chromophoric Dissolved Organic Matter (CDOM) and Other Dissolved Materials. **2019**.

(40) Bricaud, A.; Morel, A.; Prieur, L. Absorption by Dissolved Organic Matter of the Sea (Yellow Substance) in the UV and Visible Domains1. *Limnol. Oceanogr.* **1981**, *26* (1), 43–53. https://doi.org/10.4319/lo.1981.26.1.0043.
(41) Twardowski, M. S.; Boss, E.; Sullivan, J. M.; Donaghay, P. L. Modeling the Spectral Shape of Absorption by Chromophoric Dissolved Organic Matter. *Mar. Chem.* **2004**, *89* (1), 69–88. https://doi.org/10.1016/j.marchem.2004.02.008.
(42) D'Sa, E. J.; Steward, R. G.; Vodacek, A.; Blough, N. V.; Phinney, D. Determining Optical Absorption of Colored Dissolved Organic Matter in Seawater with a Liquid Capillary Waveguide. *Limnol. Oceanogr.* **1999**, *44* (4), 1142–1148. https://doi.org/10.4319/lo.1999.44.4.1142.
(43) Nelson, N. B.; Siegel, D. A.; Carlson, Craig. A.; Swan, C.; Smethie, W. M.; Khatiwala, S. Hydrography of Chromophoric Dissolved Organic Matter in the North Atlantic. *Deep Sea Res. Part Oceanogr. Res. Pap.* **2007**, *54* (5), 710–731. https://doi.org/10.1016/j.dsr.2007.02.006.
(44) Cartisano, C.; Del Vecchio, R.; Blough, N. A Calibration/Validation Protocol for Long/Multi-Pathlength Capillary Waveguide Spectrometers: Protocols for Capillary Waveguide. *Limnol. Oceanogr. Methods* **2018**, *16* (11), 773–786. https://doi.org/10.1002/lom3.10282.
(45) Coble, P. G. Characterization of Marine and Terrestrial DOM in Seawater Using Excitation-Emission Matrix Spectroscopy. *Mar. Chem.* **1996**, *51* (4), 325–346. https://doi.org/10.1016/0304-4203(95)00062-3.
(46) Coelho, C.; Guyot, G. Chapter 6:Excitation–Emission Matrices of Fluorescence – EEMF – for the Characterization of Organic Matter of Surface Waters. In *Surface Water Photochemistry*; 2015; pp 97–115. https://doi.org/10.1039/9781782622154-00097.
(47) Del Vecchio, R.; Blough, N. V. Spatial and Seasonal Distribution of Chromophoric Dissolved Organic Matter and Dissolved Organic Carbon in the Middle Atlantic Bight. *Mar. Chem.* **2004**, *89* (1), 169–187. https://doi.org/10.1016/j.marchem.2004.02.027.
(48) Andrew, A. A.; Del Vecchio, R.; Subramaniam, A.; Blough, N. V. Chromophoric Dissolved Organic Matter (CDOM) in the Equatorial Atlantic Ocean: Optical Properties and Their Relation to CDOM Structure and Source. *Mar. Chem.* **2013**, *148*, 33–43. https://doi.org/10.1016/j.marchem.2012.11.001.
(49) Cartisano, C. M.; Del Vecchio, R.; Bianca, M. R.; Blough, N. V. Investigating the Sources and Structure of Chromophoric Dissolved Organic Matter (CDOM) in the North Pacific Ocean (NPO) Utilizing Optical Spectroscopy Combined with Solid Phase Extraction and Borohydride Reduction. *Mar. Chem.* **2018**, *204*, 20–35. https://doi.org/10.1016/j.marchem.2018.05.005.
(50) Boyle, E. S.; Guerriero, N.; Thiallet, A.; Vecchio, R. D.; Blough, N. V. Optical Properties of Humic Substances and CDOM: Relation to Structure. *Environ. Sci. Technol.* **2009**, *43* (7), 2262–2268. https://doi.org/10.1021/es803264g.
(51) Chen, Y.; Liu, J.; Zhang, X.; Blough, N. V. Time-Resolved Fluorescence Spectra of Untreated and Sodium Borohydride-Reduced Chromophoric Dissolved Organic Matter. *Environ. Sci. Technol.* **2020**, *54* (19), 12109–12118. https://doi.org/10.1021/acs.est.0c03135.
(52) Del Vecchio, R.; Blough, N. V. On the Origin of the Optical Properties of Humic Substances. *Environ. Sci. Technol.* **2004**, *38* (14), 3885–3891. https://doi.org/10.1021/es049912h.

(53) Ma, J.; Del Vecchio, R.; Golanoski, K. S.; Boyle, E. S.; Blough, N. V. Optical Properties of Humic Substances and CDOM: Effects of Borohydride Reduction. *Environ. Sci. Technol.* **2010**, *44* (14), 5395–5402. https://doi.org/10.1021/es100880q.
(54) Perminova, I. V.; Shirshin, E. A.; Konstantinov, A. I.; Zherebker, A. Ya.; Dubinenkov, I. V.; Lebedev, V. A.; Kulikova, N. A.; Nikolaev, E. N.; Bulygina, E.; Holmes, R. M. The Structural Arrangement and Relative Abundance of Aliphatic Units May Effect Long-Wave Absorbance of Natural Organic Matter as Revealed by 1H NMR Spectroscopy. *Environ. Sci. Technol.* **2018**. https://doi.org/10.1021/acs.est.8b01029.
(55) Yakimov, B. P.; Rubekina, A. A.; Budylin, G. S.; Zherebker, A. Y.; Kompanets, V. O.; Chekalin, S. V.; Vainer, Y. G.; Fadeev, V. V.; Gorbunov, M. Y.; Perminova, I. V.; Shirshin, E. A. Ultrafast Energy Transfer Determines the Formation of Fluorescence in DOM and Humic Substances. *Environ. Sci. Technol.* **2021**, *55* (15), 10365–10377. https://doi.org/10.1021/acs.est.1c00998.
(56) Nelson, N. B.; Siegel, D. A. The Global Distribution and Dynamics of Chromophoric Dissolved Organic Matter. *Annu. Rev. Mar. Sci.* **2013**, *5* (1), 447–476. https://doi.org/10.1146/annurev-marine-120710-100751.
(57) Zika, R. G. Chapter 10 Marine Organic Photochemistry. In *Elsevier Oceanography Series*; Duursma, E. K., Dawson, R., Eds.; Marine Organic Chemistry; Elsevier, 1981; Vol. 31, pp 299–325. https://doi.org/10.1016/S0422-9894(08)70332-5.
(58) Zafiriou, O. C.; Joussot-Dubien, J.; Zepp, R. G.; Zika, R. G. Photochemistry of Natural Waters. *Environ. Sci. Technol.* **1984**, *18* (12), 358A-371A. https://doi.org/10.1021/es00130a001.
(59) Zika, R. G. Advances in Marine Photochemistry 1983–1987. *Rev. Geophys.* **1987**, *25* (6), 1390–1394. https://doi.org/10.1029/RG025i006p01390.
(60) Zepp, R. Environmental Photoprocesses Involving Natural Organic Matter. In *Humic Substance and their Role in the Environment*; Wiley: New York, 1988; pp 192–214.
(61) Cooper, W. J.; Zika, R. G.; Petasne, R. G.; Plane, J. M. C. Photochemical Formation of Hydrogen Peroxide in Natural Waters Exposed to Sunlight. *Environ. Sci. Technol.* **1988**, *22* (10), 1156–1160. https://doi.org/10.1021/es00175a004.
(62) Hoigné, J.; Faust, B. C.; Haag, W. R.; Scully, F. E.; Zepp, R. G. Aquatic Humic Substances as Sources and Sinks of Photochemically Produced Transient Reactants. In *Aquatic Humic Substances*; Advances in Chemistry; American Chemical Society, 1988; Vol. 219, pp 363–381. https://doi.org/10.1021/ba-1988-0219.ch023.
(63) Blough, N. V.; Zepp, R. G. Reactive Oxygen Species in Natural Waters. In *Active Oxygen in Chemistry*; Foote, C. S., Ed.; Chapman & Hall, 1995; p 54.
(64) Kieber, D. J.; Peake, B. M.; Scully, N. M. Reactive Oxygen Species in Aquatic Ecosystems. In *UV Effects in Aquatic Organisms and Ecosystems*; Helbling, E. W., Zagarese, H., Eds.; The Royal Society of Chemistry: Thomas Graham House, Science Park, Milton Road, Cambridge CB4 0WF, UK, 2003; Vol. 1.
(65) Burns, J. M.; Cooper, W. J.; Ferry, J. L.; King, D. W.; DiMento, B. P.; McNeill, K.; Miller, C. J.; Miller, W. L.; Peake, B. M.; Rusak, S. A.; Rose, A. L.; Waite, T. D. Methods for Reactive Oxygen Species (ROS) Detection in Aqueous Environments. *Aquat. Sci.* **2012**, *74* (4), 683–734. https://doi.org/10.1007/s00027-012-0251-x.
(66) Swallow, A. J. Hydrated Electrons in Seawater. *Nature* **1969**, *222* (5191), 369–370. https://doi.org/10.1038/222369a0.

(67) Fischer, A. M.; Kliger, D. S.; Winterle, J. S.; Mill, T. Direct Observation of Phototransients in Natural Waters. *Chemosphere* **1985**, *14* (9), 1299–1306. https://doi.org/10.1016/0045-6535(85)90150-X.
(68) Fischer, A. M.; Winterle, J. S.; Mill, T. Primary Photochemical Processes in Photolysis Mediated by Humic Substances. In *Photochemistry of Environmental Aquatic Systems*; ACS Symposium Series; American Chemical Society, 1987; Vol. 327, pp 141–156. https://doi.org/10.1021/bk-1987-0327.ch011.
(69) Power, J. F.; Sharma, D. K.; Langford, C. H.; Bonneau, R.; Joussot-Dubien, J. Photophysics of a Well Characterized Humic Substance. *Photochem. Photobiol.* **1986**, *44* (1), 11–13. https://doi.org/10.1111/j.1751-1097.1986.tb03557.x.
(70) Power, J. F.; Sharma, D. K.; Langford, C. H.; Bonneau, R.; Joussot-Dubien, J. Laser Flash Photolytic Studies of a Well-Characterized Soil Humic Substance. In *Photochemistry of Environmental Aquatic Systems*; Zika, R. G., Cooper, W. J., Eds.; ACS Symposium Series; American Chemical Society: Washington, DC, 1987; Vol. 327, pp 157–173. https://doi.org/10.1021/bk-1987-0327.ch012.
(71) Zepp, R. G.; Braun, A. M.; Hoigne, Juerg.; Leenheer, J. A. Photoproduction of Hydrated Electrons from Natural Organic Solutes in Aquatic Environments. *Environ. Sci. Technol.* **1987**, *21* (5), 485–490. https://doi.org/10.1021/es00159a010.
(72) Thomas-Smith, T. E.; Blough, N. V. Photoproduction of Hydrated Electron from Constituents of Natural Waters. *Environ. Sci. Technol.* **2001**, *35* (13), 2721–2726. https://doi.org/10.1021/es010552x.
(73) Breugem, P.; van Noort, P.; Velberg, S.; Wondergem, E.; Zijlstra, J. Steady State Concentrations of the Phototransient Hydrated Electron in Natural Waters. *Chemosphere* **1986**, *15* (6), 717–724. https://doi.org/10.1016/0045-6535(86)90037-8.
(74) Cory, R. M.; McNeill, K.; Cotner, J. P.; Amado, A.; Purcell, J. M.; Marshall, A. G. Singlet Oxygen in the Coupled Photochemical and Biochemical Oxidation of Dissolved Organic Matter. *Environ. Sci. Technol.* **2010**, *44* (10), 3683–3689. https://doi.org/10.1021/es902989y.
(75) Cooper, W. J.; Shao, C.; Lean, D. R. S.; Gordon, A. S.; Scully, F. E. Factors Affecting the Distribution of H2O2 in Surface Waters. In *Environmental Chemistry of Lakes and Reservoirs*; Advances in Chemistry; American Chemical Society, 1994; Vol. 237, pp 391–422. https://doi.org/10.1021/ba-1994-0237.ch012.
(76) Dalrymple, R. M.; Carfagno, A. K.; Sharpless, C. M. Correlations between Dissolved Organic Matter Optical Properties and Quantum Yields of Singlet Oxygen and Hydrogen Peroxide. *Environ. Sci. Technol.* **2010**, *44* (15), 5824–5829. https://doi.org/10.1021/es101005u.
(77) Garg, S.; Rose, A. L.; Waite, T. D. Photochemical Production of Superoxide and Hydrogen Peroxide from Natural Organic Matter. *Geochim. Cosmochim. Acta* **2011**, *75* (15), 4310–4320. https://doi.org/10.1016/j.gca.2011.05.014.
(78) Zhang, Y.; Del Vecchio, R.; Blough, N. V. Investigating the Mechanism of Hydrogen Peroxide Photoproduction by Humic Substances. *Environ. Sci. Technol.* **2012**, *46* (21), 11836–11843. https://doi.org/10.1021/es3029582.
(79) Schendorf, T. M.; Del Vecchio, R.; Koech, K.; Blough, N. V. A Standard Protocol for $NaBH_4$ Reduction of CDOM and HS: Borohydride Reduction of HS and CDOM. *Limnol. Oceanogr. Methods* **2016**, *14* (6), 414–423. https://doi.org/10.1002/lom3.10100.

(80) Zhang, Y.; Blough, N. V. Photoproduction of One-Electron Reducing Intermediates by Chromophoric Dissolved Organic Matter (CDOM): Relation to O_2^- and H_2O_2 Photoproduction and CDOM Photooxidation. *Environ. Sci. Technol.* **2016**, *50* (20), 11008–11015. https://doi.org/10.1021/acs.est.6b02919.
(81) Bielski, B. H. J.; Allen, A. O. Mechanism of the Disproportionation of Superoxide Radicals. *J. Phys. Chem.* **1977**, *81* (11), 1048–1050. https://doi.org/10.1021/j100526a005.
(82) Baxendale, J. H. The Flash Photolysis of Water and Aqueous Solutions. *Radiat. Res.* **1962**, *17* (3), 312–326. https://doi.org/10.2307/3571095.
(83) Rabani, J.; Neilsen, S. Absorption Spectrum and Decay Kinetics of O2- and HO2 in Aqueous Solutions by Pulse Radiolysis. *J. Phys. Chem.* **1969**, *73* (11), 3736–3744.
(84) Bielski, B. H. J.; Cabelli, D. E.; Arudi, R. L.; Ross, A. B. Reactivity of HO2/O−2 Radicals in Aqueous Solution. *J. Phys. Chem. Ref. Data* **1985**, *14* (4), 1041–1100. https://doi.org/10.1063/1.555739.
(85) Zafiriou, O. C. Chemistry of Superoxide Ion-Radical (O2−) in Seawater. I. PKasw∗ (HOO) and Uncatalyzed Dismutation Kinetics Studied by Pulse Radiolysis. *Mar. Chem.* **1990**, *30*, 31–43. https://doi.org/10.1016/0304-4203(90)90060-P.
(86) Zhang, Y.; Blough, N. V. Photoproduction of One-Electron Reducing Intermediates by Chromophoric Dissolved Organic Matter (CDOM): Relation to O_2^- and H_2O_2 Photoproduction and CDOM Photooxidation. *Environ. Sci. Technol.* **2016**, *50* (20), 11008–11015. https://doi.org/10.1021/acs.est.6b02919.
(87) Powers, L. C.; Miller, W. L. Apparent Quantum Efficiency Spectra for Superoxide Photoproduction and Its Formation of Hydrogen Peroxide in Natural Waters. *Front. Mar. Sci.* **2016**, *3*. https://doi.org/10.3389/fmars.2016.00235.
(88) C. Powers, L.; L. Miller, W. Blending Remote Sensing Data Products to Estimate Photochemical Production of Hydrogen Peroxide and Superoxide in the Surface Ocean. *Environ. Sci. Process. Impacts* **2014**, *16* (4), 792–806. https://doi.org/10.1039/C3EM00617D.
(89) Shaked, Y.; Harris, R.; Klein-Kedem, N. Hydrogen Peroxide Photocycling in the Gulf of Aqaba, Red Sea. *Environ. Sci. Technol.* **2010**, *44* (9), 3238–3244. https://doi.org/10.1021/es902343y.
(90) Mopper, K.; Kieber, D. J.; Stubbins, A. Chapter 8 - Marine Photochemistry of Organic Matter: Processes and Impacts A2 - Hansell, Dennis A. In *Biogeochemistry of Marine Dissolved Organic Matter (Second Edition)*; Carlson, C. A., Ed.; Academic Press: Boston, 2015; pp 389–450. https://doi.org/10.1016/B978-0-12-405940-5.00008-X.
(91) Obernosterer, I.; Ruardij, P.; Herndl, G. J. Spatial and Diurnal Dynamics of Dissolved Organic Matter (DOM) Fluorescence and H2O2 and the Photochemical Oxygen Demand of Surface Water DOM across the Subtropical Atlantic Ocean. *Limnol. Oceanogr.* **2001**, *46* (3), 632–643. https://doi.org/10.4319/lo.2001.46.3.0632.
(92) Yuan, J.; Shiller, A. M. Distribution of Hydrogen Peroxide in the Northwest Pacific Ocean. *Geochem. Geophys. Geosystems* **2005**, *6* (9). https://doi.org/10.1029/2004GC000908.
(93) Cooper, W. J.; Lean, D. R. S. Hydrogen Peroxide Concentration in a Northern Lake: Photochemical Formation and Diel Variability. *Environ. Sci. Technol.* **1989**, *23* (11), 1425–1428. https://doi.org/10.1021/es00069a017.
(94) Avery, G. B.; Cooper, W. J.; Kieber, R. J.; Willey, J. D. Hydrogen Peroxide at the Bermuda Atlantic Time Series Station: Temporal Variability of Seawater Hydrogen

Peroxide. *Mar. Chem.* **2005**, *97* (3), 236–244. https://doi.org/10.1016/j.marchem.2005.03.006.
(95) Rusak, S. A.; Peake, B. M.; Richard, L. E.; Nodder, S. D.; Cooper, W. J. Distributions of Hydrogen Peroxide and Superoxide in Seawater East of New Zealand. *Mar. Chem.* **2011**, *127* (1–4), 155–169. https://doi.org/10.1016/j.marchem.2011.08.005.
(96) Szymczak, R.; Waite, T. Generation and Decay of Hydrogen Peroxide in Estuarine Waters. *Mar. Freshw. Res.* **1988**, *39* (3), 289. https://doi.org/10.1071/MF9880289.
(97) Zika, R. G.; Moffett, J. W.; Petasne, R. G.; Cooper, W. J.; Saltzman, E. S. Spatial and Temporal Variations of Hydrogen Peroxide in Gulf of Mexico Waters. *Geochim. Cosmochim. Acta* **1985**, *49* (5), 1173–1184. https://doi.org/10.1016/0016-7037(85)90008-0.
(98) Petasne, R. G.; Zika, R. G. Hydrogen Peroxide Lifetimes in South Florida Coastal and Offshore Waters. *Mar. Chem.* **1997**, *56* (3), 215–225. https://doi.org/10.1016/S0304-4203(96)00072-2.
(99) Yuan, J.; Shiller, A. M. The Distribution of Hydrogen Peroxide in the Southern and Central Atlantic Ocean. *Deep Sea Res. Part II Top. Stud. Oceanogr.* **2001**, *48* (13), 2947–2970. https://doi.org/10.1016/S0967-0645(01)00026-1.
(100) Gerringa, L. J. A.; Rijkenberg, M. J. A.; Timmermans, R.; Buma, A. G. J. The Influence of Solar Ultraviolet Radiation on the Photochemical Production of H2O2 in the Equatorial Atlantic Ocean. *J. Sea Res.* **2004**, *51* (1), 3–10. https://doi.org/10.1016/j.seares.2003.03.002.
(101) Häkkinen, P. J.; Anesio, A. M.; Granéli, W. Hydrogen Peroxide Distribution, Production, and Decay in Boreal Lakes. *Can. J. Fish. Aquat. Sci.* **2004**, *61* (8), 1520–1527. https://doi.org/10.1139/f04-098.
(102) Rose, A. L.; Webb, E. A.; Waite, T. D.; Moffett, J. W. Measurement and Implications of Nonphotochemically Generated Superoxide in the Equatorial Pacific Ocean. *Environ. Sci. Technol.* **2008**, *42* (7), 2387–2393. https://doi.org/10.1021/es7024609.
(103) Yuan, J.; Shiller, A. M. The Variation of Hydrogen Peroxide in Rainwater over the South and Central Atlantic Ocean. *Atmos. Environ.* **2000**, *34* (23), 3973–3980. https://doi.org/10.1016/S1352-2310(00)00167-9.
(104) Kieber, D. J.; Miller, G. W.; Neale, P. J.; Mopper, K. Wavelength and Temperature-Dependent Apparent Quantum Yields for Photochemical Formation of Hydrogen Peroxide in Seawater. *Env. Sci Process. Impacts* **2014**, *16* (4), 777–791. https://doi.org/10.1039/C4EM00036F.
(105) Moore, C. A.; Farmer, C. T.; Zika, R. G. Influence of the Orinoco River on Hydrogen Peroxide Distribution and Production in the Eastern Caribbean. *J. Geophys. Res. Oceans* **1993**, *98* (C2), 2289–2298. https://doi.org/10.1029/92JC02767.
(106) Yocis, B. H.; Kieber, D. J.; Mopper, K. Photochemical Production of Hydrogen Peroxide in Antarctic Waters. *Deep Sea Res. Part Oceanogr. Res. Pap.* **2000**, *47* (6), 1077–1099. https://doi.org/10.1016/S0967-0637(99)00095-3.
(107) Johnson, K. S.; Willason, S. W.; Wiesenburg, D. A.; Lohrenz, S. E.; Arnone, R. A. Hydrogen Peroxide in the Western Mediterranean Sea: A Tracer for Vertical Advection. *Deep Sea Res. Part Oceanogr. Res. Pap.* **1989**, *36* (2), 241–254. https://doi.org/10.1016/0198-0149(89)90136-2.

(108) Cooper, W. J.; Saltzman, E. S.; Zika, R. G. The Contribution of Rainwater to Variability in Surface Ocean Hydrogen Peroxide. *J. Geophys. Res.* **1987**, *92* (C3), 2970. https://doi.org/10.1029/JC092iC03p02970.
(109) Palenik, B.; Morel, F. M. M. Dark Production of H2O2 in the Sargasso Sea. *Limnol. Oceanogr.* **1988**, *33* (6part2), 1606–1611. https://doi.org/10.4319/lo.1988.33.6part2.1606.
(110) Yuan, J.; Shiller, A. M. Hydrogen Peroxide in Deep Waters of the North Pacific Ocean. *Geophys. Res. Lett.* **2004**, *31* (1). https://doi.org/10.1029/2003GL018439.
(111) Paul Hansard, S.; Vermilyea, A. W.; Voelker, B. M. Measurements of Superoxide Radical Concentration and Decay Kinetics in the Gulf of Alaska. *Deep Sea Res. Part Oceanogr. Res. Pap.* **2010**, *57* (9), 1111–1119. https://doi.org/10.1016/j.dsr.2010.05.007.
(112) Diaz, J. M.; Hansel, C. M.; Voelker, B. M.; Mendes, C. M.; Andeer, P. F.; Zhang, T. Widespread Production of Extracellular Superoxide by Heterotrophic Bacteria. *Science* **2013**, *340* (6137), 1223–1226. https://doi.org/10.1126/science.1237331.
(113) Voelker, B. M.; Sedlak, D. L.; Zafiriou, O. C. Chemistry of Superoxide Radical in Seawater: Reactions with Organic Cu Complexes. *Environ. Sci. Technol.* **2000**, *34* (6), 1036–1042. https://doi.org/10.1021/es990545x.
(114) Barbeau, K. Photochemistry of Organic Iron(III) Complexing Ligands in Oceanic Systems. *Photochem. Photobiol.* **2006**, *82* (6), 1505–1516. https://doi.org/10.1111/j.1751-1097.2006.tb09806.x.
(115) Sunda, W. G. Measurement of Manganese, Zinc and Cadmium Complexation in Seawater Using Chelex Ion Exchange Equilibria. *Mar. Chem.* **1984**, *14* (4), 365–378. https://doi.org/10.1016/0304-4203(84)90031-8.
(116) Garg, S.; Rose, A. L.; Waite, T. D. Pathways Contributing to the Formation and Decay of Ferrous Iron in Sunlit Natural Waters. In *Aquatic Redox Chemistry*; Tratnyek, P. G., Grundl, T. J., Haderlein, S. B., Eds.; American Chemical Society: Washington, DC, 2011; Vol. 1071, pp 153–176. https://doi.org/10.1021/bk-2011-1071.ch008.
(117) Yuan, X.; Pham, A. N.; Xing, G.; Rose, A. L.; Waite, T. D. Effects of PH, Chloride, and Bicarbonate on Cu(I) Oxidation Kinetics at Circumneutral PH. *Environ. Sci. Technol.* **2012**, *46* (3), 1527–1535. https://doi.org/10.1021/es203394k.
(118) von Langen, P. J.; Johnson, K. S.; Coale, K. H.; Elrod, V. A. Oxidation Kinetics of Manganese (II) in Seawater at Nanomolar Concentrations. *Geochim. Cosmochim. Acta* **1997**, *61* (23), 4945–4954. https://doi.org/10.1016/S0016-7037(97)00355-4.
(119) Xing, G.; Garg, S.; Miller, C. J.; Pham, A. N.; Waite, T. D. Effect of Chloride and Suwannee River Fulvic Acid on Cu Speciation: Implications to Cu Redox Transformations in Simulated Natural Waters. *Environ. Sci. Technol.* **2020**, *54* (4), 2334–2343. https://doi.org/10.1021/acs.est.9b06789.
(120) Moffett, J. W.; Zika, R. G. Reaction Kinetics of Hydrogen Peroxide with Copper and Iron in Seawater. *Environ. Sci. Technol.* **1987**, *21* (8), 804–810. https://doi.org/10.1021/es00162a012.
(121) Zepp, R. G.; Faust, B. C.; Hoigne, J. Hydroxyl Radical Formation in Aqueous Reactions (PH 3-8) of Iron(II) with Hydrogen Peroxide: The Photo-Fenton Reaction. *Environ. Sci. Technol.* **1992**, *26* (2), 313–319. https://doi.org/10.1021/es00026a011.
(122) White, E. M.; Vaughan, P. P.; Zepp, R. G. Role of the Photo-Fenton Reaction in the Production of Hydroxyl Radicals and Photobleaching of Colored Dissolved Organic Matter in a Coastal River of the Southeastern United States. *Aquat. Sci.* **2003**, *65* (4), 402–414. https://doi.org/10.1007/s00027-003-0675-4.

(123) Southworth, B. A.; Voelker, B. M. Hydroxyl Radical Production via the Photo-Fenton Reaction in the Presence of Fulvic Acid. *Environ. Sci. Technol.* **2003**, *37* (6), 1130–1136. https://doi.org/10.1021/es020757l.
(124) Mostofa, K.; Liu, C.-Q.; Sakugawa, H.; Vione, D.; Minakata, D.; Saquib, M.; Mottaleb, M. A. Photoinduced Generation of Hydroxyl Radical in Natural Waters. In *Photobiogeochemistry of Organic Matter: Principles and Practices in Natural Waters*; 2013; pp 209–272. https://doi.org/10.1007/978-3-642-32223-5_3.
(125) Moffett, J. W.; Zika, R. G. Measurement of Copper(I) in Surface Waters of the Subtropical Atlantic and Gulf of Mexico. *Geochim. Cosmochim. Acta* **1988**, *52* (7), 1849–1857. https://doi.org/10.1016/0016-7037(88)90008-7.
(126) Heller, M. I.; Croot, P. L. Superoxide Decay Kinetics in the Southern Ocean. *Environ. Sci. Technol.* **2010**, *44* (1), 191–196. https://doi.org/10.1021/es901766r.
(127) Pham, A. N.; Xing, G.; Miller, C. J.; Waite, T. D. Fenton-like Copper Redox Chemistry Revisited: Hydrogen Peroxide and Superoxide Mediation of Copper-Catalyzed Oxidant Production. *J. Catal.* **2013**, *301*, 54–64. https://doi.org/10.1016/j.jcat.2013.01.025.
(128) Hansard, S. P.; Easter, H. D.; Voelker, B. M. Rapid Reaction of Nanomolar Mn(II) with Superoxide Radical in Seawater and Simulated Freshwater. *Environ. Sci. Technol.* **2011**, *45* (7), 2811–2817. https://doi.org/10.1021/es104014s.
(129) Wuttig, K.; Heller, M. I.; Croot, P. L. Reactivity of Inorganic Mn and Mn Desferrioxamine B with O2, O2–, and H2O2 in Seawater. *Environ. Sci. Technol.* **2013**, *47* (18), 10257–10265. https://doi.org/10.1021/es4016603.
(130) Wuttig, K.; Heller, M. I.; Croot, P. L. Pathways of Superoxide (O2–) Decay in the Eastern Tropical North Atlantic. *Environ. Sci. Technol.* **2013**, *47* (18), 10249–10256. https://doi.org/10.1021/es401658t.
(131) Madison, A. S.; Tebo, B. M.; Mucci, A.; Sundby, B.; George W. Luther, I. I. I. Abundant Porewater Mn(III) Is a Major Component of the Sedimentary Redox System. *Science* **2013**. https://doi.org/10.1126/science.1241396.
(132) Oldham, V. E.; Mucci, A.; Tebo, B. M.; Luther, G. W. Soluble Mn(III)–L Complexes Are Abundant in Oxygenated Waters and Stabilized by Humic Ligands. *Geochim. Cosmochim. Acta* **2017**, *199*, 238–246. https://doi.org/10.1016/j.gca.2016.11.043.
(133) Jones, M. R.; Luther, G. W.; Mucci, A.; Tebo, B. M. Concentrations of Reactive Mn(III)-L and MnO2 in Estuarine and Marine Waters Determined Using Spectrophotometry and the Leuco Base, Leucoberbelin Blue. *Talanta* **2019**, *200*, 91–99. https://doi.org/10.1016/j.talanta.2019.03.026.
(134) Jones, M. R.; Luther, G. W.; Tebo, B. M. Distribution and Concentration of Soluble Manganese(II), Soluble Reactive Mn(III)-L, and Particulate MnO2 in the Northwest Atlantic Ocean. *Mar. Chem.* **2020**, *226*, 103858. https://doi.org/10.1016/j.marchem.2020.103858.
(135) Chaput, D. L.; Fowler, A. J.; Seo, O.; Duhn, K.; Hansel, C. M.; Santelli, C. M. Mn Oxide Formation by Phototrophs: Spatial and Temporal Patterns, with Evidence of an Enzymatic Superoxide-Mediated Pathway. *Sci. Rep.* **2019**, *9* (1), 18244. https://doi.org/10.1038/s41598-019-54403-8.
(136) Post, J. E. Manganese Oxide Minerals: Crystal Structures and Economic and Environmental Significance. *Proc. Natl. Acad. Sci.* **1999**, *96* (7), 3447–3454. https://doi.org/10.1073/pnas.96.7.3447.

(137) Bienert, G. P.; Schjoerring, J. K.; Jahn, T. P. Membrane Transport of Hydrogen Peroxide. *Biochim. Biophys. Acta BBA - Biomembr.* **2006**, *1758* (8), 994–1003. https://doi.org/10.1016/j.bbamem.2006.02.015.
(138) Cordeiro, R. M. Reactive Oxygen Species at Phospholipid Bilayers: Distribution, Mobility and Permeation. *Biochim. Biophys. Acta BBA - Biomembr.* **2014**, *1838* (1, Part B), 438–444. https://doi.org/10.1016/j.bbamem.2013.09.016.
(139) Korshunov, S. S.; Imlay, J. A. A Potential Role for Periplasmic Superoxide Dismutase in Blocking the Penetration of External Superoxide into the Cytosol of Gram-Negative Bacteria. *Mol. Microbiol.* **2002**, *43* (1), 95–106. https://doi.org/10.1046/j.1365-2958.2002.02719.x.
(140) Wolf, R.; Andersen, T.; Hessen, D. O.; Hylland, K. The Influence of Dissolved Organic Carbon and Ultraviolet Radiation on the Genomic Integrity of Daphnia Magna. *Funct. Ecol.* **2017**, *31* (4), 848–855. https://doi.org/10.1111/1365-2435.12730.
(141) Baltar, F.; Reinthaler, T.; Herndl, G. J.; Pinhassi, J. Major Effect of Hydrogen Peroxide on Bacterioplankton Metabolism in the Northeast Atlantic. *PLOS ONE* **2013**, *8* (4), e61051. https://doi.org/10.1371/journal.pone.0061051.
(142) Moffett, J. W.; Zafiriou, O. C. An Investigation Ofhydrogen Peroxide Chemistry in Surface Waters of Vineyard Sound with H218O2 and 18O2. *Limnol. Oceanogr.* **1990**, *35* (6), 1221–1229. https://doi.org/10.4319/lo.1990.35.6.1221.
(143) Sutherland, K. M.; Grabb, K. C.; Karolewski, J. S.; Taenzer, L.; Hansel, C. M.; Wankel, S. D. The Redox Fate of Hydrogen Peroxide in the Marine Water Column. *Limnol. Oceanogr.* **2021**, *66* (10), 3828–3841. https://doi.org/10.1002/lno.11922.
(144) Morris, J. J.; Johnson, Z. I.; Szul, M. J.; Keller, M.; Zinser, E. R. Dependence of the Cyanobacterium Prochlorococcus on Hydrogen Peroxide Scavenging Microbes for Growth at the Ocean's Surface. *PLOS ONE* **2011**, *6* (2), e16805. https://doi.org/10.1371/journal.pone.0016805.
(145) Clark, C. D.; De Bruyn, W. J.; Jakubowski, S. D.; Grant, S. B. Hydrogen Peroxide Production in Marine Bathing Waters: Implications for Fecal Indicator Bacteria Mortality. *Mar. Pollut. Bull.* **2008**, *56* (3), 397–401. https://doi.org/10.1016/j.marpolbul.2007.10.017.
(146) Diaz, J. M.; Hansel, C. M.; Apprill, A.; Brighi, C.; Zhang, T.; Weber, L.; McNally, S.; Xun, L. Species-Specific Control of External Superoxide Levels by the Coral Holobiont during a Natural Bleaching Event. *Nat. Commun.* **2016**, *7* (1), 13801. https://doi.org/10.1038/ncomms13801.
(147) Diaz, J. M.; Plummer, S.; Tomas, C.; Alves-de-Souza, C. Production of Extracellular Superoxide and Hydrogen Peroxide by Five Marine Species of Harmful Bloom-Forming Algae. *J. Plankton Res.* **2018**, *40* (6), 667–677. https://doi.org/10.1093/plankt/fby043.
(148) Rose, A. L.; Salmon, T. P.; Lukondeh, T.; Neilan, B. A.; Waite, T. D. Use of Superoxide as an Electron Shuttle for Iron Acquisition by the Marine Cyanobacterium Lyngbya Majuscula. *Environ. Sci. Technol.* **2005**, *39* (10), 3708–3715. https://doi.org/10.1021/es048766c.
(149) Learman, D. R.; Voelker, B. M.; Vazquez-Rodriguez, A. I.; Hansel, C. M. Formation of Manganese Oxides by Bacterially Generated Superoxide. *Nat. Geosci.* **2011**, *4* (2), 95–98. https://doi.org/10.1038/ngeo1055.
(150) Wang, X.; Wang, S.; Qu, R.; Ge, J.; Wang, Z.; Gu, C. Enhanced Removal of Chlorophene and 17β-Estradiol by Mn(III) in a Mixture Solution with Humic Acid: Investigation of

Reaction Kinetics and Formation of Co-Oligomerization Products. *Environ. Sci. Technol.* **2018**, *52* (22), 13222–13230. https://doi.org/10.1021/acs.est.8b04116.
(151) Chen, Y.; Zhang, X.; Feng, S. Contribution of the Excited Triplet State of Humic Acid and Superoxide Radical Anion to Generation and Elimination of Phenoxyl Radical. *Environ. Sci. Technol.* **2018**, *52* (15), 8283–8291. https://doi.org/10.1021/acs.est.8b00890.
(152) Zhou, Q.; Zhang, X.; Zhou, C. Transformation of Amino Acid Tyrosine in Chromophoric Organic Matter Solutions: Generation of Peroxide and Change of Bioavailability. *Chemosphere* **2020**, *245*, 125662. https://doi.org/10.1016/j.chemosphere.2019.125662.
(153) Rong, H.; Garg, S.; Waite, T. D. Impact of Light and Suwanee River Fulvic Acid on O2 and H2O2 Mediated Oxidation of Silver Nanoparticles in Simulated Natural Waters. *Environ. Sci. Technol.* **2019**. https://doi.org/10.1021/acs.est.8b07079.
(154) Rochelle-Newall, E. J.; Fisher, T. R. Production of Chromophoric Dissolved Organic Matter Fluorescence in Marine and Estuarine Environments: An Investigation into the Role of Phytoplankton. *Mar. Chem.* **2002**, *77* (1), 7–21. https://doi.org/10.1016/S0304-4203(01)00072-X.
(155) Castillo, C. R.; Sarmento, H.; Álvarez-Salgado, X. A.; Gasol, J. M.; Marraséa, C. Production of Chromophoric Dissolved Organic Matter by Marine Phytoplankton. *Limnol. Oceanogr.* **2010**, *55* (1), 446–454. https://doi.org/10.4319/lo.2010.55.1.0446.
(156) Steinberg, D.; Nelson, N. B.; Carlson, C. A.; Prusak, A. C. Production of Chromophoric Dissolved Organic Matter (CDOM) in the Open Ocean by Zooplankton and the Colonial Cyanobacterium Trichodesmium Spp. *Mar. Ecol. Prog. Ser.* **2004**, *267*, 45–56. https://doi.org/ 10.3354/meps267045 .
(157) Del Vecchio, R.; Blough, N. V. Photobleaching of Chromophoric Dissolved Organic Matter in Natural Waters: Kinetics and Modeling. *Mar. Chem.* **2002**, *78* (4), 231–253. https://doi.org/10.1016/S0304-4203(02)00036-1.
(158) Helms, J. R.; Mao, J.; Stubbins, A.; Schmidt-Rohr, K.; Spencer, R. G. M.; Hernes, P. J.; Mopper, K. Loss of Optical and Molecular Indicators of Terrigenous Dissolved Organic Matter during Long-Term Photobleaching. *Aquat. Sci.* **2014**, *76* (3), 353–373. https://doi.org/10.1007/s00027-014-0340-0.
(159) Dalzell, B. J.; Minor, E. C.; Mopper, K. M. Photodegradation of Estuarine Dissolved Organic Matter: A Multi-Method Assessment of DOM Transformation. *Org. Geochem.* **2009**, *40* (2), 243–257. https://doi.org/10.1016/j.orggeochem.2008.10.003.
(160) Miller, W. L.; Zepp, R. G. Photochemical Production of Dissolved Inorganic Carbon from Terrestrial Organic Matter: Significance to the Oceanic Organic Carbon Cycle. *Geophys. Res. Lett.* **1995**, *22* (4), 417–420. https://doi.org/10.1029/94GL03344.
(161) Gao, H.; Zepp, R. G. Factors Influencing Photoreactions of Dissolved Organic Matter in a Coastal River of the Southeastern United States. *Environ. Sci. Technol.* **1998**, *32* (19), 2940–2946. https://doi.org/10.1021/es9803660.
(162) Goldstone, J. V.; Pullin, M. J.; Bertilsson, S.; Voelker, B. M. Reactions of Hydroxyl Radical with Humic Substances: Bleaching, Mineralization, and Production of Bioavailable Carbon Substrates. *Environ. Sci. Technol.* **2002**, *36* (3), 364–372. https://doi.org/10.1021/es0109646.
(163) Stubbins, A.; Hubbard, V.; Uher, G.; Law, C. S.; Upstill-Goddard, R. C.; Aiken, G. R.; Mopper, K. Relating Carbon Monoxide Photoproduction to Dissolved Organic Matter Functionality. *Environ. Sci. Technol.* **2008**, *42* (9), 3271–3276. https://doi.org/10.1021/es703014q.

(164) Reader, H. E.; Miller, W. L. Variability of Carbon Monoxide and Carbon Dioxide Apparent Quantum Yield Spectra in Three Coastal Estuaries of the South Atlantic Bight. *Biogeosciences* **2012**, *9* (11), 4279–4294. https://doi.org/10.5194/bg-9-4279-2012.
(165) Sharpless, C. M.; Aeschbacher, M.; Page, S. E.; Wenk, J.; Sander, M.; McNeill, K. Photooxidation-Induced Changes in Optical, Electrochemical, and Photochemical Properties of Humic Substances. *Environ. Sci. Technol.* **2014**, *48* (5), 2688–2696. https://doi.org/10.1021/es403925g.
(166) Moran, M. A.; Sheldon, W.; Zepp, R. Carbon Loss and Optical Property Changes during Long-Term Photochemical and Biological Degradation of Estuarine Dissolved Organic Matter. *Limnol. Oceanogr.* **2000**, *45*, 1254–1264. https://doi.org/10.4319/lo.2000.45.6.1254.
(167) Spencer, R. G. M.; Stubbins, A.; Hernes, P. J.; Baker, A.; Mopper, K.; Aufdenkampe, A. K.; Dyda, R. Y.; Mwamba, V. L.; Mangangu, A. M.; Wabakanghanzi, J. N.; Six, J. Photochemical Degradation of Dissolved Organic Matter and Dissolved Lignin Phenols from the Congo River. *J. Geophys. Res. Biogeosciences* **2009**, *114* (G3). https://doi.org/10.1029/2009JG000968.
(168) Stubbins, A.; Spencer, R. G. M.; Chen, H.; Hatcher, P. G.; Mopper, K.; Hernes, P. J.; Mwamba, V. L.; Mangangu, A. M.; Wabakanghanzi, J. N.; Six, J. Illuminated Darkness: Molecular Signatures of Congo River Dissolved Organic Matter and Its Photochemical Alteration as Revealed by Ultrahigh Precision Mass Spectrometry. *Limnol. Oceanogr.* **2010**, *55* (4), 1467–1477. https://doi.org/10.4319/lo.2010.55.4.1467.
(169) Dittmar, T.; Whitehead, K.; Minor, E. C.; Koch, B. P. Tracing Terrigenous Dissolved Organic Matter and Its Photochemical Decay in the Ocean by Using Liquid Chromatography/Mass Spectrometry. *Mar. Chem.* **2007**, *107* (3), 378–387. https://doi.org/10.1016/j.marchem.2007.04.006.
(170) Opsahl, S. P.; Zepp, R. G. Photochemically-Induced Alteration of Stable Carbon Isotope Ratios (Δ13C) in Terrigenous Dissolved Organic Carbon. *Geophys. Res. Lett.* **2001**, *28* (12), 2417–2420. https://doi.org/10.1029/2000GL012686.
(171) Peterson, B.; Fry, B.; Hullar, M.; Saupe, S.; Wright, R. The Distribution and Stable Carbon Isotopic Composition of Dissolved Organic Carbon in Estuaries. *Estuaries* **1994**, *17* (1), 111–121. https://doi.org/10.2307/1352560.
(172) Benner, R.; Opsahl, S. Molecular Indicators of the Sources and Transformations of Dissolved Organic Matter in the Mississippi River Plume. *Org. Geochem.* **2001**, *32* (4), 597–611. https://doi.org/10.1016/S0146-6380(00)00197-2.
(173) Gonsior, M.; Peake, B. M.; Cooper, W. T.; Podgorski, D.; D'Andrilli, J.; Cooper, W. J. Photochemically Induced Changes in Dissolved Organic Matter Identified by Ultrahigh Resolution Fourier Transform Ion Cyclotron Resonance Mass Spectrometry. *Environ. Sci. Technol.* **2009**, *43* (3), 698–703. https://doi.org/10.1021/es8022804.
(174) Andrews, S. S.; Caron, S.; Zafiriou, O. C. Photochemical Oxygen Consumption in Marine Waters: A Major Sink for Colored Dissolved Organic Matter? *Limnol. Oceanogr.* **2000**, *45* (2), 267–277. https://doi.org/10.4319/lo.2000.45.2.0267.
(175) Waggoner, D. C.; Chen, H.; Willoughby, A. S.; Hatcher, P. G. Formation of Black Carbon-like and Alicyclic Aliphatic Compounds by Hydroxyl Radical Initiated Degradation of Lignin. *Org. Geochem.* **2015**, *82*, 69–76. https://doi.org/10.1016/j.orggeochem.2015.02.007.

(176) Scully, N. M.; Cooper, W. J.; Tranvik, L. J. Photochemical Effects on Microbial Activity in Natural Waters: The Interaction of Reactive Oxygen Species and Dissolved Organic Matter. *FEMS Microbiol. Ecol.* **2003**, *46* (3), 353–357. https://doi.org/10.1016/S0168-6496(03)00198-3.
(177) Waggoner, D. C.; Wozniak, A. S.; Cory, R. M.; Hatcher, P. G. The Role of Reactive Oxygen Species in the Degradation of Lignin Derived Dissolved Organic Matter. *Geochim. Cosmochim. Acta* **2017**, *208*, 171–184. https://doi.org/10.1016/j.gca.2017.03.036.
(178) Zepp, R. G.; Callaghan, T. V.; Iii, D. J. E. Interactive Effects of Ozone Depletion and Climate Change on Biogeochemical Cycles. *Photochem. Photobiol. Sci.* **2003**, *2* (1), 51–61. https://doi.org/10.1039/B211154N.
(179) Vione, D.; Scozzaro, A. Photochemistry of Surface Fresh Waters in the Framework of Climate Change. *Environ. Sci. Technol.* **2019**, *53* (14), 7945–7963. https://doi.org/10.1021/acs.est.9b00968.
(180) Steinacher, M.; Joos, F.; Frölicher, T. L.; Plattner, G.-K.; Doney, S. C. Imminent Ocean Acidification in the Arctic Projected with the NCAR Global Coupled Carbon Cycle-Climate Model. *Biogeosciences* **2009**, *6* (4), 515–533. https://doi.org/10.5194/bg-6-515-2009.
(181) Timko, S. A.; Gonsior, M.; Cooper, W. J. Influence of PH on Fluorescent Dissolved Organic Matter Photo-Degradation. *Water Res.* **2015**, *85*, 266–274. https://doi.org/10.1016/j.watres.2015.08.047.
(182) Song, G.; Li, Y.; Hu, S.; Li, G.; Zhao, R.; Sun, X.; Xie, H. Photobleaching of Chromophoric Dissolved Organic Matter (CDOM) in the Yangtze River Estuary: Kinetics and Effects of Temperature, PH, and Salinity. *Env. Sci Process. Impacts* **2017**, *19* (6), 861–873.
(183) Gu, Y.; Lensu, A.; Perämäki, S.; Ojala, A.; Vähätalo, A. V. Iron and PH Regulating the Photochemical Mineralization of Dissolved Organic Carbon. *ACS Omega* **2017**, *2* (5), 1905–1914. https://doi.org/10.1021/acsomega.7b00453.
(184) Millero, F. J.; Sotolongo, S. The Oxidation of Fe(II) with H2O2 in Seawater. *Geochim. Cosmochim. Acta* **1989**, *53* (8), 1867–1873. https://doi.org/10.1016/0016-7037(89)90307-4.
(185) Miller, C. J.; Rose, A. L.; Waite, T. D. Impact of Natural Organic Matter on H2O2-Mediated Oxidation of Fe(II) in a Simulated Freshwater System. *Geochim. Cosmochim. Acta* **2009**, *73* (10), 2758–2768. https://doi.org/10.1016/j.gca.2009.02.027.
(186) Voelker, B. M.; Sulzberger, B. Effects of Fulvic Acid on Fe(II) Oxidation by Hydrogen Peroxide. *Environ. Sci. Technol.* **1996**, *30* (4), 1106–1114. https://doi.org/10.1021/es9502132.
(187) Mostofa, K. M. G.; Liu, C.; Minella, M.; Vione, D. Balancing of Ocean Acidification by Superoxide Redox Chemistry? *Environ. Sci. Technol.* **2013**, *47* (20), 11380–11381. https://doi.org/10.1021/es4039177.
(188) Zafiriou, O. C.; Blough, N. V.; Micinski, E.; Dister, B.; Kieber, D.; Moffett, J. Molecular Probe Systems for Reactive Transients in Natural Waters. *Mar. Chem.* **1990**, *30*, 45–70. https://doi.org/10.1016/0304-4203(90)90061-G.
(189) Blough, N. V. Electron Paramagnetic Resonance Measurements of Photochemical Radical Production in Humic Substances. 1. Effects of Oxygen and Charge on Radical Scavenging

by Nitroxides. *Environ. Sci. Technol.* **1988**, *22* (1), 77–82. https://doi.org/10.1021/es00166a008.
(190) Jia, M.; Tang, Y.; Lam, Y.-F.; Green, S. A.; Blough, N. V. Prefluorescent Nitroxide Probe for the Highly Sensitive Determination of Peroxyl and Other Radical Oxidants. *Anal. Chem.* **2009**, *81* (19), 8033–8040. https://doi.org/10.1021/ac901374m.
(191) Kieber, D. J.; Blough, N. V. Fluorescence Detection of Carbon-Centered Radicals in Aqueous Solution. *Free Radic. Res. Commun.* **1990**, *10* (1–2), 109–117. https://doi.org/10.3109/10715769009145940.
(192) Green, S. A.; Simpson, D. J.; Zhou, G.; Ho, P. S.; Blough, N. V. Intramolecular Quenching of Excited Singlet States by Stable Nitroxyl Radicals. *J. Am. Chem. Soc.* **1990**, *112* (20), 7337–7346. https://doi.org/10.1021/ja00176a038.
(193) Kieber, D. J.; Blough, N. V. Determination of Carbon-Centered Radicals in Aqueous Solution by Liquid Chromatography with Fluorescence Detection. *Anal. Chem.* **1990**, *62* (21), 2275–2283. https://doi.org/10.1021/ac00220a005.
(194) Blough, N. V. Electron Paramagnetic Resonance Measurements of Photochemical Radical Production in Humic Substances. 1. Effects of Oxygen and Charge on Radical Scavenging by Nitroxides. *Environ. Sci. Technol.* **1988**, *22* (1), 77–82. https://doi.org/10.1021/es00166a008.
(195) Andrew, A. A.; Del Vecchio, R.; Zhang, Y.; Subramaniam, A.; Blough, N. V. Are Extracted Materials Truly Representative of Original Samples? Impact of C18 Extraction on CDOM Optical and Chemical Properties. *Front. Chem.* **2016**, *4*. https://doi.org/10.3389/fchem.2016.00004.
(196) Dixon, M. The Acceptor Specificity of Flavins and Flavoproteins. I. Techniques for Anaerobic Spectrophotometry. *Biochim. Biophys. Acta BBA - Bioenerg.* **1971**, *226* (2), 241–258. https://doi.org/10.1016/0005-2728(71)90092-2.
(197) Anderson, J. H. The Copper-Catalysed Oxidation of Hydroxylamine. *The Analyst* **1964**, *89* (1058), 357. https://doi.org/10.1039/an9648900357.
(198) Gomez, E.; Estela, J. M.; Cerda, V. Thermometric Determination of CuIIbased on Its Catalytic Effect on the Oxidation of Hydroxylamine by Dissolved Oxygen. *Thermochim. Acta* **1990**, *165* (2), 255–260. https://doi.org/10.1016/0040-6031(90)80225-N.
(199) Green, S. A.; Morel, F. M. M.; Blough, N. V. Investigation of the Electrostatic Properties of Humic Substances by Fluorescence Quenching. *Environ. Sci. Technol.* **1992**, *26* (2), 294–302. https://doi.org/10.1021/es00026a008.
(200) Amador, J. A.; Alexander, M.; Zika, R. G. Sequential Photochemical and Microbial Degradation of Organic Molecules Bound to Humic Acid. *Appl. Environ. Microbiol.* **1989**, *55* (11), 2843–2849.
(201) Felix, A. M.; Toome, V.; De Bernardo, S.; Weigele, M. Colorimetric Amino Acid Analysis Using Fluorescamine. *Arch. Biochem. Biophys.* **1975**, *168* (2), 601–608. https://doi.org/10.1016/0003-9861(75)90292-1.
(202) Udenfriend, S.; Stein, S.; Böhlen, P.; Dairman, W.; Leimgruber, W.; Weigele, M. Fluorescamine: A Reagent for Assay of Amino Acids, Peptides, Proteins, and Primary Amines in the Picomole Range. *Science* **1972**, *178* (4063), 871–872. https://doi.org/10.1126/science.178.4063.871.
(203) Kosseva, M. R.; Kennedy, J. F. Food Proteins: Processing Applications Shuryo Nakai & H. Wayne Modler. *Bioseparation* **2000**, *9* (4), 257–257. https://doi.org/10.1023/A:1008109625991.

(204) Poste, A.; Grung, M.; Wright, R. Amines and Amine-Related Compounds in Surface Waters: A Review of Sources, Concentrations and Aquatic Toxicity. *Sci. Total Environ.* **2014**, *481C*, 274–279. https://doi.org/10.1016/j.scitotenv.2014.02.066.
(205) Stein, S.; Böhlen, P.; Udenfriend, S. Studies on the Kinetics of Reaction and Hydrolysis of Fluorescamine. *Arch. Biochem. Biophys.* **1974**, *163* (1), 400–403. https://doi.org/10.1016/0003-9861(74)90491-3.
(206) Helms, J. R.; Stubbins, A.; Ritchie, J. D.; Minor, E. C.; Kieber, D. J.; Mopper, K. Absorption Spectral Slopes and Slope Ratios as Indicators of Molecular Weight, Source, and Photobleaching of Chromophoric Dissolved Organic Matter. *Limnol. Oceanogr.* **2008**, *53* (3), 955–969. https://doi.org/10.4319/lo.2008.53.3.0955.
(207) Peuravuori, J.; Pihlaja, K. Molecular Size Distribution and Spectroscopic Properties of Aquatic Humic Substances. *Anal. Chim. Acta* **1997**, *337* (2), 133–149. https://doi.org/10.1016/S0003-2670(96)00412-6.
(208) Weishaar, J. L.; Aiken, G. R.; Bergamaschi, B. A.; Fram, M. S.; Fujii, R.; Mopper, K. Evaluation of Specific Ultraviolet Absorbance as an Indicator of the Chemical Composition and Reactivity of Dissolved Organic Carbon. *Environ. Sci. Technol.* **2003**, *37* (20), 4702–4708. https://doi.org/10.1021/es030360x.
(209) Fujii, M.; Otani, E. Photochemical Generation and Decay Kinetics of Superoxide and Hydrogen Peroxide in the Presence of Standard Humic and Fulvic Acids. *Water Res.* **2017**, *123*, 642–654. https://doi.org/10.1016/j.watres.2017.07.015.
(210) O'Sullivan, D. W.; Neale, P. J.; Coffin, R. B.; Boyd, T. J.; Osburn, C. L. Photochemical Production of Hydrogen Peroxide and Methylhydroperoxide in Coastal Waters. *Mar. Chem.* **2005**, *97* (1), 14–33. https://doi.org/10.1016/j.marchem.2005.04.003.
(211) García, P. E.; Queimaliños, C.; Diéguez, M. C. Natural Levels and Photo-Production Rates of Hydrogen Peroxide (H2O2) in Andean Patagonian Aquatic Systems: Influence of the Dissolved Organic Matter Pool. *Chemosphere* **2019**, *217*, 550–557. https://doi.org/10.1016/j.chemosphere.2018.10.179.
(212) Green, S. A.; Blough, N. V. Optical Absorption and Fluorescence Properties of Chromophoric Dissolved Organic Matter in Natural Waters. *Limnol. Oceanogr.* **1994**, *39* (8), 1903–1916. https://doi.org/10.4319/lo.1994.39.8.1903.
(213) Velapoldi, R. A.; Tønnesen, H. H. Corrected Emission Spectra and Quantum Yields for a Series of Fluorescent Compounds in the Visible Spectral Region. *J. Fluoresc.* **2004**, *14* (4), 465–472. https://doi.org/10.1023/B:JOFL.0000031828.96368.c1.
(214) Brouwer, A. M. Standards for photoluminescence quantum yield measurements in solution (IUPAC Technical Report). *Pure Appl. Chem.* **2011**, *83* (12), 2213–2228. https://doi.org/10.1351/PAC-REP-10-09-31.
(215) Scully, N. M.; McQueen, D. J.; Lean, D. R. S. Hydrogen Peroxide Formation: The Interaction of Ultraviolet Radiation and Dissolved Organic Carbon in Lake Waters along a 43-75°N Gradient. *Limnol. Oceanogr.* **1996**, *41* (3), 540–548. https://doi.org/10.4319/lo.1996.41.3.0540.
(216) Li, P.; Hur, J. Utilization of UV-Vis Spectroscopy and Related Data Analyses for Dissolved Organic Matter (DOM) Studies: A Review. *Crit. Rev. Environ. Sci. Technol.* **2017**, *47* (3), 131–154. https://doi.org/10.1080/10643389.2017.1309186.
(217) Stetzenbach, K. J.; Thompson, G. M. A New Method for Simultaneous Measurement of Cl−, Br−, NO3−, SCN−, and I− at Sub-Ppm Levels in Ground Water. *Groundwater* **1983**, *21* (1), 36–41. https://doi.org/10.1111/j.1745-6584.1983.tb00702.x.

(218) Catalá, T. S.; Reche, I.; Ramón, C. L.; López-Sanz, À.; Álvarez, M.; Calvo, E.; Álvarez-Salgado, X. A. Chromophoric Signatures of Microbial By-Products in the Dark Ocean: MICROBIAL CHROMOPHORIC SIGNATURES. *Geophys. Res. Lett.* **2016**, *43* (14), 7639–7648. https://doi.org/10.1002/2016GL069878.
(219) Xiao, Y.-H.; Sara-Aho, T.; Hartikainen, H.; Vähätalo, A. V. Contribution of Ferric Iron to Light Absorption by Chromophoric Dissolved Organic Matter. *Limnol. Oceanogr.* **2013**, *58* (2), 653–662. https://doi.org/10.4319/lo.2013.58.2.0653.
(220) Poulin, B. A.; Gerbig, C. A.; Kim, C. S.; Stegemeier, J. P.; Ryan, J. N.; Aiken, G. R. Effects of Sulfide Concentration and Dissolved Organic Matter Characteristics on the Structure of Nanocolloidal Metacinnabar. *Environ. Sci. Technol.* **2017**, *51* (22), 13133–13142. https://doi.org/10.1021/acs.est.7b02687.
(221) Stirchak, L. T.; Moor, K. J.; McNeill, K.; Donaldson, D. J. Differences in Photochemistry between Seawater and Freshwater for Two Natural Organic Matter Samples. *Environ. Sci. Process. Impacts* **2019**, *21* (1), 28–39. https://doi.org/10.1039/C8EM00431E.
(222) Ryan, D.; Weber, J. Copper(II) Complexing Capacities of Natural Waters by Fluorescence Quenching. *Environ. Sci. Technol.* **1982**, *16* (12), 866–872. https://doi.org/10.1021/es00106a009.
(223) Schendorf, T. M.; Del Vecchio, R.; Bianca, M.; Blough, N. V. Combined Effects of PH and Borohydride Reduction on the Optical Properties of Humic Substances (HS): A Comparison of Optical Models. *Environ. Sci. Technol.* **2019**, *53* (11), 6310–6319. https://doi.org/10.1021/acs.est.9b01516.
(224) Ritchie, J. D.; Perdue, E. M. Proton-Binding Study of Standard and Reference Fulvic Acids, Humic Acids, and Natural Organic Matter. *Geochim. Cosmochim. Acta* **2003**, *67* (1), 85–96.
(225) Karentz, D.; McEuen, F. S.; Land, M. C.; Dunlap, W. C. Survey of Mycosporine-like Amino Acid Compounds in Antarctic Marine Organisms: Potential Protection from Ultraviolet Exposure. *Mar. Biol.* **1991**, *108* (1), 157–166. https://doi.org/10.1007/BF01313484.
(226) Hulatt, C. J.; Thomas, D. N.; Bowers, D. G.; Norman, L.; Zhang, C. Exudation and Decomposition of Chromophoric Dissolved Organic Matter (CDOM) from Some Temperate Macroalgae. *Estuar. Coast. Shelf Sci.* **2009**, *84* (1), 147–153. https://doi.org/10.1016/j.ecss.2009.06.014.
(227) Powers, L. C.; Hertkorn, N.; McDonald, N.; Schmitt-Kopplin, P.; Vecchio, R. D.; Blough, N. V.; Gonsior, M. Sargassum Sp. Act as a Large Regional Source of Marine Dissolved Organic Carbon and Polyphenols. *Glob. Biogeochem. Cycles* **2019**, *33* (11), 1423–1439. https://doi.org/10.1029/2019GB006225.
(228) Stuever Kaltenbach, M.; Arnold, M. A. Acridinium Ester Chemiluminescence: PH Dependent Hydrolysis of Reagents and Flow Injection Analysis of Hydrogen Peroxide and Glutamate. *Mikrochim. Acta* **1992**, *108* (3–6), 205–219. https://doi.org/10.1007/BF01242430.
(229) *Waterville Analytical Chemistries*. http://www.watervilleanalytical.com/chemistries.html (accessed 2018-04-09).
(230) Miller, W. L.; Kester, D. R. Hydrogen Peroxide Measurement in Seawater by (p-Hydroxyphenyl)Acetic Acid Dimerization. *Anal. Chem.* **1988**, *60* (24), 2711–2715. https://doi.org/10.1021/ac00175a014.

(231) Rose, A. L.; Moffett, J. W.; Waite, T. D. Determination of Superoxide in Seawater Using 2-Methyl-6-(4-Methoxyphenyl)-3,7- Dihydroimidazo[1,2-a]Pyrazin-3(7 *H*)-One Chemiluminescence. *Anal. Chem.* **2008**, *80* (4), 1215–1227. https://doi.org/10.1021/ac7018975.
(232) McDowell, M. S.; Bakac, A.; Espenson, J. H. A Convenient Route to Superoxide Ion in Aqueous Solution. *Inorg. Chem.* **1983**, *22* (5), 847–848. https://doi.org/10.1021/ic00147a033.
(233) Sikorski, R. J.; Zika, R. G. Modeling Mixed-Layer Photochemistry of H_2O_2: Optical and Chemical Modeling of Production. *J. Geophys. Res. Oceans* **1993**, *98* (C2), 2315–2328. https://doi.org/10.1029/92JC02933.
(234) Jerome, J. H.; Bukata, R. P. Impact of Stratospheric Ozone Depletion on Photoproduction of Hydrogen Peroxide in Lake Ontario. *J. Gt. Lakes Res.* **1998**, *24* (4), 929–935. https://doi.org/10.1016/S0380-1330(98)70873-1.
(235) Andrews, S. S.; Caron, S.; Zafiriou, O. C. Photochemical Oxygen Consumption in Marine Waters: A Major Sink for Colored Dissolved Organic Matter? *Limnol. Oceanogr.* **2000**, *45* (2), 267–277. https://doi.org/10.4319/lo.2000.45.2.0267.
(236) Miller, W. L.; Moran, M.; Sheldon, W. M.; Zepp, R. G.; Opsahl, S. Determination of Apparent Quantum Yield Spectra for the Formation of Biologically Labile Photoproducts. *Limnol. Oceanogr.* **2002**, *47* (2), 343–352. https://doi.org/10.4319/lo.2002.47.2.0343.
(237) Kieber, D. J.; Miller, G. W.; Neale, P. J.; Mopper, K. Wavelength and Temperature-Dependent Apparent Quantum Yields for Photochemical Formation of Hydrogen Peroxide in Seawater. *Environ. Sci. Process. Impacts* **2014**, *16* (4), 777–791. https://doi.org/10.1039/C4EM00036F.
(238) Powers, L. C.; Miller, W. L. Hydrogen Peroxide and Superoxide Photoproduction in Diverse Marine Waters: A Simple Proxy for Estimating Direct CO_2 Photochemical Fluxes: H_2O_2 /O_2^- PROXY FOR CO_2 PHOTOPRODUCTION. *Geophys. Res. Lett.* **2015**, *42* (18), 7696–7704. https://doi.org/10.1002/2015GL065669.
(239) Zhang, Y.; Simon, K. A.; Andrew, A. A.; Del Vecchio, R.; Blough, N. V. Enhanced Photoproduction of Hydrogen Peroxide by Humic Substances in the Presence of Phenol Electron Donors. *Environ. Sci. Technol.* **2014**, *48* (21), 12679–12688. https://doi.org/10.1021/es5035798.
(240) Fichot, C. G.; Miller, W. L. An Approach to Quantify Depth-Resolved Marine Photochemical Fluxes Using Remote Sensing: Application to Carbon Monoxide (CO) Photoproduction. *Remote Sens. Environ.* **2010**, *114* (7), 1363–1377. https://doi.org/10.1016/j.rse.2010.01.019.
(241) Powers, L. C.; Babcock-Adams, L. C.; Enright, J. K.; Miller, W. L. Probing the Photochemical Reactivity of Deep Ocean Refractory Carbon (DORC): Lessons from Hydrogen Peroxide and Superoxide Kinetics. *Mar. Chem.* **2015**, *177*, 306–317. https://doi.org/10.1016/j.marchem.2015.06.005.
(242) Bray, R. C.; Mautner, G. N.; Fielden, E. M.; Carle, C. I. STUDIES ON THE SUPEROXIDE ION: COMPLEX FORMATION WITH BARIUM AND CALCIUM IONS DETECTED BY e.p.r. SPECTROSCOPY AND KINETICALLY. 16.
(243) Millero, F. J. Estimate of the Life Time of Superoxide in Seawater. *Geochim. Cosmochim. Acta* **1987**, *51* (2), 351–353. https://doi.org/10.1016/0016-7037(87)90246-8.

(244) Buerge-Weirich, D.; Sulzberger, B. Formation of Cu(I) in Estuarine and Marine Waters: Application of a New Solid-Phase Extraction Method To Measure Cu(I). *Environ. Sci. Technol.* **2004**, *38* (6), 1843–1848. https://doi.org/10.1021/es034845x.
(245) Miller, W. L.; King, D. W.; Lin, J.; Kester, D. R. Photochemical Redox Cycling of Iron in Coastal Seawater. *Mar. Chem.* **1995**, *50* (1–4), 63–77. https://doi.org/10.1016/0304-4203(95)00027-O.
(246) Zafiriou, O. C.; Voelker, B. M.; Sedlak, D. L. Chemistry of the Superoxide Radical (O2-) in Seawater: Reactions with Inorganic Copper Complexes. *J. Phys. Chem. A* **1998**, *102* (28), 5693–5700. https://doi.org/10.1021/jp980709g.
(247) Rose, A. L.; Waite, T. D. Role of Superoxide in the Photochemical Reduction of Iron in Seawater. *Geochim. Cosmochim. Acta* **2006**, *70* (15), 3869–3882. https://doi.org/10.1016/j.gca.2006.06.008.
(248) Garg, S.; Rose, A. L.; Waite, T. D. Superoxide Mediated Reduction of Organically Complexed Iron(III): Comparison of Non-Dissociative and Dissociative Reduction Pathways. *Environ. Sci. Technol.* **2007**, *41* (9), 3205–3212. https://doi.org/10.1021/es0617892.
(249) Garg, S.; Rose, A. L.; Waite, T. D. Superoxide-Mediated Reduction of Organically Complexed Iron(III): Impact of PH and Competing Cations (Ca2+). *Geochim. Cosmochim. Acta* **2007**, *71* (23), 5620–5634. https://doi.org/10.1016/j.gca.2007.08.002.
(250) Holloway, J. H.; Reilley, C. N. Metal Chelate Stability Constants of Aminopolycarboxylate Ligands. *Anal. Chem.* **1960**, *32* (2), 249–256. https://doi.org/10.1021/ac60158a033.
(251) Rose, A. L.; Waite, T. D. Reduction of Organically Complexed Ferric Iron by Superoxide in a Simulated Natural Water. *Environ. Sci. Technol.* **2005**, *39* (8), 2645–2650. https://doi.org/10.1021/es048765k.
(252) Elbaz-Poulichet, F.; Cauwet, G.; Guan, D. M.; Faguet, D.; Barlow, R.; Mantoura, R. F. C. C18 Sep-Pak Extractable Trace Metals in Waters from the Gulf of Lions. *Mar. Chem.* **1994**, *46* (1–2), 67–75. https://doi.org/10.1016/0304-4203(94)90046-9.
(253) Ksionzek, K. B.; Zhang, × Jing; Ludwichowski, K.-U.; Wilhelms-Dick, D.; Trimborn, S.; Jendrossek, T.; Kattner, G.; Koch, B. P. Stoichiometry, Polarity, and Organometallics in Solid-Phase Extracted Dissolved Organic Matter of the Elbe-Weser Estuary. *PLoS One San Franc.* **2018**, *13* (9), e0203260. http://dx.doi.org/10.1371/journal.pone.0203260.
(254) Goldstone, J. V.; Voelker, B. M. Chemistry of Superoxide Radical in Seawater: CDOM Associated Sink of Superoxide in Coastal Waters. *Environ. Sci. Technol.* **2000**, *34* (6), 1043–1048. https://doi.org/10.1021/es9905445.
(255) Ma, J.; Zhou, H.; Yan, S.; Song, W. Kinetics Studies and Mechanistic Considerations on the Reactions of Superoxide Radical Ions with Dissolved Organic Matter. *Water Res.* **2019**, *149*, 56–64. https://doi.org/10.1016/j.watres.2018.10.081.
(256) Vialaton, D.; Richard, C.; Baglio, D.; Paya-Perez, A.-B. Phototransformation of 4-Chloro-2-Methylphenol in Water: Influence of Humic Substances on the Reaction. *J. Photochem. Photobiol. Chem.* **1998**, *119* (1), 39–45. https://doi.org/10.1016/S1010-6030(98)00401-8.
(257) Powers, L. C.; Babcock-Adams, L. C.; Enright, J. K.; Miller, W. L. Probing the Photochemical Reactivity of Deep Ocean Refractory Carbon (DORC): Lessons from Hydrogen Peroxide and Superoxide Kinetics. *Mar. Chem.* **2015**, *177*, 306–317. https://doi.org/10.1016/j.marchem.2015.06.005.

(258) Shaked, Y.; Harris, R.; Klein-Kedem, N. Hydrogen Peroxide Photocycling in the Gulf of Aqaba, Red Sea. *Environ. Sci. Technol.* **2010**, *44* (9), 3238–3244. https://doi.org/10.1021/es902343y.
(259) Ma, J.; Nie, J.; Zhou, H.; Wang, H.; Lian, L.; Yan, S.; Song, W. Kinetic Consideration of Photochemical Formation and Decay of Superoxide Radical in Dissolved Organic Matter Solutions. *Environ. Sci. Technol.* **2020**, *54* (6), 3199–3208. https://doi.org/10.1021/acs.est.9b06018.
(260) Le Roux, D. M.; Powers, L. C.; Blough, N. V. Photoproduction Rates of One-Electron Reductants by Chromophoric Dissolved Organic Matter via Fluorescence Spectroscopy: Comparison with Superoxide and Hydrogen Peroxide Rates. *Environ. Sci. Technol.* **2021**, *55* (17), 12095–12105. https://doi.org/10.1021/acs.est.1c04043.
(261) Nakano, M.; Kikuyama, M.; Hasegawa, T.; Ito, T.; Sakurai, K.; Hiraishi, K.; Hashimura, E.; Adachi, M. The First Observation of O2− Generation at Real Time in Vivo from Non-Kupffer Sinusoidal Cells in Perfused Rat Liver during Acute Ethanol Intoxication. *FEBS Lett.* **1995**, *372* (2), 140–143. https://doi.org/10.1016/0014-5793(95)00923-W.
(262) Fujimori, K.; Nakajima, H.; Akutsu, K.; Mitani, M.; Sawada, H.; Nakayama, M. Chemiluminescence of Cypridina Luciferin Analogues. Part 1. Effect of PH on Rates of Spontaneous Autoxidation of CLA in Aqueous Buffer Solutions. *J. Chem. Soc. Perkin Trans. 2* **1993**, *0* (12), 2405–2409. https://doi.org/10.1039/P29930002405.
(263) Heller, M. I.; Croot, P. L. Kinetics of Superoxide Reactions with Dissolved Organic Matter in Tropical Atlantic Surface Waters near Cape Verde (TENATSO). *J. Geophys. Res. Oceans* **2010**, *115* (C12), C12038. https://doi.org/10.1029/2009JC006021.
(264) Neta, P.; Grodkowski, J. Rate Constants for Reactions of Phenoxyl Radicals in Solution. *J Phys Chem Ref Data* **2005**, *34* (1), 92.
(265) Jonsson, M.; Lind, J.; Reitberger, T.; Eriksen, T. E.; Merenyi, G. Free Radical Combination Reactions Involving Phenoxyl Radicals. *J. Phys. Chem.* **1993**, *97* (31), 8229–8233. https://doi.org/10.1021/j100133a018.
(266) Jin, F.; Leitich, J.; von Sonntag, C. The Superoxide Radical Reacts with Tyrosine-Derived Phenoxyl Radicals by Addition Rather than by Electron Transfer. *J. Chem. Soc. Perkin Trans. 2* **1993**, No. 9, 1583. https://doi.org/10.1039/p29930001583.
(267) Winterbourn, C. C.; Kettle, A. J. Radical–Radical Reactions of Superoxide: A Potential Route to Toxicity. *Biochem. Biophys. Res. Commun.* **2003**, *305* (3), 729–736. https://doi.org/10.1016/S0006-291X(03)00810-6.
(268) d'Alessandro, N.; Bianchi, G.; Fang, X.; Jin, F.; Schuchmann, H.-P.; von Sonntag, C. Reaction of Superoxide with Phenoxyl-Type Radicals. *J. Chem. Soc. Perkin Trans. 2* **2000**, No. 9, 1862–1867. https://doi.org/10.1039/b003346o.
(269) Romera-Castillo, C.; Jaffe, R. Free Radical Scavenging (Antioxidant Activity) of Natural Dissolved Organic Matter. *Mar. Chem.* **2015**, *177*.
(270) King, D. W.; Berger, E.; Helm, Z.; Irish, E.; Mopper, K. Measurement of Antioxidant Activity toward Superoxide in Natural Waters. *Front. Mar. Sci.* **2016**, *3*. https://doi.org/10.3389/fmars.2016.00217.
(271) Aeschbacher, M.; Graf, C.; Schwarzenbach, R. P.; Sander, M. Antioxidant Properties of Humic Substances. *Environ. Sci. Technol.* **2012**, *46* (9), 4916–4925. https://doi.org/10.1021/es300039h.

(272) Clark, C. D.; De Bruyn, W. J.; Jones, J. G. Photochemical Production of Hydrogen Peroxide in Size-Fractionated Southern California Coastal Waters. *Chemosphere* **2009**, *76* (1), 141–146. https://doi.org/10.1016/j.chemosphere.2009.01.076.
(273) Zhang, D.; Yan, S.; Song, W. Photochemically Induced Formation of Reactive Oxygen Species (ROS) from Effluent Organic Matter. *Environ. Sci. Technol.* **2014**, *48* (21), 12645–12653. https://doi.org/10.1021/es5028663.
(274) Wang, Z.; Lv, J.; Zhang, S.; Christie, P.; Zhang, S. Interfacial Molecular Fractionation on Ferrihydrite Reduces the Photochemical Reactivity of Dissolved Organic Matter. *Environ. Sci. Technol.* **2021**, *55* (3), 1769–1778. https://doi.org/10.1021/acs.est.0c07132.
(275) Zhang, R.; Goldstein, S.; Samuni, A. Kinetics of Superoxide-Induced Exchange among Nitroxide Antioxidants and Their Oxidized and Reduced Forms. *Free Radic. Biol. Med.* **1999**, *26* (9), 1245–1252. https://doi.org/10.1016/S0891-5849(98)00328-1.
(276) Goldstein, S.; Merenyi, G.; Russo, A.; Samuni, A. The Role of Oxoammonium Cation in the SOD-Mimic Activity of Cyclic Nitroxides. *J. Am. Chem. Soc.* **2003**, *125* (3), 789–795. https://doi.org/10.1021/ja028190w.
(277) Heller, M. I.; Croot, P. L. Application of a Superoxide (O2−) Thermal Source (SOTS-1) for the Determination and Calibration of O2− Fluxes in Seawater. *Anal. Chim. Acta* **2010**, *667* (1–2), 1–13. https://doi.org/10.1016/j.aca.2010.03.054.
(278) Svenson, A.; Kaj, L.; Björndal, H. Aqueous Photolysis of the Iron (III) Complexes of NTA, EDTA and DTPA. *Chemosphere* **1989**, *18* (9), 1805–1808. https://doi.org/10.1016/0045-6535(89)90464-5.
(279) Metsärinne, S.; Rantanen, P.; Aksela, R.; Tuhkanen, T. Biological and Photochemical Degradation Rates of Diethylenetriaminepentaacetic Acid (DTPA) in the Presence and Absence of Fe(III). *Chemosphere* **2004**, *55* (3), 379–388. https://doi.org/10.1016/j.chemosphere.2003.10.062.
(280) Albéric, P.; Voillier, E.; Jézéquel, D.; Grosbois, C.; Michard, G. Interactions between Trace Elements and Dissolved Organic Matter in the Stagnant Anoxic Deep Layer of a Meromictic Lake. *Limnol. Oceanogr.* **2000**, *45* (5), 1088–1096. https://doi.org/10.4319/lo.2000.45.5.1088.